Quarkonia Production in Nonrelativistic Quantum Chromodynamics

Thesis by

Adam K. Leibovich

In Partial Fulfillment of the Requirements

for the Degree of

Doctor of Philosophy

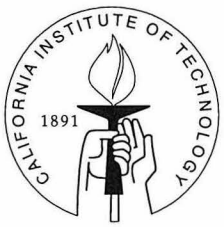

California Institute of Technology

Pasadena, California

1998

(Submitted July 30, 1997)

Acknowledgements

There are a number of people that it is my pleasure to thank. First I would like to thank Mark Wise for many years of advice, abuse and coffee. Next I would like to thank Peter Cho, with whom most of this work was done. I would also like to thank Zoltan Ligeti, who was a constant source of inspiration. There are many friends that have helped me pass the time here at Caltech. I would like to thank Steve Ouellette, Erik and Tanny Daniel and Heather Frase for all the games and movies. Andrea Dvoredsky kept me sane for many years. David Hogg helped me waste a lot of time at the pool table, at the race track, etc. Finally I would like thank my parents for all their love and support.

Abstract

Color-singlet production of quarkonia has failed to correctly predict the cross section of ψ's produced at the Tevatron. Gluon fragmentation has been identified the dominant source of high energy prompt quarkonia at hadron colliders. Fragmentation approximations break down, however, when a quarkonium's transverse momentum becomes comparable to its mass. We review the NRQCD formalism, which is an effective field that improves upon the color-singlet calculations. As an example of color-singlet calculation, we calculate in closed form the complete $\mathcal{O}(\alpha_s^2)$ color-singlet differential cross section for $e^+e^- \to \gamma^* \to \psi_Q + X$ scattering. The cross section reduces at high energies to a heavy quark fragmentation form. We find that the energy scale at which the approximate fragmentation result becomes reliable exceeds the ψ_Q mass by more than an order of magnitude. We also discuss the color-singlet model's predictions for direct J/ψ angular and energy distributions at CLEO. For production at a $p\bar{p}$ collider, we identify a large class of color-octet diagrams that mediate quarkonia production at all energies and reduce to the dominant set of gluon fragmentation graphs in the high $p_\perp$ limit. They contribute to quarkonia differential cross sections at the same order as color-singlet diagrams and bring theoretical predictions for Υ and ψ production at the Tevatron into agreement with experimental measurements. Using recent CDF data, we extract numerical values for bottomonia and charmonia color-octet matrix elements which are consistent with NRQCD scaling rules. We calculated the polarization of ψ' due to $p\bar{p} \to Q\bar{Q}[^{2S+1}L_J^{(8)}]X \to \psi^{(\lambda)}X$ color-octet quarkonia production at order α_s^3 which could be used as a test of NRQCD. We find that at low transverse momenta the ψ' is unpolarized due to the contributions proportional to the $L = S = 0$ and $L = S = 1$ color-octet matrix elements. As $p_\perp$ increases, the ψ' mesons become 100% polarized, as predicted by fragmentation calculations. Polarization due to lowest order color-singlet production is also considered, which qualitatively has a similar shape to the color-octet production.

Contents

List of Figures

List of Tables

Chapter 1 Introduction

It has been more than 20 years since the discovery of the J/ψ [1, 2]. Since that initial discovery, many new and exciting developments have happened in theoretical and experimental particle physics. The study of quarkonia, the bound state of a heavy quark and antiquark, has yielded valuable insight into the nature of the strong interaction. Even though it has been quite a few years, there are many aspects in charm physics that have yet to be fully tested. Similarly, it has been over 20 years since there was conclusive evidence for the Υ [3] and even more of the bottom sector is unexplored. Even though many aspects of heavy flavor physics have yet to be accurately tested or measured, it is very rare that order of magnitude discrepancies are uncovered. With the addition of the silicon vertex detector at the CDF detector at Fermilab's Tevatron, such a discrepancy occurred, the so-called "ψ' anomaly."

The ψ' anomaly was a gross underestimate of the number of prompt charmonia produced in $p\bar{p}$ collisions. The silicon vertex detector allowed the separation of ψ's produced from B decays from those produced at the primary vertex. The calculations that underestimated the production rate were developed shortly after the initial discovery of the J/ψ, and had been fairly, but not completely, successful in describing quarkonia production and decay for over two decades. Thus the anomaly was very surprising.

In the standard picture of quarkonia production, called the Color-Singlet Model (CSM), the heavy quark and antiquark are produced in a hard collision with the same quantum numbers of the final physical state. The model is very predictive since the process of producing the heavy quark–antiquark pair can be calculated in perturbation theory. The bound state is described by the nonrelativistic wavefunction, which can be calculated in a potential model or extracted from data. Since everything can be calculated this model is very powerful.

But what if the heavy quark–antiquark pair is not produced with the same quan-

tum numbers of the final state in the hard collision? In hadron collisions there are lots of soft gluons, which could change the quantum numbers of the initial quark–antiquark pair. Since this is a nonperturbative effect, due to the assumption of soft gluons, this will not be described in the CSM as described above. An effective field theory which can accommodate such soft gluon effects has been proposed. This effective field theory is called Nonrelativistic Quantum Chromodynamics (NRQCD) [4].

Since both the quark and antiquark in quarkonia have a mass much larger than the QCD scale, $M_Q \gg \Lambda_{\rm QCD}$, the relative velocity v between the two is small. Thus the physics is inherently nonrelativistic. This small velocity creates a hierarchy of energy scales, the most important being the mass M_Q, momentum $M_Q v$ and kinetic energy $M_Q v^2$ of the heavy quark and antiquark. As part of the formalism, NRQCD keeps track of this hierarchy, separating effects of different energy scales. Being an effective field theory, NRQCD is made equivalent to full QCD by the addition of nonrenormalizable terms in the Lagrangian. In this thesis we hope to show how NRQCD can be used to calculate quarkonia production and to show that it can help improve predictions of quarkonia production at the Tevatron. The thesis is organized as follows.

In Chapter 2 we begin with the formalism relevant to NRQCD. After showing that Heavy Quark Effective Theory cannot accommodate the relevant physics of quarkonia, we review the NRQCD Lagrangian. Since we have an effective field theory, which is nonrenormalizable, there are an infinite number of terms which could be included in any calculation. Counting rules, which enable this series to be terminated, are discussed. The production and decay of quarkonia is included in the formalism by the addition of four-fermion operators, which is introduced next. As an example of how to calculate in this formalism, an explicit calculation of ψ_Q production at a hadron collider at lowest order is done. Finally, fragmentation, which is relevant to quarkonia production at large energies independent of NRQCD, is reviewed.

In Chapter 3 color-singlet production is discussed. Color-singlet production is often the most important effect in many processes. As an example of this, the direct

J/ψ production at an e^+e^- collider is calculated, and some of the consequences are discussed.

In Chapter 4 we are concerned with color-octet production at a $p\bar{p}$ collider. It turns out that, for kinematic reasons, the color-octet channels dominate over the color-singlet channels at such an experiment. This is a potential solution for the ψ' anomaly. We begin this chapter by calculating the relevant cross sections to order α_s^3. Since these cross sections reduce in the large energy limit to the fragmentation calculation, we can use this as a cross check on our results. In the fragmentation formalism, it is possible to include leading log QCD corrections by using the Altarelli–Parisi equation. It is possible to include these effects into the color-octet calculation by interpolating between the two extremes. This is done for the cross sections in this chapter. Then we compare the results to data. Finally, we discuss tests of NRQCD.

Conclusions are discussed in Chapter 5. There are a few appendices. In Appendix A, we present the squared amplitudes for unpolarized, color-octet quarkonia production at order α_s^2 and α_s^3. In Appendix B, we present functions which are relevant to the color-singlet e^+e^- cross section. Appendix C discusses the angular distributions in electron-positron collisions. Finally in Appendix D, we present functions which are relevant to the polarized, color-octet production at order α_s^3.

Chapter 2 Formalism

Heavy Quark Effective Theory (HQET) is very successful in describing physics of hadrons containing a single heavy quark [5, 6]. The physics of quarkonia, however, cannot be described by HQET. A system containing a heavy quark and antiquark form a Coulomb bound state as the mass of the heavy quark, M_Q goes to infinity $M_Q \to \infty$. If there is no kinetic energy to stabilize the energy, as is the case in HQET, the quarks fall deeper into the potential well as the mass of the quarks tend toward infinity and divergences arise. Another way of seeing this is by looking at the behavior of the Feynman diagram [7] pictured in Fig. 2.1. Evaluating the box

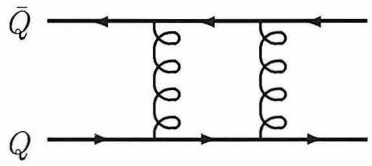

Figure 2.1: $Q\bar{Q}$ scattering at one loop. The resulting cross section is proportional to $M_Q/|\vec{q}| = 1/|\vec{v}|$, where $\vec{q}$ and $\vec{v}$ are the three-momentum and velocity of the heavy quarks.

diagram in full QCD yields terms of order $M_Q/|\vec{q}| = 1/|\vec{v}|$, where $\vec{q}$ and $\vec{v}$ are the three-momentum and velocity of the heavy quarks. The HQET Lagrangian is

$$\mathcal{L}_{\text{HQET}} = Q^\dagger (iD^0) Q, \tag{2.1}$$

where Q annihilates a heavy quark. In this Lagrangian, the kinetic energy of the heavy quark is higher order in the $1/M_Q$ expansion. In HQET the box diagram is of the form

$$\int d^4q \frac{1}{q^0 + i\epsilon} \frac{1}{-q^0 + i\epsilon}. \tag{2.2}$$

The q^0 integral has the pinch singularity shown in Fig. 2.2 and diverges as $\epsilon \to 0$. If

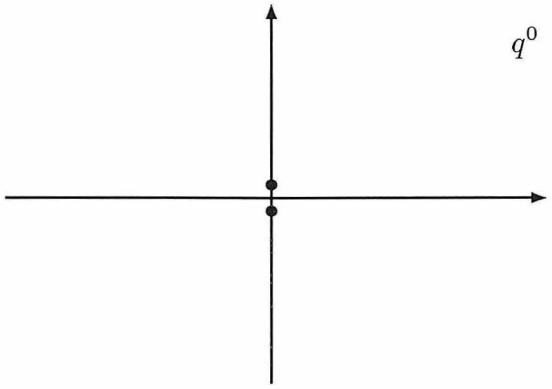

Figure 2.2: Poles in the q^0 plane for loop diagram in HQET. The poles result in a pinch singularity as $\epsilon \to 0$.

we add the kinetic energy to the Lagrangian in Eq. (2.1)

$$\mathcal{L} = Q^\dagger (iD^0) Q + Q^\dagger \frac{\vec{D}^2}{2M_Q} Q, \tag{2.3}$$

the form of the loop integral becomes

$$\int d^4q \frac{1}{q^0 - |\vec{q}|^2/2M_Q + i\epsilon} \frac{1}{-q^0 - |\vec{q}|^2/2M_Q + i\epsilon}. \tag{2.4}$$

Now the poles are separated (Fig. 2.3) and the integral can be calculated giving the correct form of $M_Q/\vec{q}$. Thus, the physics of quarkonia must treat the two operators in Eq. (2.3) as the same order, even though one is suppressed by $1/M_Q$. A new effective

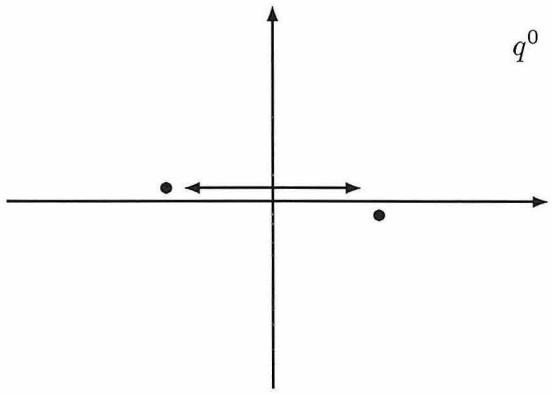

Figure 2.3: Poles in the q^0 plane for loop diagram in NRQCD. The addition of the kinetic energy has separated the poles, resulting in a finite integral as $\epsilon \to 0$.

field theory must be introduced in order to accommodate this fact.

2.1 Nonrelativistic Quantum Chromodynamics

Quarkonia bound states are qualitatively different from most other hadrons since they are inherently nonrelativistic. The physics of quarkonia consequently involves several energy scales which are separated by the small velocity v of the heavy constituents inside $Q\bar{Q}$ bound states. The most important scales are set by the mass M_Q, momentum $M_Q v$, and kinetic energy $M_Q v^2$ of the heavy quark and antiquark. In order to keep track of this scale hierarchy, an effective field theory called Nonrelativistic Quantum Chromodynamics (NRQCD) has been established [4]. This effective theory for $Q\bar{Q}$ bound states shares several similarities with the HQET which describes the low energy QCD structure of heavy-light $Q\bar{q}$ mesons. For example, NRQCD is based upon a double power series expansion in the strong interaction fine structure constant $\alpha_s = g_s^2/4\pi$ and the velocity parameter $v \sim 1/\log M_Q$ which is similar to the HQET's double expansion in α_s and $1/M_Q$. Both theories also incorporate approximate spin symmetry relations which constrain various multiplet structures and transition rates. But most importantly, NRQCD systematizes one's understanding of charmonia and bottomonia just as the HQET methodically organizes the physics of D and B mesons.

Before the development of NRQCD, quarkonia were generally treated as nonrelativistic bound states of a heavy quark and antiquark in a static gluon field that sets up an instantaneous confining potential [8]. Although this picture has enjoyed a remarkable degree of phenomenological success, it fails to take into account gluons inside a quarkonium with wavelengths much greater than the bound state's characteristic size. The presence of such low energy gluons implies that the heavy quark and antiquark cannot always be regarded as residing in a color-singlet configuration.

This shortcoming of the potential model approach is rectified in NRQCD. Dynamical gluons enter into Fock state decompositions of physical quarkonium states. For example, wavefunctions for S-wave orthoquarkonia schematically appear in Coulomb gauge as

$$|\psi_Q\rangle = \mathcal{O}(1)|Q\bar{Q}[^3S_1^{(1)}]\rangle + \mathcal{O}(v)|Q\bar{Q}[^3P_J^{(8)}]g\rangle \tag{2.5}$$
$$+\mathcal{O}(v^2)|Q\bar{Q}[^1S_0^{(8)}]g\rangle + \mathcal{O}(v^2)|Q\bar{Q}[^3S_1^{(1,8)}]g\rangle + \mathcal{O}(v^2)|Q\bar{Q}[^3D_J^{(1,8)}]gg\rangle + \cdots .$$

The spin, orbital and total angular momentum quantum numbers of the $Q\bar{Q}$ pairs in each Fock component are indicated within the square brackets in spectroscopic notation, while the pairs' color assignments are specified by singlet or octet superscripts. The order in the velocity expansion at which each of these Fock states participates in ψ_Q annihilation or creation processes is governed by simple NRQCD counting rules [9]. For instance, suppose a heavy quark and antiquark are produced almost on-shell with nearly parallel 3-momenta in some high energy reaction. The low energy hadronization of this pair into a physical ψ_Q bound state takes place at $\mathcal{O}(v^3)$ if it has the same angular momentum and color quantum numbers as those displayed in the first Fock component of Eq. (2.5). The long distance evolution of all other $Q\bar{Q}$ pairs generated at short distance scales into ψ_Q mesons occurs at higher orders in the velocity expansion.

If the relative importance of various quarkonia production channels depended solely upon the order in v at which pairs hadronize into physical bound states, those modes which proceed through the leading Fock components in quarkonia wavefunction decompositions would generally be dominant. This assumption coincides with the basic tenet of the so-called color-singlet model (CSM) [10, 11, 12, 13, 14, 15, 16]. Quarkonium production is presumed in this model to be mediated by parton reactions that generate colorless heavy quark-antiquark pairs with the same quantum numbers as the mesons into which they nonperturbatively evolve. Transverse momentum distributions calculated within this picture badly underestimate experimental observations for $p_\perp \gtrsim 2M_Q$. The breakdown of the color-singlet model stems from its neglect of all high energy processes that create $Q\bar{Q}$ pairs with quantum numbers different from those of the final state meson. In particular, it overlooks short distance contributions to quarkonia cross sections from intermediate color-octet states which can be orders of magnitude larger than those from color-singlet pairs. Even if the long distance hadronization of the former is suppressed by several powers of v compared

to the latter, the color-octet components of quarkonia distributions can dominate overall.

As a simple example of the importance of higher Fock state components, consider the P-wave Fock state expansion

$$|\chi_{QJ}\rangle = \mathcal{O}(1)|Q\bar{Q}[^3P_J^{(1)}]\rangle + \mathcal{O}(v)|Q\bar{Q}[^3S_1^{(8)}]g\rangle + \cdots . \tag{2.6}$$

Contributions to χ_{QJ} formation which involve the first color-singlet Fock component are proportional to the squared derivative of the P-wave bound state's wavefunction at the origin. This quantity counts as $\mathcal{O}(v^5)$ in the NRQCD velocity expansion. On the other hand, short distance creation of the S-wave color-octet $Q\bar{Q}$ pair in the second Fock state of Eq. (2.6) takes place at $\mathcal{O}(v^3)$. The subsequent long distance evolution of the $Q\bar{Q}[^3S_1^{(8)}]$ pair into a colorless χ_{QJ} hadron via the emission or absorption of a soft gluon costs an additional power of v in the amplitude and v^2 in the rate. So χ_{QJ} production proceeds at $\mathcal{O}(v^5)$ in both the color-singlet and color-octet mechanisms [17].

It is useful to draw a picture which clarifies the difference between these two quarkonium production mechanisms. In Fig. 2.4, we illustrate a typical color-singlet Feynman graph that creates a χ_{QJ}. The $\mathcal{O}(\alpha_S^3)$ hard scattering forms a colorless $Q\bar{Q}[^3P_J^{(1)}]$ pair at a short distance scale. The heavy quark and antiquark fly out from the initial collision point in nearly parallel directions and almost on mass shell. After exchanging many soft gluons, the color-singlet $Q\bar{Q}$ pair eventually hadronizes at a long distance into a χ_{QJ} bound state. In Fig. 2.5, the $\mathcal{O}(\alpha_S^3)$ high energy collision creates a $Q\bar{Q}$ pair in a color-octet configuration. Far away from the collision point, the $Q\bar{Q}[^3S_1^{(8)}]$ pair emits a long wavelength gluon which bleeds off its color but carries away virtually no energy or momentum. The heavy pair thus transforms into a colorless χ_{QJ} quarkonium state.

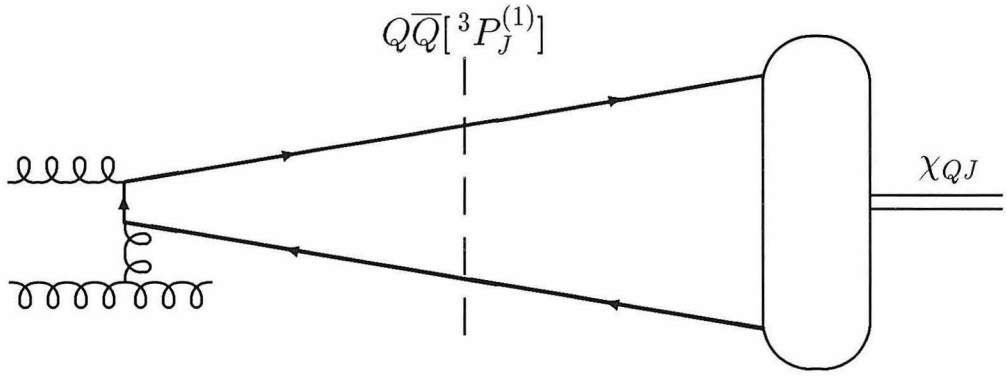

Figure 2.4: Typical Feynman diagram which contributes to χ_{QJ} production at $\mathcal{O}(\alpha_s^3)$ through the color-singlet mechanism. The short-distance scattering collision creates a $Q\bar{Q}$ pair in a $^3P_J^{(1)}$ configuration. The $Q\bar{Q}$ pair hadronizes at long distances into a χ_{QJ} bound state.

2.1.1 Lagrangian

To obtain the NRQCD Lagrangian we begin with full QCD and introduce an ultraviolet cutoff $\Lambda \sim M_Q$. Effects which are removed by introduction of this cutoff are re-introduced as local interactions in the Lagrangian. Next a Foldy-Wouthuysen transformation [18, 19] is used to decouple the heavy-quark and antiquark degrees of freedom. This allows the Dirac spinor fields to be replace by two Pauli spinors for the heavy quark and antiquark. The resulting Lagrangian is the NRQCD Lagrangian [20, 4]

$$\mathcal{L}_{\text{NRQCD}} = \mathcal{L}_{\text{light}} + \mathcal{L}_{\text{heavy}} + \delta\mathcal{L}. \tag{2.7}$$

The light quarks and gluons are described by

$$\mathcal{L}_{\text{light}} = -\frac{1}{2}\text{Tr}F_{\mu\nu}F^{\mu\nu} + \sum \bar{q} i \not{D} q, \tag{2.8}$$

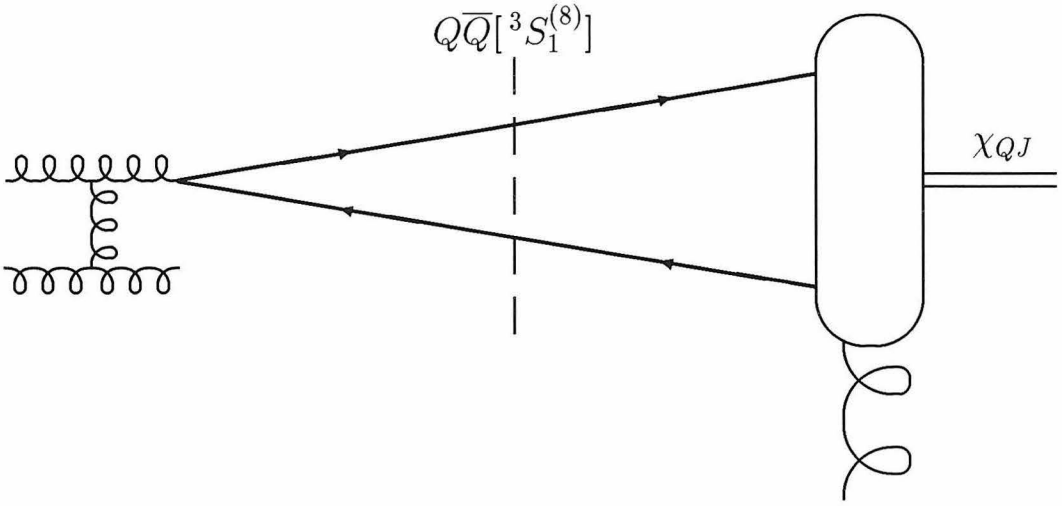

Figure 2.5: Typical Feynman diagram which contributes to χ_{QJ} production at $\mathcal{O}(\alpha_s^3)$ through the color-octet mechanism. The short-distance scattering collision creates a $Q\bar{Q}$ pair in a $^3S_1^{(8)}$ configuration. The long wavelength gluon represents the hadronization process by which color is removed from the color-octet state. Essentially no energy nor momentum is transferred to the $Q\bar{Q}$ pair during the hadronization into the final state χ_{QJ}.

where $F_{\mu\nu}$ is the gluon field strength tensor, and D is the usual covariant derivative. The sum in Eq. (2.8) is over the n_f light quarks. The heavy quarks are described by

$$\mathcal{L}_{\text{heavy}} = \psi^\dagger\Big(iD^0 + \frac{\vec{D}^2}{2M_Q}\Big)\psi + \chi^\dagger\Big(iD^0 - \frac{\vec{D}^2}{2M_Q}\Big)\chi \tag{2.9}$$

where ψ is the Pauli spinor that annihilates a heavy quark and χ is the Pauli spinor that creates a heavy antiquark. The relativistic corrections are included in the term $\delta\mathcal{L}$:

$$\begin{aligned}\delta\mathcal{L} = &\frac{c_1}{8M^3}\left[\psi^\dagger(\vec{D}^2)^2\psi - \chi^\dagger(\vec{D}^2)^2\chi\right] \\ &+\frac{c_2}{8M^2}\left[\psi^\dagger(\vec{D}\cdot g\vec{E} - g\vec{E}\cdot\vec{D})\psi + \chi^\dagger(\vec{D}\cdot g\vec{E} - g\vec{E}\cdot\vec{D})\chi\right] \\ &+\frac{c_3}{8M^2}\left[\psi^\dagger(i\vec{D}\times g\vec{E} - g\vec{E}\times i\vec{D})\cdot\vec{\sigma}\psi + \chi^\dagger(i\vec{D}\times g\vec{E} - g\vec{E}\times i\vec{D})\cdot\vec{\sigma}\chi\right] \\ &+\frac{c_4}{2M}\left[\psi^\dagger(g\vec{B}\cdot\vec{\sigma})\psi - \chi^\dagger(g\vec{B}\cdot\vec{\sigma})\chi\right] + \cdots .\end{aligned} \tag{2.10}$$

Here, $E^i = F^{0i}$ and $B^i = \frac{1}{2}\epsilon^{ijk}F^{jk}$ are the chromo-electric and magnetic fields. The operators are renormalized and the coefficients c_i depend upon Λ such that the dependence on the cutoff is canceled from the Lagrangian. The coefficients are determined

Operator	Scaling	Description
α_s	v	quark-gluon coupling constant
ψ	$(Mv)^{3/2}$	heavy quark field
D^0	Mv^2	gauge-covariant time derivative
$\vec{D}$	Mv	gauge-covariant spatial derivative
$g\vec{E}$	M^2v^3	chromoelectric field
$g\vec{B}$	M^2v^4	chromomagnetic field
$g\phi$	Mv^2	scalar potential
$g\vec{A}$	Mv^3	vector potential

Table 2.1: Velocity scaling rules for various NRQCD operators in the Coulomb gauge.

by matching scattering amplitudes in NRQCD to the corresponding amplitudes in full QCD, and are $c_i = 1 + \mathcal{O}(\alpha_s)$ [20, 9].

Since we have integrated out quarks and gluons with energy of the order of M_Q, we cannot annihilate or create heavy quarks in our Lagrangian. Thus we have no mixed terms with both ψ and $\chi^\dagger$. To include such effects, four-fermion operators are added as described in section 2.1.3.

2.1.2 Velocity counting rules

Effective field theories, while being nonrenormalizable, are a powerful tool. This power comes from the fact that it is possible to terminate the number of contributions to any given process by using some simple counting rules. For example, in HQET the expansion is in one over the mass of the heavy quark, $1/M_Q$. In chiral perturbation theory, it is in powers of the momentum. Without counting rules, there would be no systematic way to terminate the expansion.

The power counting in NRQCD is in terms of the small relative three-velocity v between the heavy quarks. This intuitively makes sense, since it is a nonrelativistic expansion. Working in the Coulomb gauge at tree level, the naive counting rules are quite simple and are summarized in Table 2.1 [21].

At one loop, however, the counting rules are not as straight forward as for other effective field theories. The problem is that loops can be proportional to $1/v$, so that adding extra loops may make certain graphs more important than lower order

processes. There has been much work on trying to make the counting rules manifest for NRQCD [22, 7, 23, 24], but so far no solution seems completely satisfying. All the work presented here was done at tree level, so no problem in power counting arises. For the rest of this work, we will assume that some power counting scheme is possible at all orders, and that NRQCD is a true effective field theory.

2.1.3 Quarkonia annihilation

Annihilation of a heavy $Q\bar{Q}$ state occurs at energy scales of the order of M_Q, or alternatively distance scales of the order $1/M_Q$. This process creates light quarks and gluons with large energy which cannot be treated accurately in NRQCD. While the amplitude cannot be calculated, the annihilation rate, which is the square of the amplitude, can be accounted for in NRQCD. Since the annihilation rate of a $Q\bar{Q}$ pair is localized, the annihilation contribution to the process $Q\bar{Q} \to Q\bar{Q}$ can be reproduced by the addition of four-fermion operators to the NRQCD Lagrangian. The optical theory can then be used to related the imaginary part of the scattering amplitude to the annihilation of the $Q\bar{Q}$ pair.

We add to the NRQCD Lagrangian [4]

$$\delta\mathcal{L}_{4-\text{fermion}} = \sum_n \frac{f_n(\Lambda)}{M_Q^{d_n-4}} \mathcal{O}_n(\Lambda), \tag{2.11}$$

where $\mathcal{O}_n$ are four-fermion operators and d_n is the naive scaling dimension of the operator $\mathcal{O}_n$. The scaling dimension can be calculated by counting powers of M_Q using Table 2.1. The dimensionless coefficients f_n depend on the ultraviolet cutoff since the operators $\mathcal{O}_n$ need to be regularized.

The four-fermion operators start at dimension 6 and are

$$\begin{aligned}(\delta\mathcal{L}_{4-\text{fermion}})_{d=6} = &\frac{f_1(^1S_0)}{M_Q^2}\mathcal{O}_1(^1S_0) + \frac{f_1(^3S_1)}{M_Q^2}\mathcal{O}_1(^3S_1) + \frac{f_8(^1S_0)}{M_Q^2}\mathcal{O}_8(^1S_0) \\ &+ \frac{f_8(^3S_1)}{M_Q^2}\mathcal{O}_8(^3S_1),\end{aligned} \tag{2.12}$$

where

$$\mathcal{O}_1(^1S_0) = \psi^\dagger \chi \chi^\dagger \psi, \tag{2.13}$$

$$\mathcal{O}_1(^3S_1) = \psi^\dagger \vec{\sigma} \chi \cdot \chi^\dagger \vec{\sigma} \psi, \tag{2.14}$$

$$\mathcal{O}_8(^1S_0) = \psi^\dagger T^a \chi \chi^\dagger T^a \psi, \tag{2.15}$$

$$\mathcal{O}_8(^3S_1) = \psi^\dagger \vec{\sigma} T^a \chi \cdot \chi^\dagger \vec{\sigma} T^a \psi. \tag{2.16}$$

The spectroscopic notation refers to the quantum numbers of the $Q\bar{Q}$ pair. Dimension 8 operators include insertions of covariant derivatives such as

$$\mathcal{O}_1(^1P_1) = \psi^\dagger (-\frac{i}{2} \overleftrightarrow{D^j}) \chi \chi^\dagger (-\frac{i}{2} \overleftrightarrow{D^j}) \psi, \tag{2.17}$$

$$\mathcal{O}_1(^3P_0) = \frac{1}{3} \psi^\dagger (-\frac{i}{2} \overleftrightarrow{D^j}\, \sigma^j) \chi \chi^\dagger (-\frac{i}{2} \overleftrightarrow{D^k}\, \sigma^k) \psi, \tag{2.18}$$

$$\mathcal{O}_1(^3P_1) = \frac{1}{2} \epsilon^{ijk} \epsilon^{ilm} \psi^\dagger (-\frac{i}{2} \overleftrightarrow{D^j}\, \sigma^k) \chi \chi^\dagger (-\frac{i}{2} \overleftrightarrow{D^l}\, \sigma^m) \psi, \tag{2.19}$$

$$\mathcal{O}_1(^3P_1) = \psi^\dagger (-\frac{i}{2} \overleftrightarrow{D^{(j}}\, \sigma^{k)}) \chi \chi^\dagger (-\frac{i}{2} \overleftrightarrow{D^{(j}}\, \sigma^{k)}) \psi, \tag{2.20}$$

and similar terms with insertions of a color matrix T^a. Here $\chi^\dagger \overleftrightarrow{D} \psi \equiv \chi^\dagger (D\psi) - (D\chi^\dagger)\psi$, and $T^{(ij)} = (T^{ij} + T^{ji})/2 - T^{kk}\delta^{ij}/3$.

Using the optical theorem, it is straightforward to show that the annihilation rate of a quarkonium state H into light hadrons is

$$\begin{aligned} \Gamma(H \to \text{light hadrons}) &= 2\,\mathrm{Im}\,\langle H|\delta\mathcal{L}_{4-\text{fermion}}|H\rangle \\ &= \sum_n \frac{2\,\mathrm{Im} f_n(\Lambda)}{M_Q^{d_n-4}} \langle H|\mathcal{O}_n(\Lambda)|H\rangle. \end{aligned} \tag{2.21}$$

Calculations of the annihilation rate depend upon the NRQCD matrix elements $\langle H|\mathcal{O}_n(\Lambda)|H\rangle$. By using heavy quark spin symmetry it is possible to reduce the number of independent matrix elements, and the color-singlet matrix elements can be related to the quarkonia wave function (or derivatives of the wave function) at the origin. These matrix elements can either be calculated on the lattice, or, for those related to wave functions, from a potential model. Alternatively, the value of the matrix elements can be extracted from experiment.

2.1.4 Quarkonia production

The production of a $Q\bar{Q}$ state takes place at distance scales on the order of $1/M_Q$ or less, since the momentum transfer is of the order M_Q^2. The formation of the hadron H

involves exchange of soft gluons over a distance the size of the final state, $1/(M_Q v)$. Thus, in NRQCD the production of the $Q\bar{Q}$ state occurs at a spacetime point. This pair propagates to the asymptotic future evolving into the physical quarkonium and perhaps other final particles. The production rate is proportional to the square of this process, and thus can be described in terms of vacuum matrix elements of four-fermion operators. Unlike the annihilation matrix elements, the production matrix elements have a projection operator inserted to ensure the inclusion of the final state quarkonium in the asymptotic future. The general form of the production operator is [4]

$$\begin{aligned}\mathcal{O}_n^H &= \chi^\dagger K_n \psi \left(\sum_X |H+X\rangle\langle H+X| \right) \psi^\dagger K_n' \chi \\ &\equiv \chi^\dagger K_n \psi \left(a_H^\dagger a_H \right) \psi^\dagger K_n' \chi, \end{aligned} \tag{2.22}$$

where the sum is over all other final state particles and the factors K_n and K_n' are products of color matrices, spin matrices, polynomials in the covariant derivative operator and other fields. Note that the insertion of the final state projection means that these objects are not truly local.

The dimension 6 production operators are

$$\mathcal{O}_1^H(^1S_0) = \chi^\dagger \psi \left(a_H^\dagger a_H \right) \psi^\dagger \chi, \tag{2.23}$$

$$\mathcal{O}_1^H(^3S_1) = \chi^\dagger \sigma^i \psi \left(a_H^\dagger a_H \right) \psi^\dagger \sigma^i \chi, \tag{2.24}$$

$$\mathcal{O}_8^H(^1S_0) = \chi^\dagger T^a \psi \left(a_H^\dagger a_H \right) \psi^\dagger T^a \chi, \tag{2.25}$$

$$\mathcal{O}_8^H(^3S_1) = \chi^\dagger \sigma^i T^a \psi \left(a_H^\dagger a_H \right) \psi^\dagger \sigma^i T^a \chi, \tag{2.26}$$

while some of the dimension 8 operators are

$$\mathcal{O}_1^H(^1P_1) = \chi^\dagger (-\frac{i}{2} \overleftrightarrow{D^j}) \psi \left(a_H^\dagger a_H \right) \psi^\dagger (-\frac{i}{2} \overleftrightarrow{D^j}) \chi, \tag{2.27}$$

$$\mathcal{O}_1^H(^3P_0) = \frac{1}{3} \chi^\dagger (-\frac{i}{2} \overleftrightarrow{D^j}\, \sigma^j) \psi \left(a_H^\dagger a_H \right) \psi^\dagger (-\frac{i}{2} \overleftrightarrow{D^k}\, \sigma^k) \chi, \tag{2.28}$$

$$\mathcal{O}_1^H(^3P_1) = \frac{1}{2} \epsilon^{ijk} \epsilon^{ilm} \chi^\dagger (-\frac{i}{2} \overleftrightarrow{D^j}\, \sigma^k) \psi \left(a_H^\dagger a_H \right) \psi^\dagger (-\frac{i}{2} \overleftrightarrow{D^l}\, \sigma^m) \chi, \tag{2.29}$$

$$\mathcal{O}_1^H(^3P_1) = \chi^\dagger (-\frac{i}{2} \overleftrightarrow{D^{(j}}\, \sigma^{k)}) \psi \left(a_H^\dagger a_H \right) \psi^\dagger (-\frac{i}{2} \overleftrightarrow{D^{(j}}\, \sigma^{k)}) \chi. \tag{2.30}$$

Color-octet dimension 8 operators are similar, with the insertion of T^a matrices. As for quarkonia annihilation, the color-singlet matrix elements can be related to the nonrelativistic wavefunction. For example [4],

$$\langle 0|\mathcal{O}_1^{\psi_Q}(^3S_1)|0\rangle = \frac{N_c}{2\pi}|R(0)|^2[1+\mathcal{O}(v^4)], \tag{2.31}$$

$$\langle 0|\mathcal{O}_1^{\chi_{QJ}}(^3P_J)|0\rangle = \frac{3N_c}{2\pi}(2J+1)|R'(0)|^2[1+\mathcal{O}(v^2)]. \tag{2.32}$$

The general form of the production cross section in NRQCD is

$$\sigma(H) = \sum_n \frac{F_n(\Lambda)}{M^{d_n-4}}\langle 0|\mathcal{O}_n^H(\Lambda)|0\rangle. \tag{2.33}$$

The coefficients $F_n(\Lambda)$ can be calculated in a perturbative series in α_s. They represent the short distance physics for the production of the $Q\bar{Q}$ pair, but include no knowledge of the hadronization to the final state H, and are thus independent of the final state particle. In this way the cross section is factorized into a short distance part and a long distance part.

The factorization may be destroyed by soft gluon effects. The $Q\bar{Q}$ pair can in general be a colored object, and thus will couple to any quarks or gluons that are around, including perhaps spectator quarks in a hadron collision. For a hadron collider one can prove that the factorized form hold through next-to-leading order in an expansion in inverse powers of the large momentum transfer Q^2 [25, 26]. Beyond this order, the factorization can be shown to fail [27]. While this is a potential problem, we will assume violations of the factorization are small.

2.2 Calculating Cross Sections

2.2.1 ψ_Q production in $2 \to 1$ collisions

Color-octet quarkonia production starts at $\mathcal{O}(\alpha_s^2)$ with the scattering processes $q + \bar{q} \to Q + \bar{Q}$ and $g + g \to Q + \bar{Q}$. The Feynman diagrams which mediate these reactions are illustrated in Figs. 2.6 and 2.7. In the first quark scattering channel, the heavy quark-antiquark pair appearing in the final state must share the same

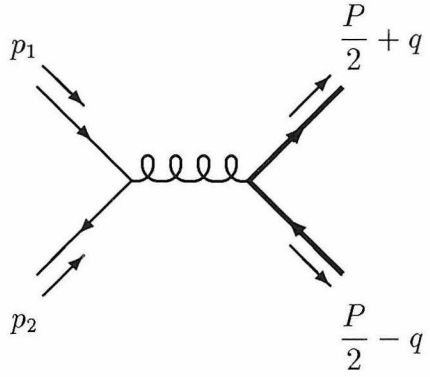

Figure 2.6: Lowest order Feynman graph which mediates $q+\bar{q}\to Q+\bar{Q}$ scattering.

quantum numbers as its intermediate virtual gluon progenitor. Angular momentum, parity and charge conjugation conservation restrict the spin, orbital and total angular momentum quantum numbers of the $Q\bar{Q}$ pair to $L=0\,\text{or}\,2$, $S=1$ and $J=1$. In the second gluon scattering process, the allowed values for L, S and J are not so tightly prescribed.

To begin, we write down the on-shell scattering amplitude

$$\begin{aligned}\mathcal{A}\left(g_a(p_1)g_b(p_2)\to Q^i(\frac{P}{2}+q;s_1)\bar{Q}_j(\frac{P}{2}-q;s_2)\right) &= -2g_s^2\varepsilon^\mu(p_1)\varepsilon^\nu(p_2) \\ \times\bar{u}(\frac{P}{2}+q;s_1)\Big\{(T_aT_b)^i_j&\frac{\gamma_\mu[\not{p}_2-\not{p}_1+2\not{q}+2M_Q]\gamma_\nu}{(p_2-p_1+2q)^2-4M_Q^2} \\ +(T_bT_a)^i_j&\frac{\gamma_\nu[\not{p}_1-\not{p}_2+2\not{q}+2M_Q]\gamma_\mu}{(p_2-p_1-2q)^2-4M_Q^2} \\ -\frac{i}{8M_Q^2}&f_{abc}(T_c)^i_j[g_{\mu\nu}(\not{p}_2-\not{p}_1)+2(p_{1\nu}\gamma_\mu-p_{2\mu}\gamma_\nu)]\Big\}v(\frac{P}{2}-q;s_2)\end{aligned} \tag{2.34}$$

that corresponds to the sum of the three graphs displayed in Fig. 2.7. The reduced amplitude which describes the creation of a $Q\bar{Q}$ pair in a particular angular momentum and color configuration is obtained from this expression by applying a series of projection operations [28]:[1]

[1]There are many ways to project out the correct state from the above amplitude. The method described here works for low orders in the velocity expansion, and is easily extendable to include more particles in the final state. For another projection method, see [29, 30].

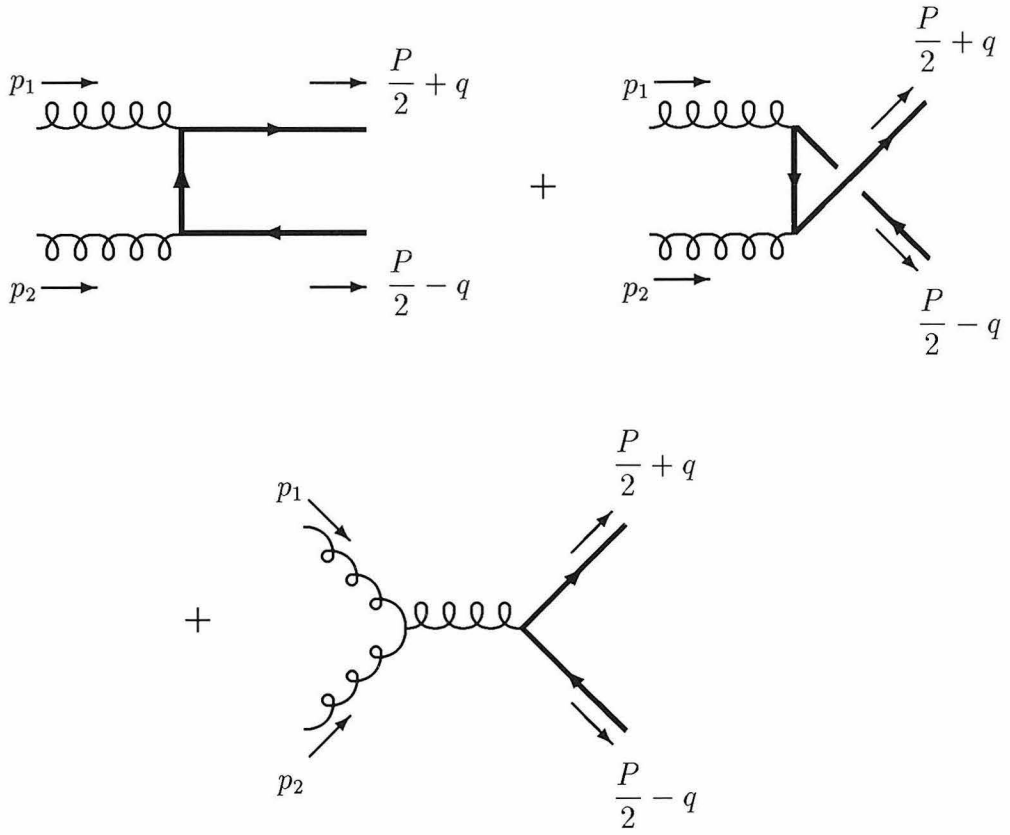

Figure 2.7: Lowest order Feynman graphs which mediate $g + g \to Q + \bar{Q}$ scattering.

$$\mathcal{A}\left(g_a(p_1)g_b(p_2) \to Q\bar{Q}[^{2S+1}L_J^{(1,8c)}](P)\right) = \tag{2.35}$$
$$\sum_{L_Z,S_Z}\sum_{s_1,s_2}\sum_{i,j}\int \frac{d^3q}{(2\pi)^3 2q^0}\delta(q^0 - \frac{\vec{q}^{\,2}}{M})Y^*_{LL_Z}(\hat{q})\langle\frac{1}{2}s_1;\frac{1}{2}s_2|SS_Z\rangle\langle LL_Z;SS_Z|JJ_Z\rangle$$
$$\times\langle 3i;\bar{3}j|1,8c\rangle\mathcal{A}\left(g_a(p_1)g_b(p_2) \to Q^i(\frac{P}{2}+q;s_1)\bar{Q}_j(\frac{P}{2}-q;s_2)\right).$$

Several points about this projection formula should be noted. Firstly, a $Q\bar{Q}$ pair has negligible overlap with a nonrelativistic quarkonium bound state unless the relative momentum q between the heavy quark and antiquark is small compared to their combined momentum P. We have therefore incorporated a delta function into Eq. (2.35) which restricts the triple integral over q to the two-dimensional surface defined by $|\vec{q}| = \sqrt{Mq^0}$ where $q^0 \simeq Mv^2 \ll M \equiv 2M_Q$. The squared invariant mass of the $Q\bar{Q}$ pair thus equals $P^2 = M^2$ up to small relativistic corrections, where M is the mass of the quarkonium. Inclusion of the delta function also properly converts the mass dimension of the $2 \to 2$ scattering amplitude into that for a $2 \to 1$ reaction. Secondly,

the angular integration over the spherical harmonic projects out the pair's specified partial wave. The sums over the Clebsch-Gordan coefficients similarly project out the spin and total angular momentum of the $Q\bar{Q}$ object. It is possible to combine the sum over the spin Clebsh-Gordan coefficient and the heavy quark spinors into a spin projection operator as[2]

$$P_{SS_z}(P;q) = \sum_{s_1,s_2} v(\frac{P}{2} - q; s_2)\bar{u}(\frac{P}{2} + q; s_1)\langle \frac{1}{2}s_1; \frac{1}{2}s_2 | SS_z\rangle \tag{2.36}$$

This 4×4 matrix reduces to the covariant expressions

$$\begin{aligned} P_{00}(P;q) &= \frac{-1}{2\sqrt{2}M_Q}(\frac{\not{P}}{2} - \not{q} - M_Q)\gamma^5(\frac{\not{P}}{2} + \not{q} + M_Q) \\ P_{1S_z}(P;q) &= \frac{-1}{2\sqrt{2}M_Q}(\frac{\not{P}}{2} - \not{q} - M_Q)\not{\epsilon}^*(P;S_z)(\frac{\not{P}}{2} + \not{q} + M_Q) \end{aligned} \tag{2.37}$$

up to $\mathcal{O}(q^2)$ corrections. Finally, the sum over the $SU(3)$ coefficients

$$\begin{aligned} \langle 3i; \bar{3}j|1\rangle &= \delta_i^j/\sqrt{N_c} \\ \langle 3i; \bar{3}j|8c\rangle &= \sqrt{2}(T_c)_i^j \end{aligned} \tag{2.38}$$

combines together the color quantum numbers of the quark and antiquark into either a singlet or octet configuration.

Inserting the gluon scattering amplitude Eq. (2.34) into the projection formula in Eq. (2.35), we can readily calculate the reduced amplitude for two gluons to fuse into an arbitrary color-octet combination. We list below the formation amplitudes for $Q\bar{Q}[^3S_1^{(8)}]$, $Q\bar{Q}[^1S_0^{(8)}]$ and $Q\bar{Q}[^3P_J^{(8)}]$ pairs which all hadronize into ψ_Q bound states at $\mathcal{O}(v^7)$ in the velocity expansion [31, 28]:

$$\begin{aligned} \mathcal{A}(g_a(p_1)g_b(p_2) \to Q\bar{Q}[^3S_1^{(8)}]_c &= \frac{ig_s^2 f_{abc}}{4(2\pi)^3}\sqrt{\frac{4\pi M}{q^0}}\varepsilon^\mu(p_1)\varepsilon^\nu(p_2)\varepsilon^\sigma(S_z)^* \\ &\times \frac{p_1^2 + p_2^2}{p_1^2 + p_2^2 - M^2}[(p_2 - p_1)_\sigma g_{\mu\nu} + 2(p_{1\nu}g_{\mu\sigma} - p_{2\mu}g_{\nu\sigma})] \end{aligned} \tag{2.39a}$$

[2]Spin projection matrices were originally introduced in Refs. [14, 15]. The $\bar{u}$ and v spinors in our definition of P_{SS_z} correspond to an outgoing $Q\bar{Q}$ pair. They differ from the $\bar{v}$ and u spinors appearing in these earlier articles' spin projection operators. Our $(+,-,-,-)$ metric signature convention is also opposite to that of Ref. [15].

$$\mathcal{A}(g_a(p_1)g_b(p_2) \to Q\bar{Q}[^1S_0^{(8)}]_c) = -\frac{ig_s^2 d_{abc}}{2(2\pi)^3}\sqrt{\frac{4\pi M}{q^0}}\frac{M\epsilon_{\sigma\tau\mu\nu}p_1^\sigma p_2^\tau \varepsilon^\mu(p_1)\varepsilon^\nu(p_2)}{p_1^2+p_2^2-M^2} \tag{2.39b}$$

$$\begin{aligned}\mathcal{A}(g_a(p_1)g_b(p_2) \to Q\bar{Q}[^3P_J^{(8)}]_c) &= \frac{g_s^2 d_{abc}}{2(2\pi)^3}\sqrt{\frac{4\pi}{3}}\sum_{L_Z,S_Z}\langle 1L_Z;1S_Z|JJ_Z\rangle\varepsilon^\alpha(L_Z)^*\varepsilon^\beta(S_Z)^* \\ &\times\frac{M\varepsilon^\mu(p_1)\varepsilon^\nu(p_2)}{p_1^2+p_2^2-M^2}\Big\{g_{\alpha\mu}p_{1\nu}(p_2-p_1)_\beta + g_{\alpha\nu}p_{2\mu}(p_1-p_2)_\beta \\ &\quad +(p_2^2-p_1^2-M^2)g_{\alpha\nu}g_{\beta\mu}+(p_1^2-p_2^2-M^2)g_{\alpha\mu}g_{\beta\nu} \\ &\quad +\frac{M^2}{M^2-p_1^2-p_2^2}[g_{\mu\nu}p_{1\beta}(p_1-p_2)_\alpha + g_{\mu\nu}p_{2\beta}(p_2-p_1)_\alpha] \\ &\quad +\frac{M^2+p_1^2+p_2^2}{M^2-p_1^2-p_2^2}[g_{\mu\beta}p_{1\nu}(p_2-p_1)_\alpha + g_{\nu\beta}p_{2\mu}(p_1-p_2)_\alpha]\Big\}.\end{aligned} \tag{2.39c}$$

As required by gauge invariance, these expressions vanish when $p_1^2 = p_2^2 = 0$ and $\varepsilon^\mu(p_1) \to p_1^\mu$ or $\varepsilon^\nu(p_2) \to p_2^\nu$. The general P-wave result listed in Eq. (2.39c) may be further reduced[3] by employing the Clebsch-Gordan identities [15]

$$\begin{aligned}\sum_{L_Z,S_Z}\langle 1L_Z;1S_Z|00\rangle\varepsilon^\alpha(L_Z)^*\varepsilon^\beta(S_Z)^* &= \sqrt{\frac{1}{3}}(g^{\alpha\beta}-\frac{P^\alpha P^\beta}{M^2}) \\ \sum_{L_Z,S_Z}\langle 1L_Z;1S_Z|1J_Z\rangle\varepsilon^\alpha(L_Z)^*\varepsilon^\beta(S_Z)^* &= -\frac{i}{\sqrt{2}M}\epsilon^{\alpha\beta\gamma\delta}P_\gamma\,\varepsilon_\delta(J_Z)^* \\ \sum_{L_Z,S_Z}\langle 1L_Z;1S_Z|2J_Z\rangle\varepsilon^\alpha(L_Z)^*\varepsilon^\beta(S_Z)^* &= \varepsilon^{\alpha\beta}(J_Z)^*.\end{aligned} \tag{2.40}$$

We then find that $gg \to Q\bar{Q}[^3P_1^{(8)}]$ as well as $gg \to Q\bar{Q}[^3S_1^{(8)}]$ scattering vanishes when both incident gluons go on-shell [31, 32].

The projection formula in Eq. (2.35) can obviously be generalized to other parton channels besides $gg \to Q\bar{Q}[^{2S+1}L_J^{(1,8)}]$. We may insert any QCD amplitude which has a heavy quark and antiquark appearing in the final state and project out a reduced color-singlet or color-octet expression. Applying this general technique to the $q\bar{q} \to Q\bar{Q}$ scattering process pictured in Fig. 2.6, we find [31, 28]

$$\mathcal{A}(q(p_1)\bar{q}(p_2) \to Q\bar{Q}[^3S_1^{(8)}]_a) = \frac{1}{4(2\pi)^3}\sqrt{\frac{4\pi M}{q^0}}g_s^2\bar{v}(p_2)\gamma_\sigma T_a u(p_1)\varepsilon^\sigma(S_z)^*. \tag{2.41}$$

The squares of $2 \to 1$ amplitudes enter into the differential cross section for heavy pair production

[3]This reduction is not valid when calculating polarized cross sections. See Sec. 4.5.

$$d\sigma\left(a(p_1)b(p_2)\to Q\bar{Q}[^{2S+1}L_J^{(1,8)}](P)\right) = \frac{1}{4p_1\cdot p_2}\overline{\sum}\left|\mathcal{A}(ab\to Q\bar{Q}[^{2S+1}L_J^{(1,8)}])\right|^2 d\Phi_1(p_1+p_2;P) \tag{2.42}$$

where the barred summation symbol indicates that initial (final) spins and colors are averaged (summed) and $d\Phi_1$ denotes a one-body phase space factor. High and low energy effects are intertwined in this expression. In order to disentangle it, we follow Ref. [4] and match the integrated cross section onto the product of a short distance coefficient and a long distance NRQCD matrix element:

$$\sigma\left(ab\to Q\bar{Q}[^{2S+1}L_J^{(1,8)}]\right) = \frac{C_{\rm short}}{M_Q^{d-4}}\times\langle 0|\mathcal{O}_{1,8}^{Q\bar{Q}}(^{2S+1}L_J)|0\rangle. \tag{2.43}$$

The general structure of the operator whose vacuum-to-vacuum matrix element appears on the right hand side of this matching condition looks like

$$\mathcal{O}_{1,8}^{Q\bar{Q}}(^{2S+1}L_J) = \chi^\dagger K\psi\left(\sum_{m_J}\left|Q\bar{Q}[^{2S+1}L_J^{(1,8)}]\right\rangle\left\langle Q\bar{Q}[^{2S+1}L_J^{(1,8)}]\right|\right)\psi^\dagger K\chi, \tag{2.44}$$

where the matrix K denotes a product of color, spin and covariant derivative factors. The intermediate quark-antiquark state sandwiched in the middle

$$\left|Q\bar{Q}[^{2S+1}L_J^{(1,8)}]\right\rangle = \sum_{L_Z,S_Z}\sum_{s_1,s_2}\sum_{i,j}\int\frac{d^3q}{(2\pi)^3 2q^0}\delta(q^0-\frac{\vec{q}^2}{M}) \times Y^*_{LL_Z}(\hat{q})\langle\frac{1}{2}s_1;\frac{1}{2}s_2|SS_Z\rangle\langle LL_Z;SS_Z|JJ_Z\rangle\langle 3i;\bar{3}j|1,8\rangle\left|Q^i(q;s_1)\bar{Q}_j(-q;s_2)\right\rangle \tag{2.45}$$

is defined in the NRQCD effective theory in the same way as in full QCD. As a result, any arbitrariness in the definitions of the heavy pair production cross section and NRQCD matrix element cancels out of their ratio. The short distance coefficient appearing on the right hand side of Eq. (2.43) is convention independent.

All information related to the hard scattering process which creates the $Q\bar{Q}$ pair is encoded within $C_{\rm short}$. This same coefficient enters into the physical quarkonium production cross section

$$\sigma\left(ab\to Q\bar{Q}[^{2S+1}L_J^{(1,8)}]\to\psi_Q+X\right) = \frac{C_{\rm short}}{M_Q^{(d+1)-4}}\times\langle 0|\mathcal{O}_{1,8}^{\psi_Q}(^{2S+1}L_J)|0\rangle. \tag{2.46}$$

On the other hand, the accompanying long distance matrix element which specifies the probability that a $Q\bar{Q}[^{2S+1}L_J^{(1,8)}]$ pair hadronizes into a ψ_Q bound state is completely different from its counterpart in Eq. (2.43). The operator

$$\mathcal{O}_{1,8}^{\psi_Q}(^{2S+1}L_J) = \chi^\dagger K\psi \left(\sum_{m_J}\sum_X |\psi_Q + X\rangle\langle\psi_Q + X|\right)\psi^\dagger K\chi \tag{2.47}$$

has one unit greater mass dimension than $\mathcal{O}_{1,8}^{Q\bar{Q}}(^{2S+1}L_J)$ as can be verified by comparing the dimensions of heavy intermediate pair and nonrelativistically normalized ψ_Q states. The inverse powers of M_Q in cross section Eqs. (2.43) and (2.46) consequently differ by unity. The nonperturbative matrix element $\langle 0|\mathcal{O}_{1,8}^{\psi_Q}(^{2S+1}L_J)|0\rangle$ also cannot readily be calculated within NRQCD unlike its perturbative $\langle 0|\mathcal{O}_{1,8}^{Q\bar{Q}}(^{2S+1}L_J)|0\rangle$ counterpart. Simple multiplicity relations such as

$$\begin{aligned}\langle 0|\mathcal{O}_{1,8}^H(^3S_1)|0\rangle &= 3\langle 0|\mathcal{O}_{1,8}^H(^1S_0)|0\rangle \\ \langle 0|\mathcal{O}_{1,8}^H(^3P_J)|0\rangle &= (2J+1)\langle 0|\mathcal{O}_{1,8}^H(^3P_0)|0\rangle\end{aligned} \tag{2.48}$$

are obeyed exactly by the latter and approximately by the former. But the color-factor relation

$$\langle 0|\mathcal{O}_8^H(^{2S+1}L_J)|0\rangle = \frac{N_c^2-1}{2N_c}\langle 0|\mathcal{O}_1^H(^{2S+1}L_J)|0\rangle \tag{2.49}$$

which holds for $H = Q\bar{Q}$ certainly does not apply when $H = \psi_Q$. Numerical values for $\langle 0|\mathcal{O}_{1,8}^{\psi_Q}(^{2S+1}L_J)|0\rangle$ matrix elements must be extracted from experimental data.

2.2.2 Explicit matching calculation

In order to clarify the meaning of these NRQCD matching ideas, we explicitly evaluate the matching conditions specified in Eqns. (2.43) and (2.46) for one simple example [28]. We consider the gluon fusion formation of an η_Q pseudoscalar meson through an intermediate $Q\bar{Q}[^1S_0^{(1)}]$ pair. A straightforward computation yields the color-singlet cross section[4]

$$\sigma\left(gg \to Q\bar{Q}[^1S_0^{(1)}]\right) = \frac{\alpha_S^2}{384\pi^2}\frac{M}{q^0\hat{s}}\delta\left(1-\frac{M^2}{\hat{s}}\right) \tag{2.50}$$

[4]In this work, a hat over a Mandelstam variable means the variable is defined in the center of momentum frame of the partons.

and matrix element

$$\langle 0|\mathcal{O}_1^{Q\bar{Q}}(^1S_0)|0\rangle = \Big\langle 0\Big|\chi^\dagger\psi\Big|Q\bar{Q}[^1S_0^{(1)}]\Big\rangle\Big\langle Q\bar{Q}[^1S_0^{(1)}]\Big|\psi^\dagger\chi\Big|0\Big\rangle = \frac{N_c}{128\pi^5}\frac{M^3}{q^0}. \tag{2.51}$$

We derived this last result within the NRQCD effective theory by decomposing the Pauli fields

$$\begin{aligned}\psi_\alpha^i(x) &= \sum_{s=1}^{2}\int \frac{d^3p}{(2\pi)^3}\, b^i(p;s)\,\xi_\alpha(p,s)\,e^{-ip\cdot x}\\ \chi_{i\alpha}(x) &= \sum_{s=1}^{2}\int \frac{d^3p}{(2\pi)^3}\, c_i^\dagger(p;s)\,\eta_\alpha(p,s)\,e^{ip\cdot x}\end{aligned} \tag{2.52}$$

in terms of two-component spinors normalized according to

$$\sum_{s=1}^{2}\xi_\alpha(p,s)\,\xi_\beta^\dagger(p,s) = \sum_{s=1}^{2}\eta_\alpha(p,s)\,\eta_\beta^\dagger(p,s) = \delta_{\alpha\beta} \tag{2.53}$$

and single fermion creation and annihilation operators which satisfy the nonrelativistic anticommutation relations

$$\{b^i(p;s), b_j^\dagger(p';s')\} = \{c^i(p;s), c_j^\dagger(p';s')\} = (2\pi)^3\delta_j^i\,\delta_{ss'}\,\delta^{(3)}(p-p'). \tag{2.54}$$

Taking the ratio of (2.50) and (2.51), we deduce the short distance coefficient in matching condition (2.43)

$$\frac{C(gg\to Q\bar{Q}[^1S_0^{(1)}])_{\text{short}}}{M_Q^{d-4}} = \frac{1}{9}\frac{\pi^3\alpha_s^2}{M^2\hat{s}}\delta\left(1-\frac{M^2}{\hat{s}}\right) \tag{2.55}$$

and the gluon fusion cross section in matching condition (2.46):

$$\sigma\left(gg\to Q\bar{Q}[^1S_0^{(1)}]\to\eta_Q\right) = \frac{2}{9}\frac{\pi^3\alpha_s^2}{M^3\hat{s}}\delta\left(1-\frac{M^2}{\hat{s}}\right)\langle 0|\mathcal{O}_1^{\eta_Q}(^1S_0)|0\rangle. \tag{2.56}$$

If we recall the relation between the NRQCD matrix element and squared η_Q wavefunction at the origin (2.31)

$$\langle 0|\mathcal{O}_1^{\eta_Q}(^1S_0)|0\rangle = \frac{N_c}{2\pi}R(0)^2(1+O(v^4)), \tag{2.57}$$

we see that our result is consistent with the $O(\alpha_s^2)$ cross section

$$\sigma\left(gg \to Q\bar{Q}[^1S_0^{(1)}] \to \eta_Q\right) = \frac{1}{3}\frac{\pi^2\alpha_s^2}{M^3\hat{s}}\delta\left(1 - \frac{M^2}{\hat{s}}\right)R(0)^2 \tag{2.58}$$

previously reported in the literature [16].

Working in a similar fashion, we can decompose any color-singlet or color-octet cross section into products of short and long distance factors. We tabulate in Appendix A all $\mathcal{O}(\alpha_s^2)$ short distance squared amplitudes for $2 \to 1$ color-octet reactions which yield ψ_Q bound states at $\mathcal{O}(v^7)$ in the NRQCD velocity expansion. The corresponding long distance factors are simply given by appropriate NRQCD matrix elements for specific production channels. For example, the total squared amplitude for $gg \to Q\bar{Q}[^1S_0^{(1)}] \to \psi_Q$ scattering equals the product of the process-independent high energy expression listed in Eq. (A.2a) and the process-specific low energy matrix element $\langle 0|\mathcal{O}_8^{\psi_Q}(^1S_0)|0\rangle$:

$$\overline{\sum}\left|\mathcal{A}(gg \to Q\bar{Q}[^1S_0^{(1)}] \to \psi_Q)\right|^2 = \frac{5(4\pi\alpha_s)^2}{192M}\langle 0|\mathcal{O}_8^{\psi_Q}(^1S_0)|0\rangle. \tag{2.59}$$

Color-octet pair production in $2 \to 1$ collisions could represent an important source of quarkonia in fixed target experiments, and its impact has been studied [33, 30]. But before definite predictions can be made, numerical values for color-octet matrix elements must be known. Therefore, it will be important to consider quarkonia production at hadron colliders where we can use experimental data to determine these matrix element values.

2.3 Fragmentation

It is sometimes possible that higher order perturbative corrections can dominate given processes. Such is the case with quarkonia production at large transverse momentum. As an example, the lowest order diagram which contributes to color-singlet η_Q production through the process $gg \to Q\bar{Q}g$ is shown in Fig. 2.8. This diagram contributes at order α_s^3. Note that the quark propagator is far off-shell, of the order $p_\perp$.

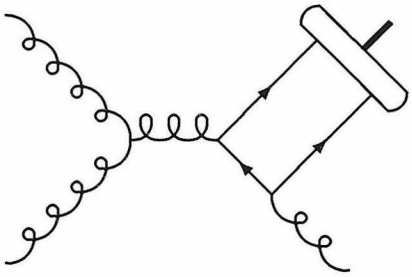

Figure 2.8: Typical Feynman diagram for producing η_Q at order α_s^3.

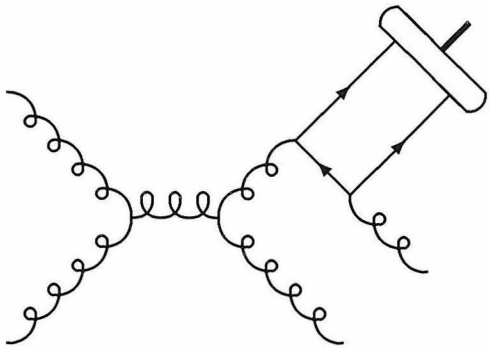

Figure 2.9: Fragmentation diagram for color-singlet η_Q production at order α_s^4. This diagram will dominate at high $p_\perp$ relative to the lower order diagram pictured in Fig. 2.8.

At order α_s^4 there are diagrams such as the one shown in Fig. 2.9. In most of phase space the gluons are off-shell also by an amount of the order of $p_\perp$. Thus the diagram in Fig. 2.9 is suppressed relative to the diagram in Fig. 2.8 by $\alpha_s(p_\perp)$. However, there are regions in phase space where the virtual gluon creating the $Q\bar{Q}$ pair is almost on-shell, of the order M_Q. This means the second diagram is enhanced by an amount $p_\perp^2/M_Q^2$. For large enough transverse momenta, this enhancement can compensate for the extra power of α_s, and this diagram will dominate the cross section. This is the basic idea behind fragmentation [34, 35].

The fragmentation cross section can be written in a factorized form. First there is some process which creates a nearly on-shell parton, which is going to fragment into the final particle of interest. For the example above, this would be $gg \to gg^*$, where the virtual gluon g^* has a low invariant mass q^2 relative to the transverse momentum,

i.e. $q^2 \ll p_\perp^2$. The second factor is the propagator for this parton, $1/q^2$. The final factor is the fragmentation function, which is the probability for the parton to create the final state particle, $g^* \to \eta_Q g$. Thus we write the cross section as [35]

$$d\sigma_{\eta_Q}(E) \approx \int_0^1 dz\, d\hat{\sigma}_g(E/z) D_{g\to\eta_Q}(z, M_Q), \tag{2.60}$$

where $d\hat{\sigma}_g$ is the differential cross section for producing an on shell gluon. Implicit in the cross section is that first a gluon of energy E/z is produced, which splits into an η_Q carrying a fraction z of the initial energy. Note that all the energy dependence is contained in the cross section $d\hat{\sigma}$, while all dependence on the mass of the heavy quarks is contained in the fragmentation function $D_{g\to\eta_Q}(z, M_Q)$.

It is possible that the parton that splits into the quarkonia originally split from a higher energy parton. This process will give rise to large logarithms of the order E/M_Q. To keep the factorization of the energy and mass dependence, a factorization scale μ is introduced. Thus to all orders in α_s, we can write the fragmentation cross section for producing a quarkonia state H with energy E as [35]

$$d\sigma_H(E) = \sum_i \int_0^1 dz\, d\hat{\sigma}_i(E/z, \mu) D_{i\to H}(z, \mu), \tag{2.61}$$

where the sum is over all parton types i.

The power of the fragmentation formalism is that it is possible to calculate $D_{i\to H}(z, \mu)$ at the scale $\mu = M_Q$. Then the fragmentation functions can be evolved to an arbitrary scale μ by

$$\mu \frac{\partial}{\partial \mu} D_{i\to H}(z, \mu) = \sum_j \int_z^1 \frac{dy}{y} P_{i\to j}(z/y, \mu) D_{j\to H}(y, \mu), \tag{2.62}$$

where the function $P_{i\to j}(x, \mu)$ is the Altarelli-Parisi function [36] for the splitting of parton i into parton j with momentum fraction x. Thus, we can do a perturbative calculation in $\alpha_s(M_Q)$ to calculate the fragmentation function at a scale M_Q, and then we can evolve this to the correct scale of the process of interest.

Chapter 3 Color-singlet Production

During the past few years, there has been renewed interest in the study of heavy quarkonium systems. Much of the recent work on this subject has been stimulated by large discrepancies between old predictions and new observations of ψ and Υ production at several experimental facilities. Orders of magnitude disagreements between theory and data have seriously undermined the conventional CSM picture of quarkonia formation [12, 13, 14, 15, 16]. In this model, charmonia and bottomonia mesons are presumed to exclusively originate from short distance processes that create heavy quark-antiquark pairs in colorless configurations. The quantum numbers of pairs produced in high energy collisions on time scales short compared to Λ_{QCD} are required to precisely match those of the final state hadrons into which they nonperturbatively evolve. Although this CSM picture is simple, it does not explain several gross features of recent charmonia and bottomonia data collected at the Fermilab Tevatron [37, 38, 39]. It consequently must be abandoned as a complete theory.

Even though the CSM cannot be considered the correct description of quarkonia in all cases, it is often true that the dominant contributions to a given process are those that can be calculated in this model alone. Also, it is important to understand how calculations in the past are related to those of NRQCD. One of the advantages of NRQCD is that it reduces to the CSM as $v \to 0$. In this section, as an example of the CSM, we calculate quarkonia production at an e^+e^- collider. Then we discuss color-singlet quarkonia production in hadron collision.

3.1 An Example: Quarkonia production at e^+e^- collider

Braaten and Chen have suggested that a clean signature of the color-octet mechanism may be observable in ψ_Q production at electron-positron colliders [40]. These authors have noted that the angular distribution of colored $Q\bar{Q}$ pairs near the endpoint region may qualitatively differ from that of their colorless counterparts. If this effect could be observed, it would support the color-octet production picture. It might also permit an independent determination of the numerical values for certain NRQCD matrix elements.

Before the search for color-octet quarkonia production in e^+e^- annihilation can begin, one must first know the precise CSM prediction. Within the NRQCD framework, the color-singlet cross section is also expected to be quite accurate for all energies except near the endpoint region [40]. In this section, we therefore build upon previous studies reported in the literature [41, 42, 43, 44] and calculate the complete $\mathcal{O}(\alpha_s^2)$ color-singlet cross section for $e^+e^- \to \psi_Q + X$ scattering. We examine the contribution to ψ_Q production from the short distance modes $e^+e^- \to Q\bar{Q}[^3S_1^{(1)}] + g + g$ and $e^+e^- \to Q\bar{Q}[^3S_1^{(1)}] + Q + \bar{Q}$,[1] and we derive a closed form expression for the differential cross section. We then discuss the implications of the CSM result for direct J/ψ observations at CLEO. Finally, we compare heavy quark fragmentation predictions with the color-singlet cross section and determine the energy scale at which fragmentation approximations become reliable.

3.1.1 Color-singlet ψ_Q production

The simplest parton level process which mediates color-singlet production of $J^{PC} = 1^{--}$ quarkonia is given by $e^+e^- \to Q\bar{Q}[^3S_1^{(1)}] + g + g$. Color, parity and charge conjugation conservation require two gluons to appear in the final state along with the colorless $Q\bar{Q}[^3S_1^{(1)}]$ pair. This channel consequently contributes to the ψ_Q cross

[1] We indicate the angular momentum and color-singlet quantum numbers of the $Q\bar{Q}$ pair which hadronizes into the final state ψ_Q meson inside square brackets.

section starting at $\mathcal{O}(\alpha_s^2)$. Color singlet production also proceeds at the same order in perturbative QCD through the mode $e^+e^- \to Q\bar{Q}[^3S_1^{(1)}] + Q + \bar{Q}$. These two distinct reactions have been considered separately in the literature [41, 42, 43, 44]. We will reexamine their joint impact upon ψ and Υ production and derive a closed form analytic expression for $d^2\sigma/dE_3\, d\cos\theta_3$. We can then compare the relative magnitudes of the gluon and quark processes as a function of center-of-mass energy $\sqrt{S}$.

The leading order diagrams which mediate $e^+(p_1)\, e^-(p_2) \to Q\bar{Q}[^3S_1^{(1)}](p_3) + g(p_4) + g(p_5)$ and $e^+(p_1)\, e^-(p_2) \to Q\bar{Q}[^3S_1^{(1)}](p_3) + Q(p_4) + \bar{Q}(p_5)$ scattering are illustrated in Figs. 3.1 and 3.2. The hard collisions pictured in the figures form on short time scales a heavy quark and antiquark which fly out from the primary interaction point in nearly parallel directions and almost on-shell. The $Q\bar{Q}$ pair then evolves over a much longer time interval into a physical ψ_Q bound state. Working within the NRQCD framework and using computational methods discussed in Sec. 2.2 and Refs. [15, 31, 28], one can straightforwardly calculate the amplitudes for these processes. Their squares factorize into products of short distance coefficient functions and long distance NRQCD matrix elements.

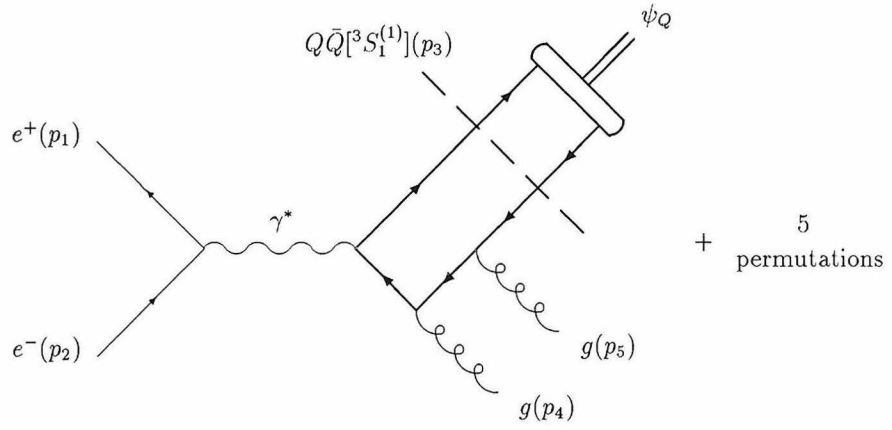

Figure 3.1: Leading order Feynman graphs which mediate $e^+e^- \to \gamma^* \to Q\bar{Q}[^3S_1^{(1)}] + g + g \to \psi_Q + X$ scattering.

Integrating the squared amplitudes over the three particle phase space factor

$$d\Phi_3 = (2\pi)^4\delta^4(p_1 + p_2 - p_3 - p_4 - p_5)\prod_{i=3}^{5}\frac{d^3p_i}{(2\pi)^3 2E_i} \tag{3.1}$$

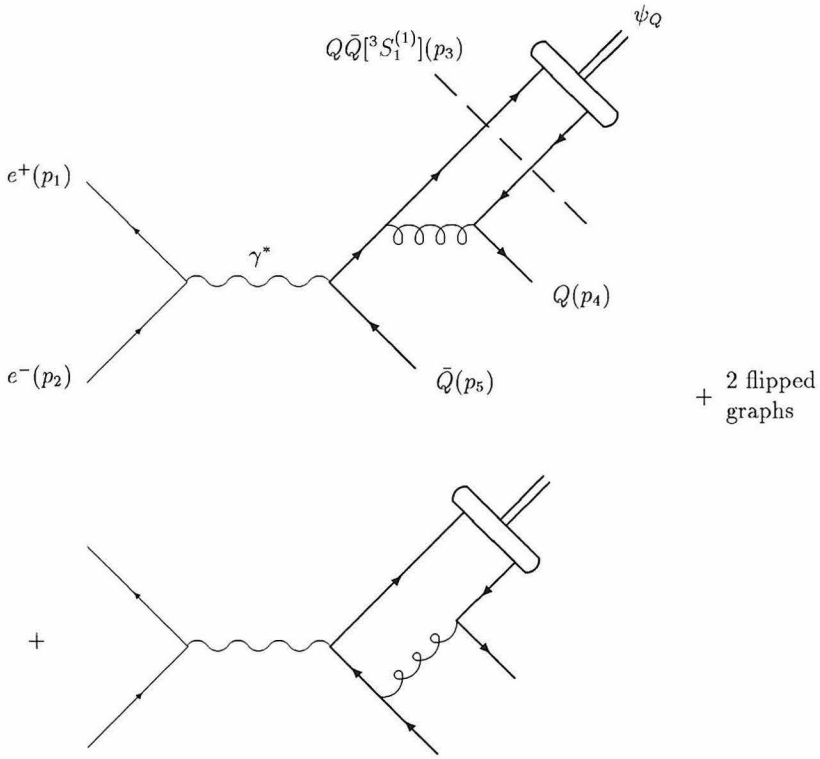

Figure 3.2: Leading order Feynman graphs which mediate $e^+e^- \to \gamma^* \to Q\bar{Q}[^3S_1^{(1)}] + Q + \bar{Q} \to \psi_Q + X$ scattering.

is somewhat involved. As a simplifying measure, we rescale all dimensionful quantities relative to the beam energy E and work with the dimensionless variables $z_i = E_i/E$, $\vec{q}_i = \vec{p}_i/E$, $x_i = \cos\theta_i$ and $\delta = 2M_Q/E$. The phase space factor for the reaction with gluons in the final state can then be reduced to the form [45]

$$d\Phi_3 = \frac{(2\pi)^{-4}}{8} E^2 \frac{dz_3\, dx_3\, dz_-\, dw}{\sqrt{(1-K^2)(1-x_3^2)-w^2}} \tag{3.2}$$

where

$$z_- = z_4 - z_5 \tag{3.3a}$$

$$|\vec{q}_-| = \sqrt{4 - 4z_3 + \delta^2 + z_-^2} \tag{3.3b}$$

$$|\vec{q}_3| = \sqrt{z_3^2 - \delta^2} \tag{3.3c}$$

$$K = \frac{z_-(2-z_3)}{|\vec{q}_-||\vec{q}_3|} \tag{3.3d}$$

$$w = x_- + K x_3. \tag{3.3e}$$

We can use the same result for the quark process with the simple alteration $|\vec{q}_-| = \sqrt{4 - 4z_3 + z_-^2}$.

The available phase space volume clearly depends upon the masses of the final state bodies. For the $e^+e^- \to Q\bar{Q}[^3S_1^{(1)}] + g + g$ channel, the limits of integration for the remaining energy and angular variables in eq. (3.2) are given by

$$\delta \leq z_3 \leq 1 + \frac{\delta^2}{4} \tag{3.4a}$$

$$-1 \leq x_3 \leq 1 \tag{3.4b}$$

$$-\sqrt{z_3^2 - \delta^2} \leq z_- \leq \sqrt{z_3^2 - \delta^2} \tag{3.4c}$$

$$-\sqrt{(1-K^2)(1-x_3^2)} \leq w \leq \sqrt{(1-K^2)(1-x_3^2)}. \tag{3.4d}$$

The corresponding limits for the $e^+e^- \to Q\bar{Q}[^3S_1^{(1)}] + Q + \bar{Q}$ mode

$$\delta \leq z_3 \leq 1 \tag{3.5a}$$

$$-1 \leq x_3 \leq 1 \tag{3.5b}$$

$$-\sqrt{\frac{(4-4z_3)(z_3^2-\delta^2)}{4-4z_3+\delta^2}} \leq z_- \leq \sqrt{\frac{(4-4z_3)(z_3^2-\delta^2)}{4-4z_3+\delta^2}} \tag{3.5c}$$

$$-\sqrt{(1-K^2)(1-x_3^2)} \leq w \leq \sqrt{(1-K^2)(1-x_3^2)} \tag{3.5d}$$

are more tight due to the additional heavy quark and antiquark in the final state.

After inserting the averaged squared amplitudes and reduced phase space factors into the formula

$$d\sigma = \frac{1}{8E^2}\overline{\sum}|\mathcal{A}|^2 d\Phi_3, \tag{3.6}$$

we can analytically integrate over w and z_- and obtain differential expressions of the form

$$\frac{d^2\sigma}{dE_3 d\cos\theta_3}\left(e^+(p_1)e^-(p_2) \to \gamma^* \to \psi_Q(p_3) + X\right) = S(E_3)\left[1 + \alpha(E_3)\cos^2\theta_3\right]. \tag{3.7}$$

We display the resulting $S(z_3)$ and $\alpha(z_3)$ functions for the $e^+e^- \to Q\bar{Q}[^3S_1^{(1)}] + g + g$ and $e^+e^- \to Q\bar{Q}[^3S_1^{(1)}] + Q + \bar{Q}$ processes in Appendix B. As a check, one can

verify that $|\alpha_{\rm gluon}|$ and $|\alpha_{\rm quark}|$ do not exceed unity within their allowed z_3 ranges as required by the general constraints discussed in Appendix C. The total $\mathcal{O}(\alpha_s^2)$ angular coefficient function

$$\alpha_{\rm total} = \frac{S_{\rm gluon}\,\alpha_{\rm gluon} + S_{\rm quark}\,\alpha_{\rm quark}}{S_{\rm gluon} + S_{\rm quark}} \tag{3.8}$$

also respects the bound $-1 \leq \alpha_{\rm total} \leq 1$.

Another important check can be performed by considering the high energy behavior of the $S(z_3)$ and $\alpha(z_3)$ functions. In the $z_3 \gg \delta$ limit, the color-singlet cross section reduces to [45]

$$\frac{d^2\sigma}{dz_3 d\cos\theta_3}(e^+e^- \to \psi_Q + X) = \frac{4\pi}{243}\frac{(\alpha_s\alpha_{EM}\mathcal{Q}_Q)^2}{m_Q^3 E^2}\left\langle 0|\mathcal{O}_1^{\psi_Q}(^3S_1)|0\right\rangle\left[1+\cos^2\theta_3\right] \times \frac{z_3(1-z_3)^2(16-32z_3+72z_3^2-32z_3^3+5z_3^4)}{(2-z_3)^6}, \tag{3.9}$$

where $\mathcal{Q}_Q$ is the charge of the quark in units of the electron charge. After integrating over $\cos\theta_3$ and recalling the relation $\left\langle 0|\mathcal{O}_1^{\psi_Q}(^3S_1)|0\right\rangle = 9|\mathcal{R}(0)|^2/2\pi$ between the color-singlet NRQCD matrix element and the ψ_Q wavefunction at the origin [4], we can write the ψ_Q energy distribution as

$$\frac{d\sigma}{dz_3}(e^+e^- \to \psi_Q + X) = 2\sigma(e^+e^- \to Q\bar{Q}) \times \mathcal{D}_{Q\to\psi_Q}(z_3) \tag{3.10}$$

where $\mathcal{D}_{Q\to\psi_Q}(z_3)$ denotes the heavy quark fragmentation function originally calculated in Ref. [34]. The complete $\mathcal{O}(\alpha_s^2)$ color-singlet cross section thus correctly reproduces known fragmentation results at high energies.

3.1.2 Direct J/ψ production at CLEO

J/ψ production is currently under study at CLEO[46, 47]. Charmonia observed at this e^+e^- facility mainly come from B meson decays. However, a clean sample of ψ's originating from continuum production can be obtained by imposing a lower momentum cut on their dilepton decay products. Various characteristics of the resulting direct J/ψ data sample can then be compared with predictions based upon color-

singlet and color-octet production mechanisms. Such experimental investigations are underway.

The angular distribution of direct J/ψ mesons represents one observable which can be measured at CLEO. In Fig. 3.3, we plot the CSM prediction for the angular coefficient function α. The results displayed in the figure are based upon the input parameter values $E = 5.29$ GeV, $m_c = 1.48$ GeV, $\alpha_s(2m_c) = 0.28$, $\alpha_{EM}(2m_c) = 0.0075$, $\mathcal{Q}_c = 2/3$ and $\left\langle 0|\mathcal{O}_1^{J/\psi}(^3S_1)|0\right\rangle = 1.2\ GeV^3$. The dashed curve illustrates the function $\alpha_{\rm gluon}$ associated with $e^+e^- \to c\bar{c}[^3S_1^{(1)}] + g + g$ scattering. The shape of this

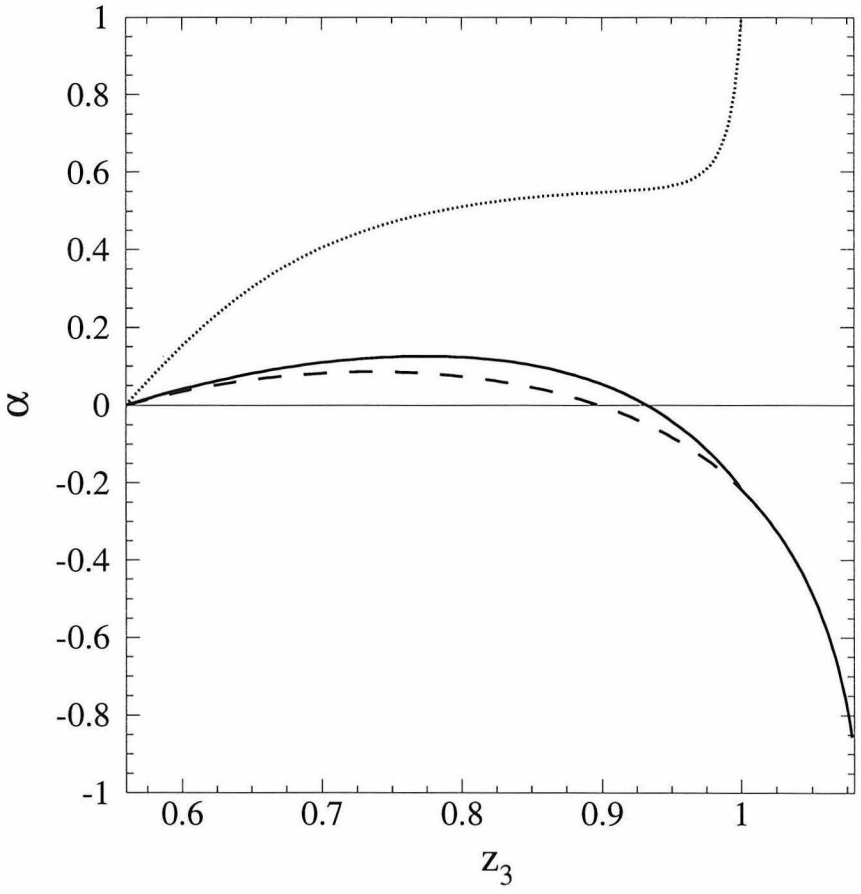

Figure 3.3: Angular coefficient functions $\alpha_{\rm gluon}$ (dashed line), $\alpha_{\rm quark}$ (dotted line) and $\alpha_{\rm total}$ (solid line) plotted against dimensionless energy variable z_3.

curve agrees with numerical results of Driesen *et al.* reported in Ref. [43]. The dotted line in Fig. 3.3 depicts the function $\alpha_{\rm quark}$ originating from the $e^+e^- \to c\bar{c}[^3S_1^{(1)}] + c + \bar{c}$ mode. The shape of $\alpha_{\rm quark}$ is clearly quite different than that of $\alpha_{\rm gluon}$. But since $S_{\rm quark}$

is substantially smaller than $S_{\rm gluon}$ at CLEO energies, it has only a small impact upon the total color-singlet function $\alpha_{\rm total}$ which is represented by the solid curve in Fig. 3.3. It is important to note that $\alpha_{\rm total}$ is predicted within the CSM to be negative at the largest allowed values for z_3. On the other hand, color-octet effects may render $\alpha_{\rm total}$ positive in the endpoint region [40]. The angular distribution of the most energetic J/ψ's at CLEO can therefore provide a valuable test of the color-octet mechanism.

The energy distribution of direct J/ψ's is another quantity which can be used to probe theories of quarkonia production. In Fig. 3.4, we display the separate contributions to $d\sigma/dz_3$ from the $e^+e^- \to c\bar{c}[^3S_1^{(1)}]+g+g$ and $e^+e^- \to c\bar{c}[^3S_1^{(1)}]+c+\bar{c}$ channels along with the total CSM prediction. The sensitivity of this energy observable to the

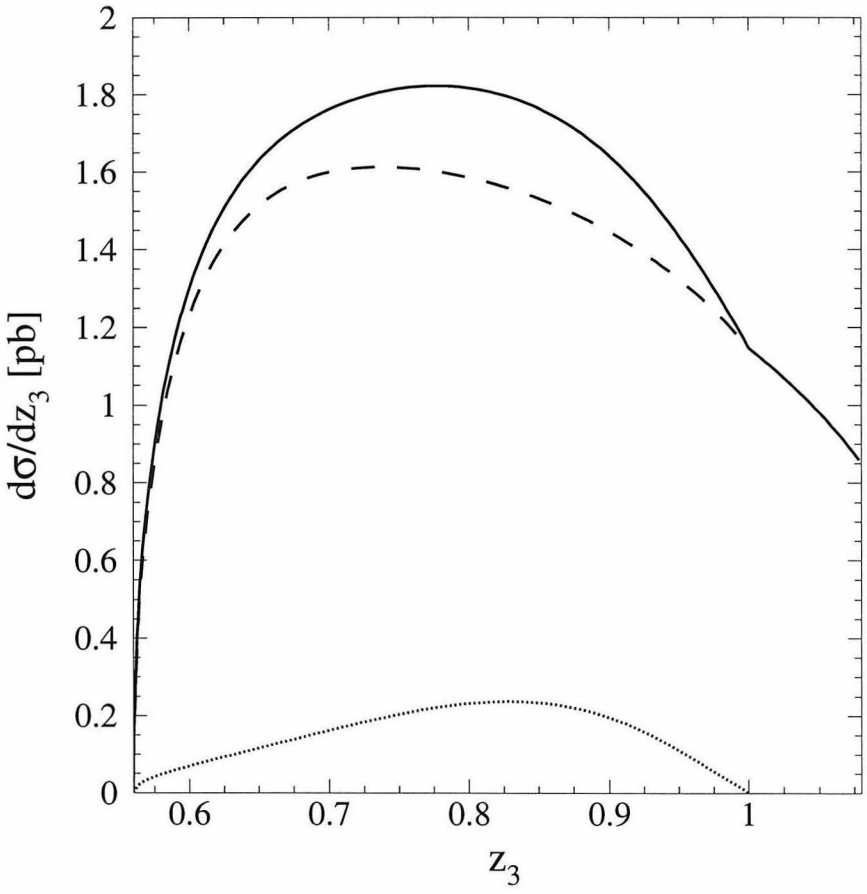

Figure 3.4: Contributions to $d\sigma/dz_3$ from the gluon (dashed line) and quark (dotted line) modes plotted against z_3. The CSM prediction for the total direct J/ψ energy distribution is represented by the solid curve.

charm mode is more pronounced than that of the angular coefficient function. The

areas underneath the dashed, dotted and solid curves respectively equal 0.74 pb, 0.07 pb and 0.81 pb. The quark process thus contributes at the 10% level to direct J/ψ production at CLEO.

The $e^+e^- \to c\bar{c}[^3S_1^{(1)}]+c+\bar{c}$ mode is significantly phase space suppressed compared to $e^+e^- \to c\bar{c}[^3S_1^{(1)}]+g+g$ at CLEO energies. As a result, its impact upon charmonia observables is minor. However, it is interesting to examine the relative importance of these two color-singlet channels as a function of center-of-mass energy. We plot in Fig. 3.5 the modes' separate contributions to the integrated J/ψ cross section along with their sum versus $\sqrt{S} = 2E$. We also display the integral of the charm quark fragmentation approximation (3.9). At low energies, the charm quark mode is negligible compared to its gluon counterpart. At larger values of $\sqrt{S}$, it becomes relatively more important. Finally, in the charm fragmentation limit $\sqrt{S} \gg m_c$, the quark mode dominates.

As can be seen in Fig. 3.5, the charm quark fragmentation curve rapidly asymptotes to the $e^+e^- \to c\bar{c}[^3S_1^{(1)}] + c + \bar{c}$ cross section. But it is important to note that the crossover point at which the rates for the charm and gluon modes become equal occurs around $\sqrt{S} \simeq 50$ GeV. Consequently, the fragmentation approximation does *not* accurately reflect the total color-singlet cross section until $\sqrt{S}$ exceeds $2m_c$ by more than an order of magnitude. This result for J/ψ production at lepton colliders is quite different than that for hadron accelerators. Previous investigations have found that fragmentation approximations are reasonably trustworthy for production of ψ's at the Tevatron with $p_\perp \gtrsim 10$ GeV [31, 28]. The moral we thus draw from this study of charmonia at CLEO is that the validity of fragmentation predictions must be carefully checked on a case-by-case basis.

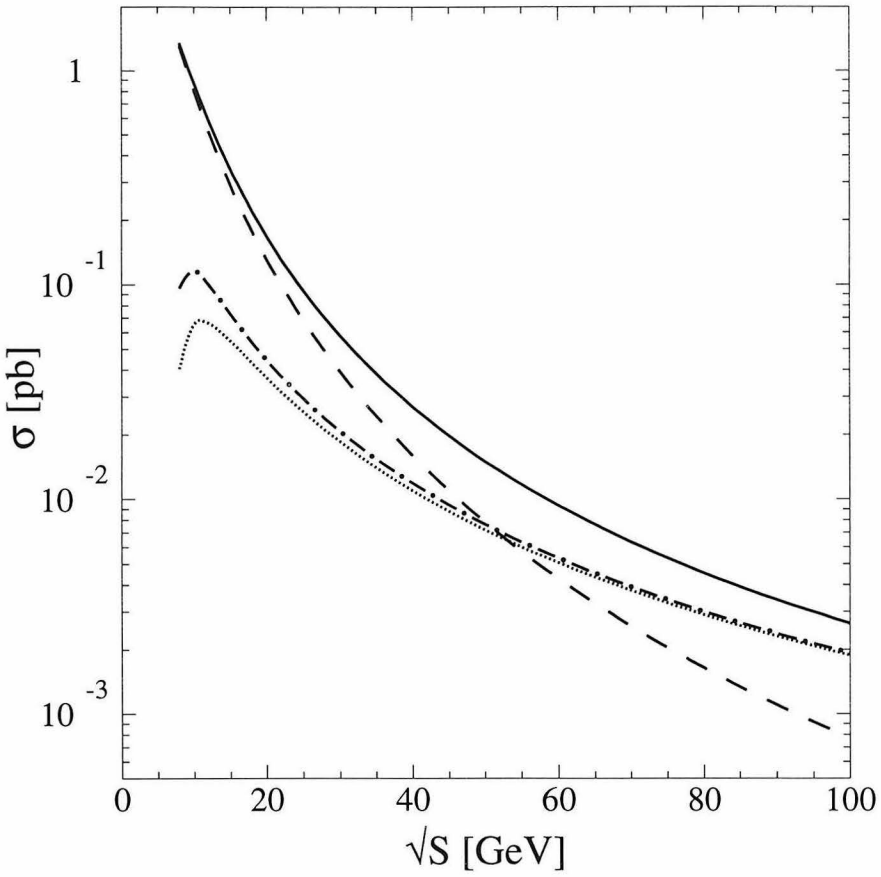

Figure 3.5: Integrated cross sections for the gluon (dashed line) and charm quark (dotted line) modes plotted as a function of $\sqrt{S}$. The sum of the two is shown by the solid curve. The approximate charm quark fragmentation cross section is depicted by the dot-dashed curve.

3.2 Color-singlet quarkonia production for hadroproduction

The cross sections for producing color-singlet quarkonia are well known [16, 48]. Nonperturbative physics is factorized into the wavefunction, or derivatives of the wavefunction, evaluated at the origin. This wavefunction can be related to the color-singlet matrix elements appearing in NRQCD. In this section, We will give a general overview on how to calculate a reaction in the color-singlet model.

The amplitude for some process can be written as [16]

$$\mathcal{A}(P) = \int \frac{d^4q}{(2\pi)^4} Tr[O(P,q)\phi(P,q)], \tag{3.11}$$

where P is the momentum of the outgoing quarkonium, $O(P,q)$ is the perturbative part of the amplitude and $\phi(P,q)$ is the Bethe-Salpeter wavefunction, which includes the heavy quark spinors. The quarkonia is pictured as a nonrelativistic bound state, with relative momentum q. The Bethe-Salpeter wavefunction can be decomposed into a state with spin S, orbital angular momentum L and total angular momentum J as [16]

$$\phi(P,q) = 2\pi\delta\left(q^0 - \frac{|\vec{q}|^2}{2M_Q}\right) \sum_{L_Z,S_Z} \psi_{LL_Z}(\vec{q}) P_{SS_Z}(P,q) \langle LL_Z; SS_Z | JJ_Z \rangle, \tag{3.12}$$

where P_{SS_Z} is the same as in Eq. (2.36), and $\psi_{LL_Z}(\vec{q})$ is the nonrelativistic wavefunction.

Since the wavefunction has little support for $|\vec{q}| \gtrsim M_Q$, it is possible to expand in powers of $|\vec{q}|$ and to keep only the first nonvanishing piece. For $L = 0$ states we can set $|\vec{q}| = 0$. Plugging Eq. (3.12) into Eq. (3.11) leads to,

$$\mathcal{A}(P) = \frac{1}{\sqrt{4\pi}} R(0) Tr[O(P,0) P_{SS_Z}(P,0)], \tag{3.13}$$

where we have introduced the radial wavefunction evaluated as the origin. This wavefunction appears from integrating the total bound state wavefunction $\psi_{LL_Z}(\vec{q})$ over q,

$$\frac{1}{\sqrt{4\pi}} R(0) = \int \frac{d^3q}{(2\pi)^3} \psi_{00}(\vec{q}). \tag{3.14}$$

If the interesting state has nonvanishing L, higher order in $\vec{q}$ is required. Plugging in the correct form of the spin projection P_{SS_Z} into Eq. (3.13), and taking the trace, results in the color-singlet amplitude for the given process.

The lowest order process in α_s which can produce a color-singlet quarkonia would be $gg \to Q\bar{Q}[^{2S+1}L_J^{(1)}]$, which then hadronizes into a final state particle with the

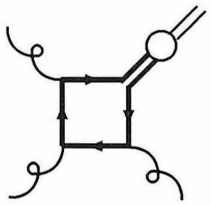

Figure 3.6: Feynman diagram for lowest order color-singlet ψ_Q production. There are five more diagrams where the gluon legs are permuted.

same angular quantum numbers as the intermediate $Q\bar{Q}$ pair. At this order, only ${}^1S_0$ and ${}^3P_{0,2}$ quantum numbers are possible. Thus, we are able to produce η_Q and $\chi_{Q0,2}$ at $\mathcal{O}(\alpha_s^2)$. These particles are produced with small transverse momenta and are, in general, lost down the beam pipe at a collider facility, but can be important at fixed target experiments.

It is first possible to produce a color-singlet ψ or Υ at order α_s^3. This process takes place through the box-like diagram of Fig. 3.6. The cross section for this process is [16]

$$\frac{d\sigma}{d\hat{t}}({}^3S_1) = \frac{10\pi^2\alpha_s^3 M}{81\hat{s}^2}\langle 0|\mathcal{O}_1^{\psi_Q}({}^3S_1)|0\rangle \frac{\hat{s}^2(\hat{s}-M^2)^2+\hat{t}^2(\hat{t}-M^2)^2+\hat{u}^2(\hat{u}-M^2)^2}{(\hat{s}-M^2)^2(\hat{t}-M^2)^2(\hat{u}-M^2)^2}. \tag{3.15}$$

The relation between NRQCD matrix elements and the radial wave function given in Eq. (2.31) has been used to write this cross section.

Chapter 4 Color-octet Production

Color-singlet quarkonium production has been studied for years. Leading order color-singlet differential cross sections were calculated a decade ago [16, 48, 49], and some total cross section formulae have been evaluated at next-to-leading order as well [50]. In contrast, color-octet contributions to quarkonium processes have only recently begun to be considered. While the latter mechanism may be less familiar than the former, it is certainly not less important. As we saw in Sec. 2.1 color-singlet and color-octet graphs arise at the same order in α_s and in v. Moreover, the color-octet diagrams dominate at high energies. So a complete analysis of quarkonium production at hadron colliders must include both mechanisms. In this section we continue the discussion in Sec. 2.2 to order α_s^3, which is relevant to a $p\bar{p}$ collider. We then proceed to compare our theoretical cross sections to data from the Tevatron. To normalize our cross section, we need to have the NRQCD production matrix elements. Since the values of these matrix elements are not known, we extract their values from the data. Finally we discuss polarization of ψ's as a potential test of NRQCD.

4.1 Cross sections to Order α_s^3

In order to be experimentally detectable, quarkonia must be created at collider facilities with nonvanishing transverse momenta so that they are not lost down the beampipe. Hadrons resulting from $2 \to 1$ scattering processes typically have small $p_\perp$ comparable to the QCD scale. The production of quarkonia with nonnegligible transverse momenta therefore mainly proceeds through $2 \to 2$ collisions. Such reactions start at $\mathcal{O}(\alpha_s^3)$ via the parton channels $q\bar{q} \to Q\bar{Q}[^{2S+1}L_J^{(1,8)}]g$, $gq \to Q\bar{Q}[^{2S+1}L_J^{(1,8)}]q$ and $gg \to Q\bar{Q}[^{2S+1}L_J^{(1,8)}]g$.

The Feynman diagrams which mediate quarkonia production in these color-octet channels are illustrated in Figs. 4.1, 4.2, and 4.3. The shaded circles appearing in the

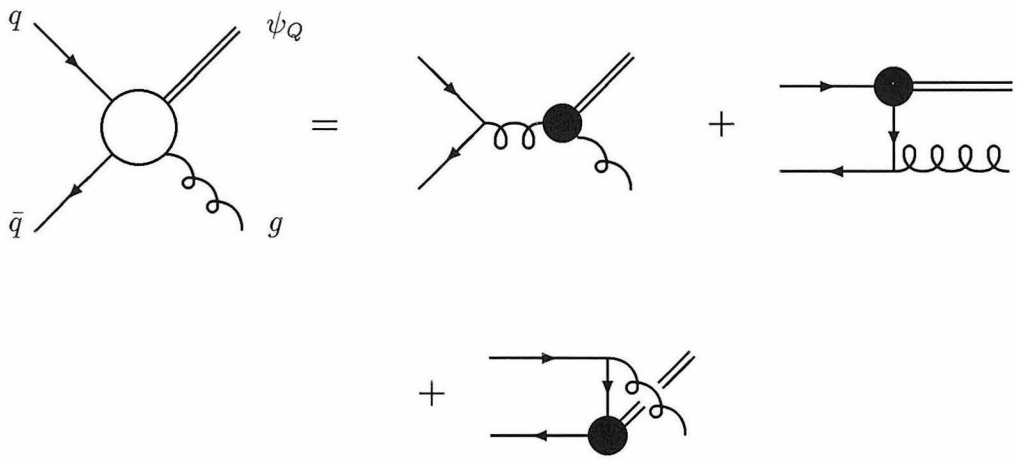

Figure 4.1: Color-octet diagrams which mediate $q\bar{q} \to \psi_Q g$. The shaded circles appearing in these graphs represent the $q\bar{q} \to \psi_Q$ and $gg \to \psi_Q$ amplitudes pictured in Figs. 2.6 and 2.7.

figure represent the $gg \to Q\bar{Q}[^1S_0^{(1)}]$, $gg \to Q\bar{Q}[^3S_1^{(1)}]$ and $gg \to Q\bar{Q}[^3P_J^{(8)}]$ amplitudes in Eq. (2.39). The $q\bar{q} \to \psi_Q g$ and $gq \to \psi_Q q$ diagrams pictured in Figs. 4.1 and 4.2 can readily be squared using standard spinor summation techniques. On the other hand, conventional evaluation of the gluon channel graphs in Fig. 4.3 represents a formidable computational task. It is therefore advisable to find a more tractable method for calculating the color-octet contributions to $gg \to \psi_Q g$ scattering.

We adopt a simple helicity amplitude technique [28] to sum and square the gluon graphs in Fig. 4.3. We first choose the following explicit representations for the gluon momenta and polarization vectors shown in the figure:

$$\begin{aligned} p_1 &= \frac{\sqrt{\hat{s}}}{2}(1,0,0,1), \\ p_2 &= \frac{\sqrt{\hat{s}}}{2}(1,0,0,-1), \\ p_4 &= \frac{\hat{s}-M^2}{2\sqrt{\hat{s}}}(1,0,\sin\theta,-\cos\theta), \end{aligned} \tag{4.1}$$

$$\begin{aligned} \varepsilon_1^+ = \varepsilon_2^- &= -\frac{1}{\sqrt{2}}(0,1,i,0) \\ \varepsilon_1^- = \varepsilon_2^+ &= \frac{1}{\sqrt{2}}(0,1,-i,0) \end{aligned} \tag{4.2}$$

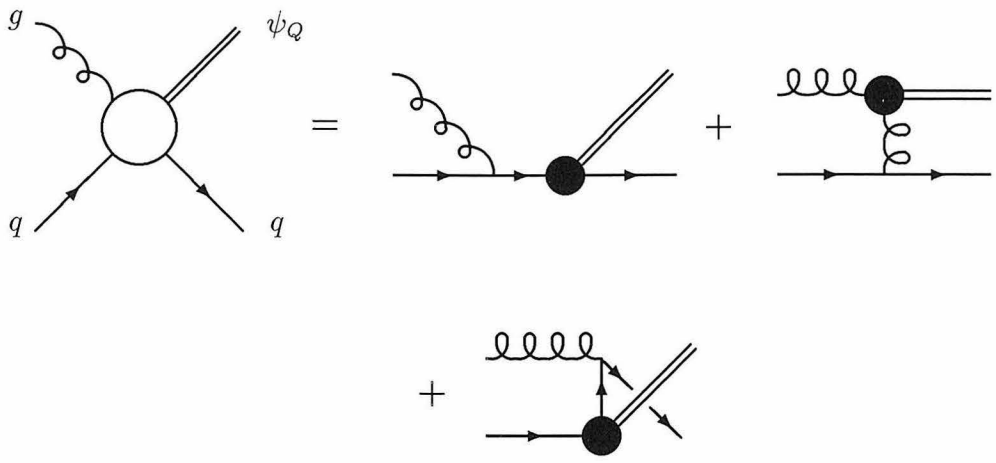

Figure 4.2: Color-octet diagrams which mediate $gq \to \psi_Q q$. The shaded circles appearing in these graphs represent the $q\bar{q} \to \psi_Q$ and $gg \to \psi_Q$ amplitudes pictured in Figs. 2.6 and 2.7.

$$(\varepsilon_4^{\pm})^* = \frac{1}{\sqrt{2}}(0, \pm 1, i\cos\theta, i\sin\theta).$$

We next boost the the heavy pair's four-momentum from its primed rest frame to the unprimed parton center-of-momentum frame:

$$p_3' = (M, 0, 0, 0) \to p_3 = \left(\frac{\hat{s} + M^2}{2\sqrt{\hat{s}}}, 0, -\frac{\hat{s} - M^2}{2\sqrt{\hat{s}}}\sin\theta, \frac{\hat{s} - M^2}{2\sqrt{\hat{s}}}\cos\theta\right). \tag{4.3}$$

We also Lorentz transform the rest frame polarization vectors

$$(\varepsilon_3'^{\,(h=1)})^* = -\sqrt{\frac{1}{2}}\begin{pmatrix} 0 \\ 1 \\ -i \\ 0 \end{pmatrix},$$

$$(\varepsilon_3'^{\,(h=0)})^* = \begin{pmatrix} 0 \\ 0 \\ 0 \\ 1 \end{pmatrix}, \tag{4.4}$$

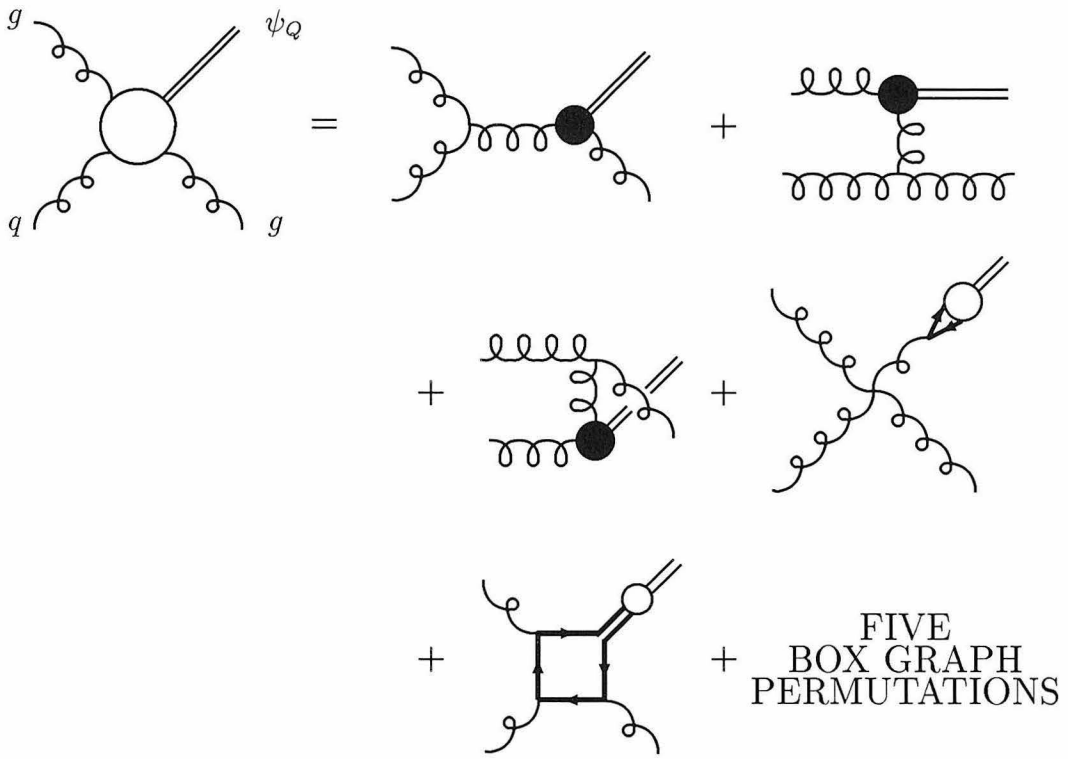

Figure 4.3: Color-octet diagrams which mediate $gg \to \psi_Q g$. The shaded circles appearing in these graphs represent the $gg \to \psi_Q$ amplitude pictured in Fig. 2.7.

$$(\varepsilon_3'^{\,(h=-1)})^* = \sqrt{\frac{1}{2}} \begin{pmatrix} 0 \\ 1 \\ i \\ 0 \end{pmatrix},$$

and tensors

$$(\varepsilon_3'^{\,(h=0)})^* = \sqrt{\frac{2}{3}} \begin{pmatrix} 0 & 0 & 0 & 0 \\ 0 & -\frac{1}{2} & 0 & 0 \\ 0 & 0 & -\frac{1}{2} & 0 \\ 0 & 0 & 0 & 1 \end{pmatrix},$$

$$(\varepsilon_3'^{\,(h=\pm 1)})^* = \mp\frac{1}{2} \begin{pmatrix} 0 & 0 & 0 & 0 \\ 0 & 0 & 0 & 1 \\ 0 & 0 & 0 & \mp i \\ 0 & 1 & \mp i & 0 \end{pmatrix}, \tag{4.5}$$

$$(\varepsilon_3'^{\,(h=\pm 2)})^* = \frac{1}{2}\begin{pmatrix} 0 & 0 & 0 & 0 \\ 0 & 1 & \mp i & 0 \\ 0 & \mp i & -1 & 0 \\ 0 & 0 & 0 & 0 \end{pmatrix},$$

of $J = 1$ and $J = 2$ $Q\bar{Q}$ pairs. Given these explicit representations, it is easy to work out all possible scalar contractions and express the answers in terms of the Mandelstam invariants $\hat{s}$, $\hat{t} = -(\hat{s} - M^2)(1 - \cos\theta)/2$ and $\hat{u} = -(\hat{s} - M^2)(1 + \cos\theta)/2$. The gluon channel amplitudes are functions of these Lorentz invariant dot products.

Using the high energy physics package FEYNCALC [51], we calculated each individual helicity amplitude for $gg \to Q\bar{Q}[^1S_0^{(8)}]g$, $gg \to Q\bar{Q}[^3S_1^{(8)}]g$ and $gg \to Q\bar{Q}[^3P_J^{(8)}]g$ scattering. Parity and crossing symmetry relations between different helicity amplitudes provided valuable checks on our Mathematica code. Since separate helicity amplitudes do not interfere, the total squared amplitude simply equals the sum of the squared helicity amplitudes. The final results are displayed in Appendix A.

The products of short distance color-octet squared amplitudes and long distance NRQCD matrix elements enter into the partonic cross section

$$\frac{d\sigma}{d\hat{t}}(ab \to Q\bar{Q}[^{2S+1}L_J^{(8)}]c \to \psi_Q)_{\rm octet} = \frac{1}{16\pi\hat{s}^2}\overline{\sum}\left|\mathcal{A}(ab \to Q\bar{Q}[^{2S+1}L_J^{(8)}]c)_{\rm short}\right|^2 \langle 0|\mathcal{O}_8^{\psi_Q}(^{2S+1}L_J)|0\rangle. \tag{4.6}$$

After folding in distribution functions $f_{a/A}(x_a)$ and $f_{b/B}(x_b)$ that specify the probabilities of finding partons a and b inside hadrons A and B carrying momentum fractions x_a and x_b, we obtain the hadronic cross section

$$\frac{d^3\sigma}{dy_3 dy_4 dp_\perp}(AB \to \psi_Q X)_{\rm octet} = 2p_\perp \sum_{abc} x_a x_b f_{a/A}(x_a) f_{b/B}(x_b) \frac{d\sigma}{d\hat{t}}(ab \to Q\bar{Q}[^{2S+1}L_J^{(8)}]c \to \psi_Q)_{\rm octet} \tag{4.7}$$

which is a function of the ψ_Q and recoiling jet rapidities, y_3 and y_4, and their common transverse momentum $p_\perp$. With this hadronic distribution in hand, we can determine color-octet contributions to ψ_Q production in any hadronic process. We apply it to the study of charmonia and bottomonia at Fermilab in Sec. 4.3.

4.2 "Including" Altarelli-Parisi evolution

It is instructive to examine the high energy limit of color-octet quarkonia production. As the partonic Mandelstam invariants grow to infinity, the cross section in Eq. (4.6) reduces to

$$\frac{d\sigma}{d\hat{t}}(ab \to \psi_Q c)_{\text{octet}} \stackrel{\hat{s}\to\infty}{\longrightarrow} \frac{d\sigma}{d\hat{t}}(ab \to g^* c) \times \left(\frac{1}{M^2}\right)^2 \times |\mathcal{A}(g^* \to \psi_Q)|^2. \tag{4.8}$$

This asymptotic expression has a simple gluon fragmentation interpretation. The first factor represents the differential cross section for producing a high energy virtual gluon. The second term comes from the square of the gluon's propagator. The last factor equals the square of the amplitude for a gluon to split into a $Q\bar{Q}$ pair times $\langle 0|\mathcal{O}_8[^3S_1]|0\rangle$ and determines the virtual gluon's probability to hadronize into a ψ_Q bound state. The gluon fragmentation picture for heavy quarkonium production is thus precisely recovered in the high energy limit [35].

Gluon fragmentation via the color-octet mechanism represents the dominant source of large $p_\perp$ quarkonia at hadron colliders [17, 52, 53]. The total cross section for ψ_Q production reduces at high energies to the fragmentation form

$$\frac{d^3\sigma}{dy_3 dy_4 dp_\perp}(AB \to \psi_Q X)_{\text{frag}} = \int_0^1 dz \, \frac{d^3\sigma}{dy_3 dy_4 dp_\perp}(AB \to g(\frac{p_\perp}{z})X, \mu) D_{g\to\psi_Q}(z, \mu). \tag{4.9}$$

The gluon fragmentation function evaluated at the factorization scale $\mu = M$ is readily identified from Eq. (4.8) and agrees with the result previously obtained in Ref. [54]:

$$D_{g\to\psi_Q}(z, M) = \frac{\pi\alpha_s(M)\langle 0|\mathcal{O}_8[^3S_1]|0\rangle}{3M^3}\delta(1-z). \tag{4.10}$$

Leading log QCD corrections to this result may be summed up using the Altarelli-Parisi equation

$$\mu\frac{dD_{g\to\psi_Q}}{d\mu}(z, \mu) = \frac{\alpha_s(\mu)}{\pi}\int_z^1 \frac{dy}{y} P_{gg}(y) D_{g\to\psi_Q}(\frac{z}{y}, \mu) \tag{4.11}$$

where

$$P_{gg}(y) = 6\Big[\frac{y}{(1-y)_+} + \frac{1-y}{y} + y(1-y) + \frac{33-2n_f}{36}\delta(1-y)\Big] \qquad (4.12)$$

denotes the gluon splitting function for n_f active quark flavors. At high energies, the fragmentation approximation in Eq. (4.9) incorporates sizable $\mathcal{O}(\log(E^2/M^2))$ renormalization effects, and its intrinsic $\mathcal{O}(M^2/E^2)$ errors are negligible. In contrast, the color-octet formula in Eq. (4.7) does not include any QCD corrections which are small at low $p_\perp$, but it retains full dependence upon all $\mathcal{O}(M^2/E^2)$ terms. These two forms for the ψ_Q differential cross section are thus complementary.

We may exercise our perturbative freedom to supplement the $\mathcal{O}(\alpha_s^3)$ color-octet cross section with the leading logarithms from the gluon fragmentation approach. We implement this choice as follows [31]:

$$d\sigma(AB \to \psi_Q X)_{\text{interp}} = d\sigma(AB \to \psi_Q X)_{\text{octet}} \times \frac{d\sigma(AB \to \psi_Q X)_{\text{frag with QCD running}}}{d\sigma(AB \to \psi_Q X)_{\text{frag without QCD running}}}. \qquad (4.13)$$

The ratio on the right-hand side of this hybrid expression reduces to unity at low energy, whereas the first factor over the denominator approaches unity at high energy. Eq. (4.13) therefore smoothly interpolates between the two asymptotic limits in Eqs. (4.7) and (4.9). We will use this final color-octet formula to study bottomonia and charmonia production at the Tevatron in the following section.

4.3 ψ and Υ production at the Tevatron

After the installation of the vertex detector in CDF, it has been possible to differentiate between prompt quarkonia and quarkonia produced in B decays. This led to the surprising discovery that the theoretical prediction for prompt ψ production, based on the color-singlet model, was far less than the experimental measurement.

These orders of magnitude discrepancies between cross section computations and observations are significantly reduced when gluon and charm color-singlet fragmentation processes are taken into account. The predicted prompt J/ψ rate then quali-

tatively agrees with recent CDF data [37]. In the case of ψ' production, the fragmentation results substantially improve upon earlier differential cross section predictions. But they still underestimate the number of ψ''s observed at the Tevatron by more than a factor of 30. This large discrepancy between theory and experiment indicates that some important production mechanism beyond the simplest $g \to \psi'$ and $c \to \psi'$ fragmentation processes needs to be included. We shall see that the fully consistent $\mathcal{O}(v^7)$ set of color-octet differential cross sections yields substantially improved fits to the data.

4.3.1 Color-octet contribution

We first plot in Fig. 4.4 the ratio

$$R(p_\perp) = \frac{\sum_{J=0}^{2} \frac{d\sigma}{dp_\perp}\left(p\bar{p} \to Q\bar{Q}[^3P_J^{(8)}] + X \to \psi_Q + X\right)}{\frac{d\sigma}{dp_\perp}\left(p\bar{p} \to Q\bar{Q}[^1S_0^{(8)}] + X \to \psi_Q + X\right)} \tag{4.14}$$

where we have temporarily set $\langle \mathcal{O}_8^{\psi_Q}(^3P_0)\rangle = M_Q^2 \langle \mathcal{O}_8^{\psi_Q}(^1S_0)\rangle$ for comparison purposes.[1] The solid curve's nearly constant value $R(p_\perp) \simeq 3$ for $p_\perp \gtrsim 5$ GeV indicates that the shapes of the $c\bar{c}[^1S_0^{(8)}]$ and $c\bar{c}[^3P_J^{(8)}]$ differential cross sections are practically identical in the charmonia sector. As a result, all fits for the NRQCD matrix elements in these color-octet channels become degenerate when performed over the transverse momentum range 5 GeV $\leq p_\perp \leq$ 20 GeV where J/ψ and ψ' differential cross sections have been measured. We consequently can only extract the linear combination $\langle 0|\mathcal{O}_8^{\psi}(^3P_0)|0\rangle/M_c^2 + \langle 0|\mathcal{O}_8^{\psi}(^1S_0)|0\rangle/3$ along with $\langle 0|\mathcal{O}_8^{\psi}(^3S_1)|0\rangle$ from the CDF data. In the bottomonia sector, the shapes of the $b\bar{b}[^1S_0^{(8)}]$ and $b\bar{b}[^3P_J^{(8)}]$ distributions are not exactly the same throughout the $0 \leq p_\perp \leq 15$ GeV interval where Υ data exists. As indicated by the dot-dashed curve in Fig. 4.4, $R(p_\perp)$ varies around 5 over this transverse momentum range. Yet the differences in shape between the

[1] The differential cross sections which enter into results displayed in Fig. 4.4 and all subsequent figures were calculated using the MRSD0 parton distribution functions evaluated at the renormalization scale $\mu = \sqrt{p_\perp^2 + M^2}$.

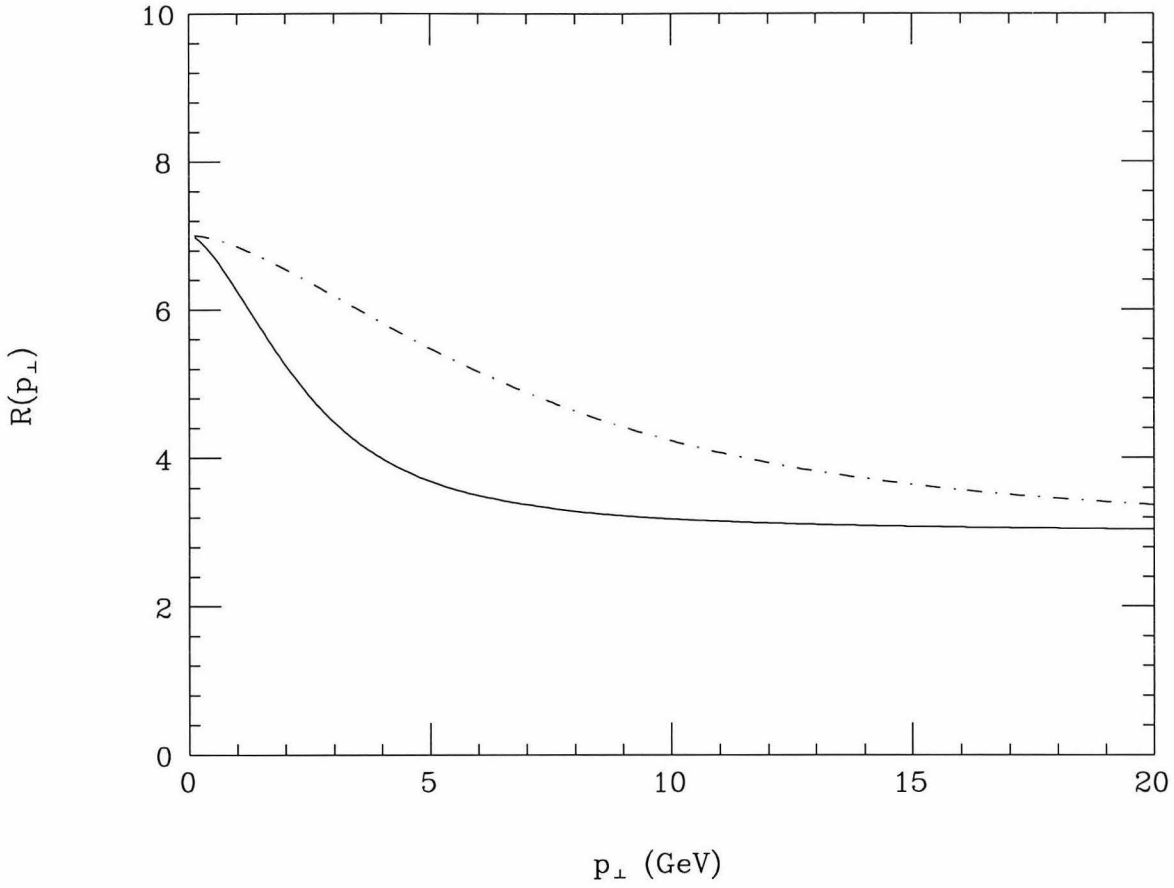

Figure 4.4: Ratio $R(p_\perp)$ of the total $Q\bar{Q}[^3P_J^{(8)}]$ and $Q\bar{Q}[^1S_0^{(8)}]$ contributions to the ψ_Q transverse momentum differential cross section in the limit where the long distance NRQCD matrix element $\langle 0|\mathcal{O}_8^{\psi_Q}(^3P_0)|0\rangle$ equals $M_Q^2\langle 0|\mathcal{O}_8^{\psi_Q}(^1S_0)|0\rangle$. The solid and dotted curves illustrate $R(p_\perp)$ for the charmonia and bottomonia sectors respectively.

$b\bar{b}[^3P_J^{(8)}]$ and $b\bar{b}[^1S_0^{(8)}]$ contributions to the total Υ differential cross section are not sufficiently great so that a full three-parameter color-octet matrix element fit can be reliably performed. So we will simply determine estimates for the linear combination $\langle 0|\mathcal{O}_8^{\Upsilon}(^3P_0)|0\rangle/M_b^2 + \langle 0|\mathcal{O}_8^{\Upsilon}(^1S_0)|0\rangle/5$ along with $\langle 0|\mathcal{O}_8^{\Upsilon}(^3S_1)|0\rangle$.

Our fits to prompt charmonia production at the Tevatron within the pseudorapidity interval $|\eta| \leq 0.6$ are illustrated in Figs. 4.5 and 4.6. All contributions from B meson decay have been removed from the data sets displayed in these figures, and radiative χ_{cJ} decay feeddown to the J/ψ differential cross section has been separated

out as well. The dashed curves depict the direct color-singlet production predictions based upon the charm quark mass value $M_c = 1.48$ GeV and the Buchmüller-Tye charmonium wave functions at the origin tabulated in Ref. [55]. The dot-dashed and dotted curves illustrate the best fits for the $c\bar{c}[^3S_1^{(8)}]$ and combined $c\bar{c}[^3P_J^{(8)}]$ plus $c\bar{c}[^1S_0^{(8)}]$ channels. The solid curves show the sums of the color-singlet and color-octet components and represent the total predicted differential cross sections.

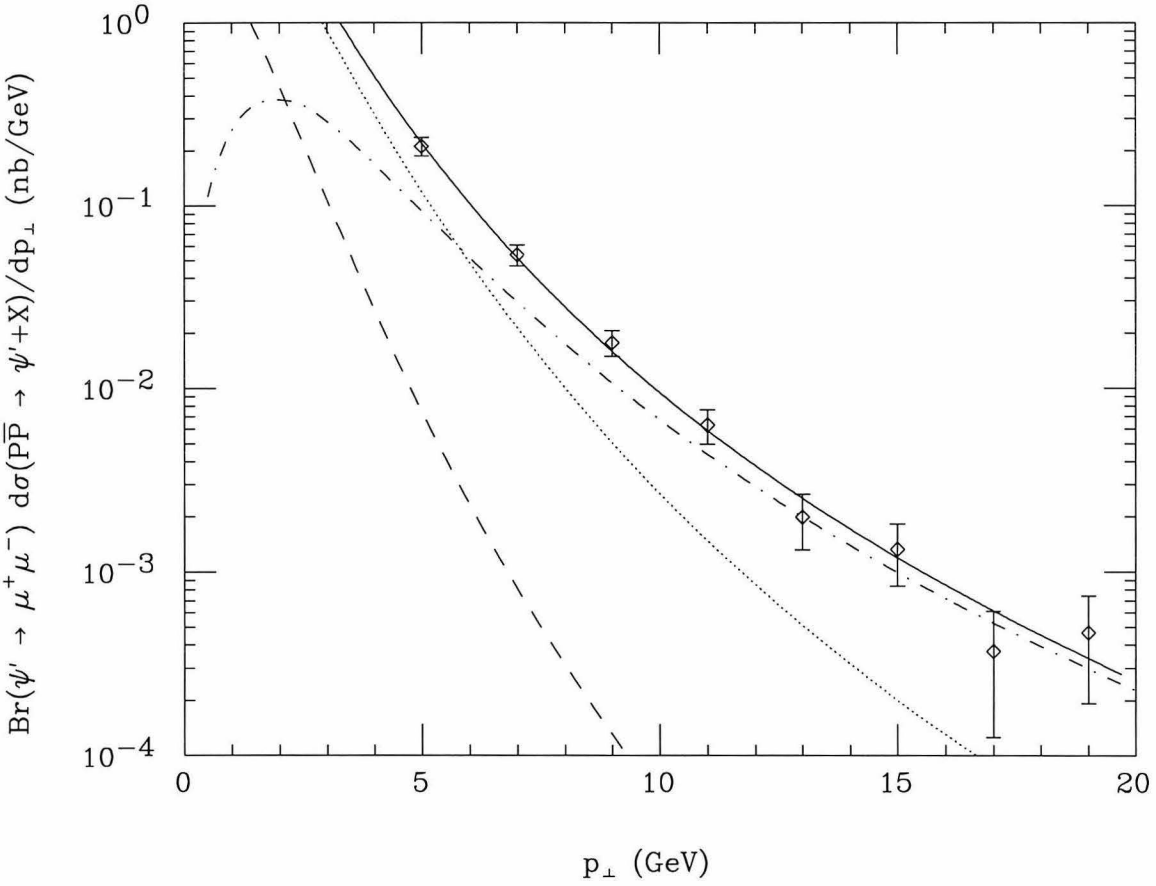

Figure 4.5: Theoretical transverse momentum differential cross section for prompt ψ' production at the Tevatron in the pseudorapidity interval $|\eta| \leq 0.6$ compared against preliminary CDF data. The dashed curve depicts the direct color-singlet contribution to ψ' production. The dot-dashed curve illustrates the $c\bar{c}[^3S_1^{(8)}]$ cross section, and the dotted curve denotes the combined $c\bar{c}[^3P_J^{(8)}]$ and $c\bar{c}[^1S_0^{(8)}]$ distributions. The solid curve equals the sum of the color-singlet and color-octet contributions and represents the total theoretical prediction for the ψ' differential cross section. All curves are multiplied by the muon branching fraction $\mathrm{Br}(\psi' \to \mu^+\mu^-)$.

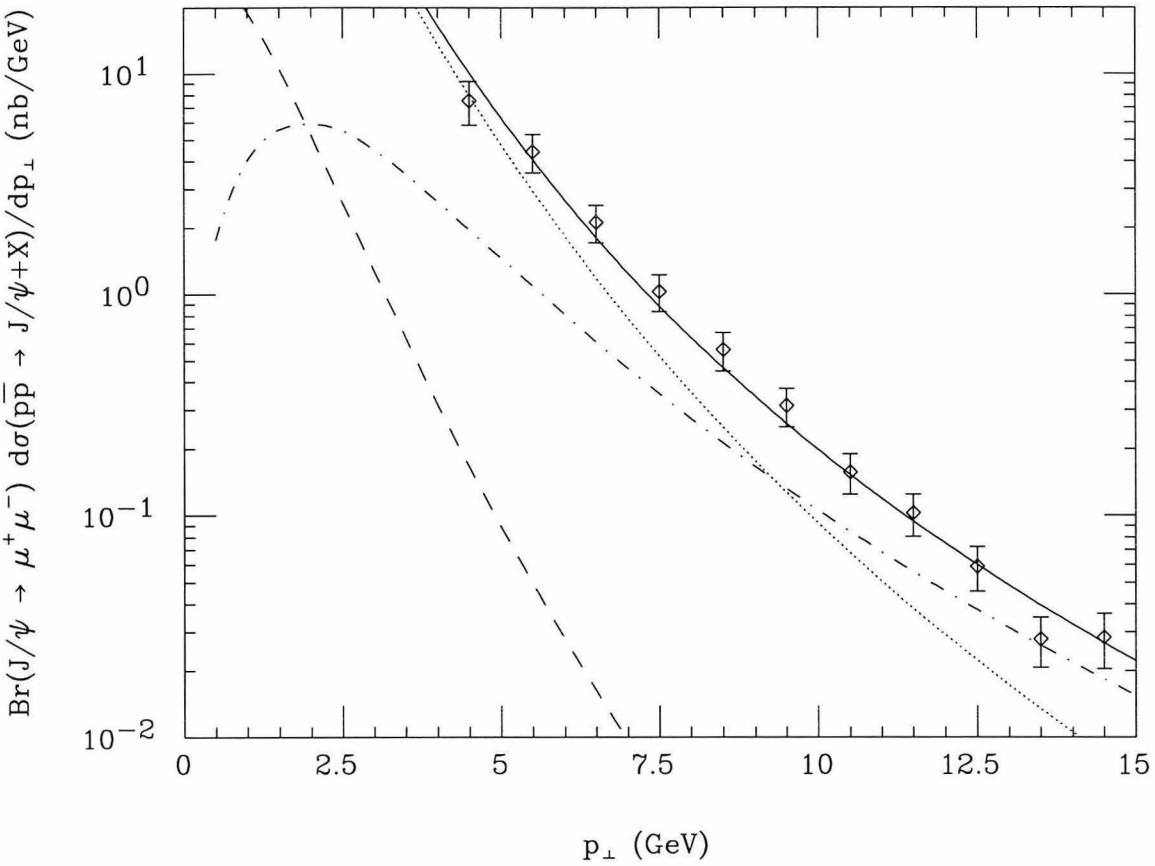

Figure 4.6: Theoretical transverse momentum differential cross section for prompt J/ψ production at the Tevatron in the pseudorapidity interval $|\eta| \leq 0.6$ compared against preliminary CDF data. The curves in this figure are labeled in the same way as those in Fig. 4.5. All curves are multiplied by the muon branching fraction $\mathrm{Br}(J/\psi \to \mu^+\mu^-)$.

Following the interpolation procedure described in 4.2, we have included leading log corrections into the $c\bar{c}[^3S_1^{(8)}]$ differential cross sections so that they approach Altarelli-Parisi improved gluon fragmentation distributions for $p_\perp \gg M_c$. In the large transverse momentum limit, gluon fragmentation represents the dominant source of prompt charmonia [35, 17, 52, 56, 57, 54]. This asymptotic behavior can be seen in the dotdashed $c\bar{c}[^3S_1^{(8)}]$ curves of Figs. 4.5 and 4.6. But throughout the $0 \leq p_\perp \leq 20$ GeV region, they are not overwhelmingly larger than the combined $c\bar{c}[^3P_J^{(8)}]$ and $c\bar{c}[^1S_0^{(8)}]$ components whose contributions to prompt charmonia production are sizable. Inclusion of the latter color-octet channels into the total differential cross sections yields

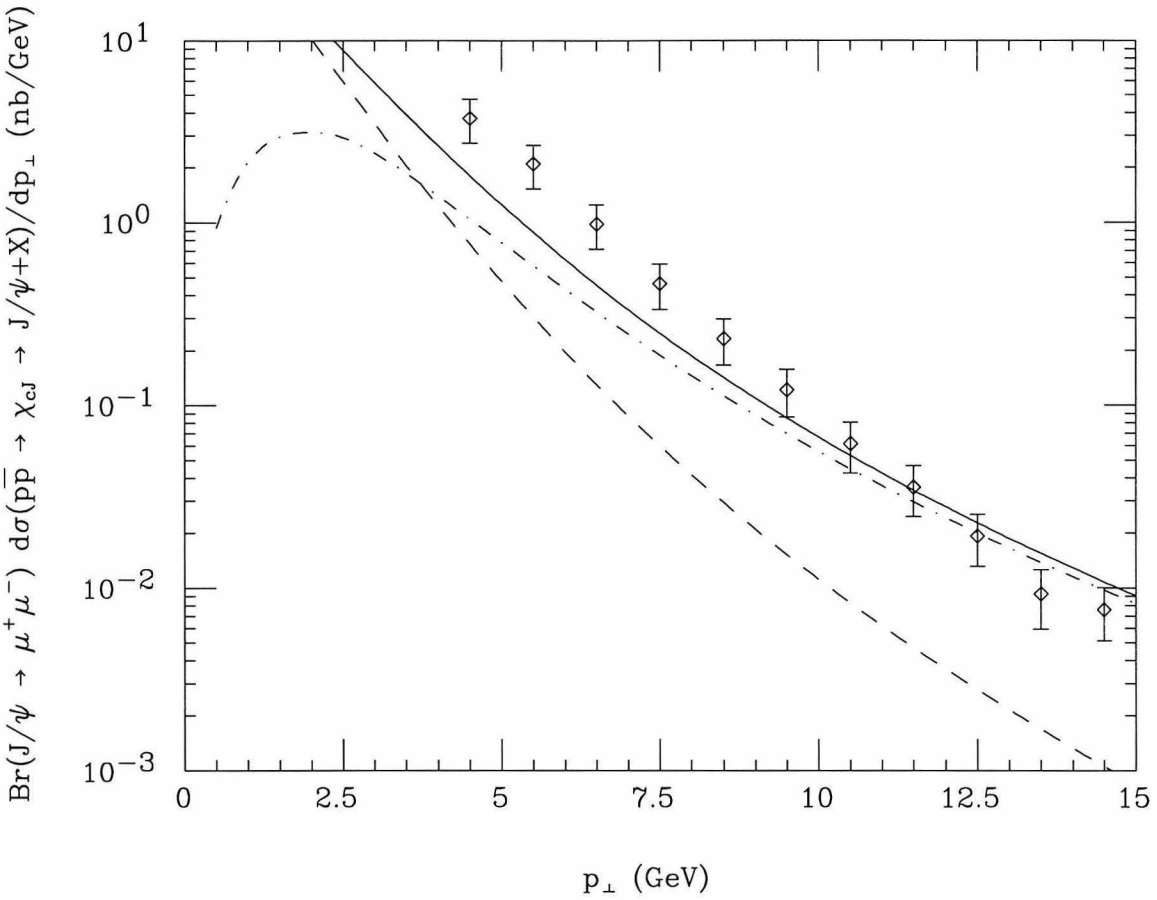

Figure 4.7: Theoretical transverse momentum differential cross section for J/ψ production at the Tevatron in the pseudorapidity interval $|\eta| \leq 0.6$ resulting from radiative χ_{cJ} decay compared against preliminary CDF data. The dashed curve depicts the color-singlet contribution, the dot-dashed curve illustrates the $c\bar{c}[^3S_1^{(8)}]$ cross section and the solid curve represents their sum. All curves are multiplied by the muon branching fraction $\mathrm{Br}(J/\psi \to \mu^+\mu^-)$.

theoretical ψ' and J/ψ distributions which fit the data quite well. Their respective $\chi^2/\mathrm{NDOF} = 0.5$ and $\chi^2/\mathrm{NDOF} = 0.9$ figures-of-merit are nice and small.

In Fig. 4.7, we plot the transverse momentum distribution of J/ψ mesons which result from radiative χ_{cJ} decay. The dashed curve in the figure shows the color-singlet χ_{cJ} differential cross section multiplied by $\mathrm{Br}(\chi_{cJ} \to J/\psi+\gamma)$ and summed over $J = 0$, 1 and 2. The dot-dashed curve illustrates the $c\bar{c}[^3S_1^{(8)}]$ channel contribution. The solid curve corresponds to their sum and represents the total $\mathcal{O}(v^5)$ cross section prediction. As indicated by its poor $\chi^2/\mathrm{NDOF} = 2.3$ value, this solid line does not fit the data

well. We believe that a better match could be achieved if subleading color-octet contributions were included. The first subdominant corrections enter at $\mathcal{O}(v^9)$ in the NRQCD velocity expansion from the long distance evolution of $Q\bar{Q}[^3P_J^{(8)}]$, $Q\bar{Q}[^3D_J^{(8)}]$ and $Q\bar{Q}[^1P_1^{(8)}]$ pairs into χ_{QJ} bound states. Since short distance production cross sections for the latter two pairs have not been yet calculated, we cannot include into Fig. 4.7 subleading contributions from the first pair which we have computed.

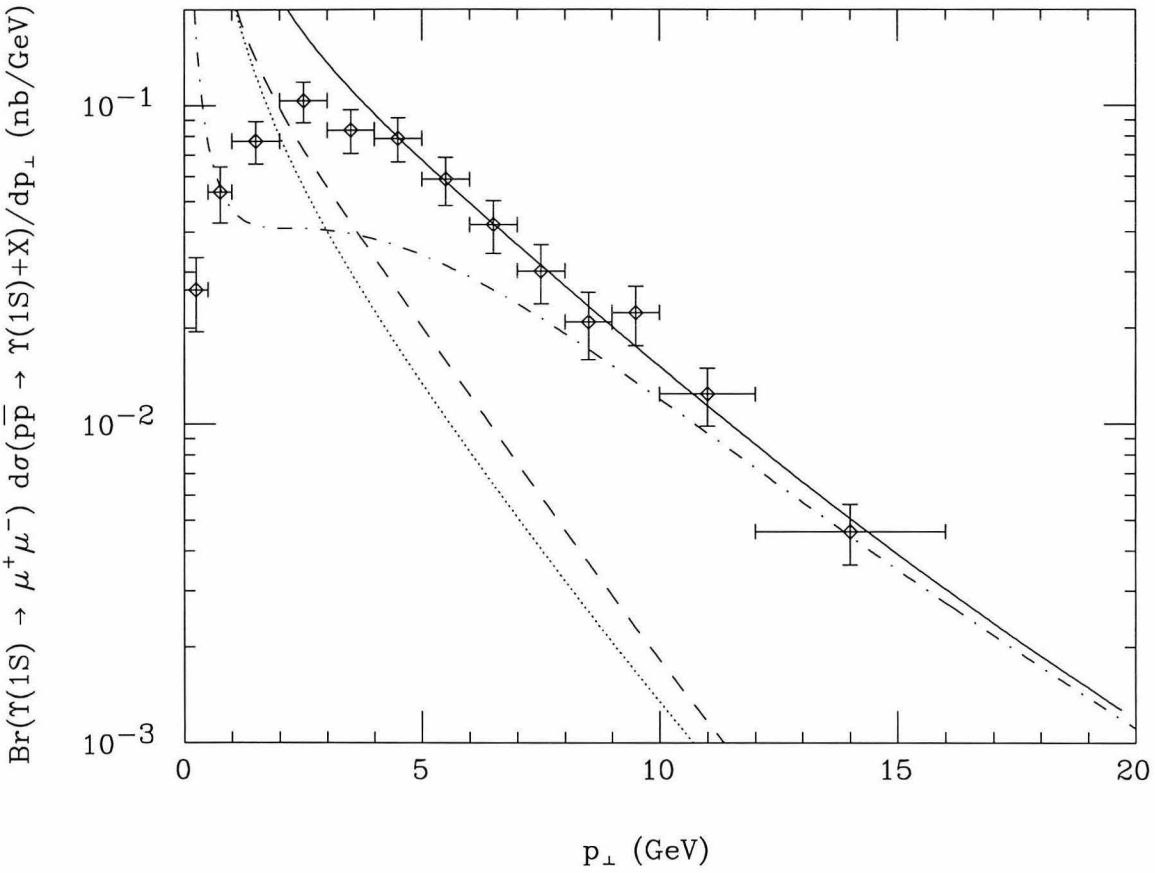

Figure 4.8: Theoretical transverse momentum differential cross section for $\Upsilon(1S)$ production at the Tevatron in the rapidity interval $|y| \leq 0.4$ compared against preliminary CDF data. The dashed curve depicts the color-singlet contribution which includes direct $\Upsilon(1S)$ production as well as radiative feeddown from $\chi_{bJ}(1P)$ and $\chi_{bJ}(2P)$ states. The dot-dashed curve illustrates the $b\bar{b}[^3S_1^{(8)}]$ cross section, and the dotted curve denotes the combined $b\bar{b}[^3P_J^{(8)}]$ and $b\bar{b}[^1S_0^{(8)}]$ distributions. The solid curve equals the sum of the color-singlet and color-octet contributions and represents the total theoretical prediction for the $\Upsilon(1S)$ differential cross section. All curves are multiplied by the muon branching fraction $\mathrm{Br}(\Upsilon(1S) \to \mu^+\mu^-)$.

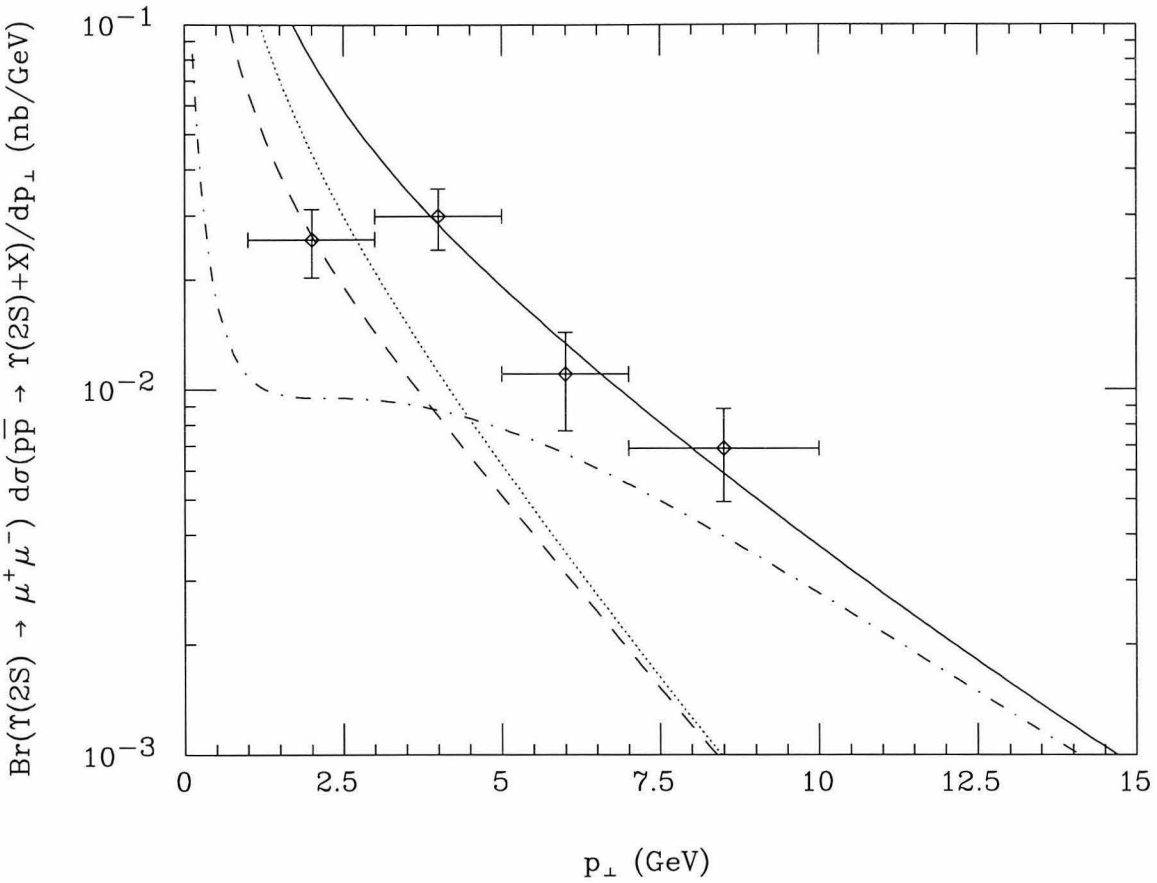

Figure 4.9: Theoretical transverse momentum differential cross section for $\Upsilon(2S)$ production at the Tevatron in the rapidity interval $|y| \leq 0.4$ compared against preliminary CDF data. The curves in this figure are labeled the same as those in Fig. 4.8. The dashed color-singlet cross section includes $\Upsilon(2S)$ production and radiative feeddown from $\chi_{bJ}(2P)$. All curves are multiplied by the muon branching fraction $\mathrm{Br}(\Upsilon(2S) \to \mu^+\mu^-)$.

We turn now to the bottomonium sector and consider Υ production at the Tevatron within the rapidity interval $|y| \leq 0.4$. Our new fits to CDF $\Upsilon(1S)$ and $\Upsilon(2S)$ data are displayed in Figs. 4.8 and 4.9. No separation between prompt and delayed Υ sources has been experimentally performed. The dashed curves in the figures therefore include both direct Υ production and radiative feeddown from χ_{bJ} states. These color-singlet distributions are based upon the bottom quark mass value $M_b = 4.88$ GeV and the Buchmüller-Tye bottomonia wavefunctions at the origin tabulated in Ref [55]. The dot-dashed and dotted curves illustrate the $b\bar{b}[^3S_1^{(8)}]$ and combined $b\bar{b}[^3P_J^{(8)}]$ plus

$b\bar{b}[^1S_0^{(8)}]$ fits. The solid curves equal the sums of the color-singlet and color-octet contributions and represent the total Υ differential cross sections. At very small $p_\perp$, the color-singlet and color-octet cross sections are corrupted by collinear divergences which should be factored into incident parton distribution functions and the intrinsic motion of incident partons inside colliding hadrons becomes important. Soft gluon effects also need to be resummed before the cross section turnover, which is evident in Fig. 4.8, can be described correctly. Since we have not incorporated these effects, our cross section predictions are not trustworthy at low $p_\perp$. We therefore exclude points in Figs. 4.8 and 4.9 with $p_\perp \leq 3.5$ GeV from our fits. We then find $\chi^2/\mathrm{NDOF} = 0.3$ and $\chi^2/\mathrm{NDOF} = 0.9$ for the remaining points in these figures.

4.4 Extraction of NRQCD matrix elements

We have seen that heavy quarkonia production involves short and long distance physics. The high energy creation of color-singlet and color-octet $Q\bar{Q}$ pairs is perturbatively computable within the NRQCD effective theory. The subsequent low energy hadronization of these pairs into physical bound states is described in terms of nonrenormalizable operator matrix elements. NRQCD scaling rules determine the relative importance of different long distance matrix elements and yield relations among them. We will use these rules to check the consistency of the fitted ψ and Υ amplitude values which we obtained in the preceding section.

We first recall the relations (2.31),

$$\langle 0|\mathcal{O}_1^{\psi_Q}(^3S_1)|0\rangle = \frac{N_c}{2\pi}|R(0)|^2 = \mathcal{O}(M_Q^3 v_Q^3), \tag{4.15}$$

$$\langle 0|\mathcal{O}_1^{\chi_{QJ}}(^3P_J)|0\rangle = \frac{3N_c}{2\pi}(2J+1)|R'(0)|^2 = \mathcal{O}(M_Q^5 v_Q^5), \tag{4.16}$$

between quarkonia radial wavefunctions at the origin and matrix elements of certain color-singlet four-quark operators in the NRQCD Lagrangian [4]. The details of these operators' definitions are discussed in Sec. 2.1.4, but they are not important to us here. Instead, we are only interested in their scaling dependence upon the heavy quark mass M_Q and velocity v_Q.

Using the Buchmüller-Tye wavefunction information tabulated in Ref. [55], we list the numerical values of color-singlet matrix elements that are relevant for Υ and ψ production in Table 4.1. The entries in this table are consistent with the NRQCD power counting rules. In the $v_Q \to 0$ limit, the long distance quarkonia matrix elements would be independent of the radial quantum number n. In actuality, the n dependence of the $b\bar{b}$ sector entries is generally smaller than that of the $c\bar{c}$ values. This trend simply indicates that the NRQCD velocity expansion works better for bottomonia with $v_b^2 \simeq 0.08$ than for charmonia with $v_c^2 \simeq 0.23$.

Color-Singlet Matrix Element	Numerical Value	NRQCD Scaling Order
$\langle 0\|\mathcal{O}_1^{J/\psi}(^3S_1)\|0\rangle$	1.2 GeV^3	$M_c^3 v_c^3$
$\langle 0\|\mathcal{O}_1^{\chi_{c1}}(^3P_1)\|0\rangle$	3.2×10^{-1} GeV^5	$M_c^5 v_c^5$
$\langle 0\|\mathcal{O}_1^{\psi'}(^3S_1)\|0\rangle$	7.6×10^{-1} GeV^3	$M_c^3 v_c^3$
$\langle 0\|\mathcal{O}_1^{\Upsilon(1S)}(^3S_1)\|0\rangle$	9.3 GeV^3	$M_b^3 v_b^3$
$\langle 0\|\mathcal{O}_1^{\chi_{b1}(1P)}(^3P_1)\|0\rangle$	6.1 GeV^5	$M_b^5 v_b^5$
$\langle 0\|\mathcal{O}_1^{\Upsilon(2S)}(^3S_1)\|0\rangle$	4.6 GeV^3	$M_b^3 v_b^3$
$\langle 0\|\mathcal{O}_1^{\chi_{b1}(2P)}(^3P_1)\|0\rangle$	7.1 GeV^5	$M_b^5 v_b^5$
$\langle 0\|\mathcal{O}_1^{\Upsilon(3S)}(^3S_1)\|0\rangle$	3.5 GeV^3	$M_b^3 v_b^3$

Table 4.1: Color-singlet matrix elements values obtained from Buchmüller-Tye wavefunctions obtained from Ref. [55].

We list in Tables 4.2 and 4.3 the numerical values for color-octet matrix elements which we extracted from the data along with their scaling dependence upon the heavy quark mass M_Q and velocity v_Q. The values for all the charmonia matrix elements were derived directly from the CDF J/ψ and ψ' data. On the other hand, in-

sufficient experimental information exists to independently extract $\langle 0|O_8^{\Upsilon(nS)}(^3S_1)|0\rangle$ and $\langle 0|O_8^{\chi_{b1}(nP)}(^3S_1)|0\rangle$ in the bottomonia sector. We therefore determined the latter from the Υ data after having scaled up the former from the corresponding ψ color-octet matrix elements using NRQCD power counting rules. The remaining $\langle 0|O_8^{\Upsilon(nS)}(^3P_0)|0\rangle/M_b^2 + \langle 0|O_8^{\Upsilon(nS)}(^1S_0)|0\rangle/5$ linear combinations were obtained directly from the bottomonia cross section data.

Color-Octet Matrix Element	Numerical Value (GeV^3)	NRQCD Scaling Order
$\langle 0\|\mathcal{O}_8^{J/\psi}(^3S_1)\|0\rangle$	$(6.6 \pm 2.1) \times 10^{-3}$	$M_c^3 v_c^7$
$\langle 0\|\mathcal{O}_8^{\chi_{c1}}(^3P_1)\|0\rangle$	$(9.8 \pm 1.3) \times 10^{-3}$	$M_c^5 v_c^5$
$\langle 0\|\mathcal{O}_8^{\psi'}(^3S_1)\|0\rangle$	$(4.6 \pm 1.0) \times 10^{-3}$	$M_c^3 v_c^7$
$\langle 0\|\mathcal{O}_8^{\Upsilon(1S)}(^3S_1)\|0\rangle$	$(5.9 \pm 1.9) \times 10^{-3}$	$M_b^3 v_b^7$
$\langle 0\|\mathcal{O}_8^{\chi_{b1}(1P)}(^3P_1)\|0\rangle$	$(4.2 \pm 1.3) \times 10^{-1}$	$M_b^5 v_b^5$
$\langle 0\|\mathcal{O}_8^{\Upsilon(2S)}(^3S_1)\|0\rangle$	$(4.1 \pm 0.9) \times 10^{-3}$	$M_b^3 v_b^7$
$\langle 0\|\mathcal{O}_8^{\chi_{b1}(2P)}(^3P_1)\|0\rangle$	$(3.2 \pm 1.9) \times 10^{-1}$	$M_b^5 v_b^5$

Table 4.2: Color-octet matrix elements values extracted from CDF data [28]. The errors are purely statistical.

The error bars listed in Tables 4.2 and 4.3 are statistical and do not reflect systematic uncertainties in heavy quark masses, color-singlet radial wavefunctions, parton distribution functions and next-to-leading order corrections. The magnitudes of all these different sources of uncertainty can be estimated. For example, the different charm and bottom quark mass values which enter into the power law, logarithmic, Coulomb plus linear and QCD motivated Buchmüller-Tye potentials tabulated in Ref. [55] span the ranges 1.48 GeV $\leq M_c \leq$ 1.84 GeV and 4.88 GeV $\leq m_b \leq$ 5.18 GeV. These intervals may be regarded as setting reasonable bounds for the

Color-Octet Matrix Element Linear Combination	Numerical Value (GeV^3)	NRQCD Scaling Order
$\frac{\langle \mathcal{O}_8^{J/\psi}(^3P_0)\|0\rangle}{M_c^2} + \frac{\mathcal{O}_8^{J/\psi}(^1S_0)\|0\rangle}{3}$	$(2.2 \pm 0.5) \times 10^{-2}$	$M_c^3 v_c^7$
$\frac{\langle \mathcal{O}_8^{\psi'}(^3P_0)\|0\rangle}{M_c^2} + \frac{\mathcal{O}_8^{\psi'}(^1S_0)\|0\rangle}{3}$	$(5.9 \pm 1.9) \times 10^{-3}$	$M_c^3 v_c^7$
$\frac{\langle \mathcal{O}_8^{\Upsilon(1S)}(^3P_0)\|0\rangle}{M_b^2} + \frac{\mathcal{O}_8^{\Upsilon(1S)}(^1S_0)\|0\rangle}{5}$	$(7.9 \pm 10.0) \times 10^{-2}$	$M_b^3 v_b^7$
$\frac{\langle \mathcal{O}_8^{\Upsilon(2S)}(^3P_0)\|0\rangle}{M_b^2} + \frac{\mathcal{O}_8^{\Upsilon(2S)}(^1S_0)\|0\rangle}{5}$	$(9.1 \pm 7.2) \times 10^{-2}$	$M_b^3 v_b^7$

Table 4.3: Linear combination of color-octet matrix elements values extracted from CDF data [28]. The errors are purely statistical.

heavy quark mass parameters. The spread in values for radial wavefunctions at the origin calculated in these four different potential models similarly provides an approximate indication of color-singlet matrix element uncertainties. Systematic errors which arise from parton distribution functions and higher order QCD corrections can also be assessed by performing several fits with different choices of distribution functions and renormalization scale [58]. We have not attempted to carry out a detailed analysis of the combined impact of all these systematic uncertainties. Our color-octet matrix element values therefore represent reasonable estimates rather than precise predictions.

Observe that the NRQCD counting rules are more faithfully followed by some matrix elements than others. For instance, the magnitudes of the matrix elements $\langle 0|\mathcal{O}_8^{J/\psi}(^3S_1)|0\rangle$, $\langle 0|\mathcal{O}_8^{\psi'}(^3S_1)|0\rangle$ and $\langle 0|\mathcal{O}_8^{\psi'}(^3P_0)|0\rangle/M_c^2 + \langle 0|\mathcal{O}_8^{\psi'}(^1S_0)|0\rangle/3$ are all mutually consistent with their common scaling rule. On the other hand, $\langle 0|\mathcal{O}_8^{\chi_{c1}}(^3S_1)|0\rangle$ is somewhat low while $\langle 0|\mathcal{O}_8^{J/\psi}(^3P_0)|0\rangle/M_c^2 + \langle 0|\mathcal{O}_8^{\psi'}(^1S_0)|0\rangle/3$ is somewhat high. Since $v_c^2 \simeq 0.23$ is not very small, none of the charmonia NRQCD order-of-magnitude es-

timates should be overly interpreted. We view the general consistency of the fitted matrix elements with the power counting rules as an encouraging indication that the color-octet quarkonia production picture is sound.

4.5 Tests of NRQCD

The best test of NRQCD would be to extract the NRQCD matrix elements from one experimental situation and use them to make predictions for a different experiment, or to compare the extracted matrix elements from different experiments. So far the extractions are not accurate enough to make a meaningful comparison [28, 58, 59, 60]. Furthermore, it is not clear whether it is even possible to use the matrix elements for different reactions [61].

Another potential test is the polarization of the quarkonia state produced in some collision. Like Heavy Quark Effective Theory, NRQCD incorporates an approximate Heavy Quark Spin Symmetry, which can be used to calculate the polarization. At large transverse momenta, quarkonia are primarily produced by gluon fragmentation [35, 17, 52, 56, 57, 54]. The gluon is nearly real and transverse in the high $p_\perp$ limit, and the resulting $Q\bar{Q}[^3S_1^{(8)}]$ pair inherits this spin alignment. The long distance hadronization into a colorless ψ preserves all angular momentum information, due to the NRQCD approximate spin symmetry. Thus, ψ mesons produced at large $p_\perp$ are 100% transversely aligned [62]. Higher order α_s corrections to the polarization of ψ from gluon fragmentation have been calculated, and occur at the few percent level [63].

Gluon fragmentation is, however, only valid in the $p_\perp \gg M_Q$ limit. At low transverse momentum, large numbers of ψ's are produced via color-octet states with $L = S = 0$ and $L = S = 1$ [31, 28]. Corrections to the fragmentation limit are not constrained to preserve the polarization of the ψ. Therefore, to use quarkonia polarization as a test of the color-octet mechanism, we need to investigate the spin alignment due to these states. In this section, we will only consider the polarization of ψ' mesons. A similar analysis for other charmonia and bottomonia states is possible,

but these mesons are complicated by feeddown from higher level states.

The methods used in calculating the amplitudes are similar to those described in Sec. 2.2, and the discussion will not be repeated here. The only difference is that we projected the amplitude onto states of definite L_z and S_z, squared, and then summed over L_z, leaving the S_z polarization arbitrary. The polarization vector $\epsilon(\lambda)$ of the quarkonium state then explicitly enters the differential cross section, Eq. (4.6), as [58]

$$\frac{d\hat{\sigma}_{ab}^{(\lambda)}[n]}{d\hat{t}} = A_{ab}[n] + B_{ab}[n](\epsilon(\lambda)\cdot p_1)^2 + C_{ab}[n](\epsilon(\lambda)\cdot p_2)^2 + D_{ab}[n](\epsilon(\lambda)\cdot p_1)(\epsilon(\lambda)\cdot p_2), \tag{4.17}$$

where p_1 and p_2 are the momenta of the initial state partons a and b. The coefficients $A,\ldots,D$ are shown in Appendix D.

The ratio of longitudinal differential cross section to the unpolarized differential cross section,

$$\xi = \frac{\sigma_L}{\sigma_T + \sigma_L}, \tag{4.18}$$

can be measured in $\psi' \to \ell^+\ell^-$ decay. The leptons are distributed in angle according to

$$\frac{d\Gamma(\psi' \to \ell^+\ell^-)}{d\cos\theta} \propto 1 + \alpha\cos^2\theta, \tag{4.19}$$

where

$$\alpha = \frac{1-3\xi}{1+\xi}, \tag{4.20}$$

and θ denotes the angle between the lepton momentum in the ψ' rest frame and the ψ' momentum in the lab frame. In Fig. 4.10, we plot α for prompt ψ' production at the Tevatron.[2] Since there is only a value for the linear combination of $\langle 0|\mathcal{O}_8^{\psi'}(^1S_0)|0\rangle$ and $\langle 0|\mathcal{O}_8^{\psi'}(^3P_0)|0\rangle$, we cannot give a definite prediction for α. Instead, the solid curve represents α when $\langle 0|\mathcal{O}_8^{\psi'}(^3P_0)|0\rangle = 0$. The dashed curve illustrates α when the contribution from $\langle 0|\mathcal{O}_8^{\psi'}(^1S_0)|0\rangle$ is set to zero. The shaded region illustrates the effect of the uncertainties in the matrix elements in Table 4.3.

[2] In this section, MRSD0 parton distribution functions evaluated at the renormalization scale $\mu = \sqrt{p_\perp^2 + 4M_c^2}$ were used, with $M_c = 1.48$ GeV. A pseudorapidity cut of $|\eta| \le 0.6$ was imposed.

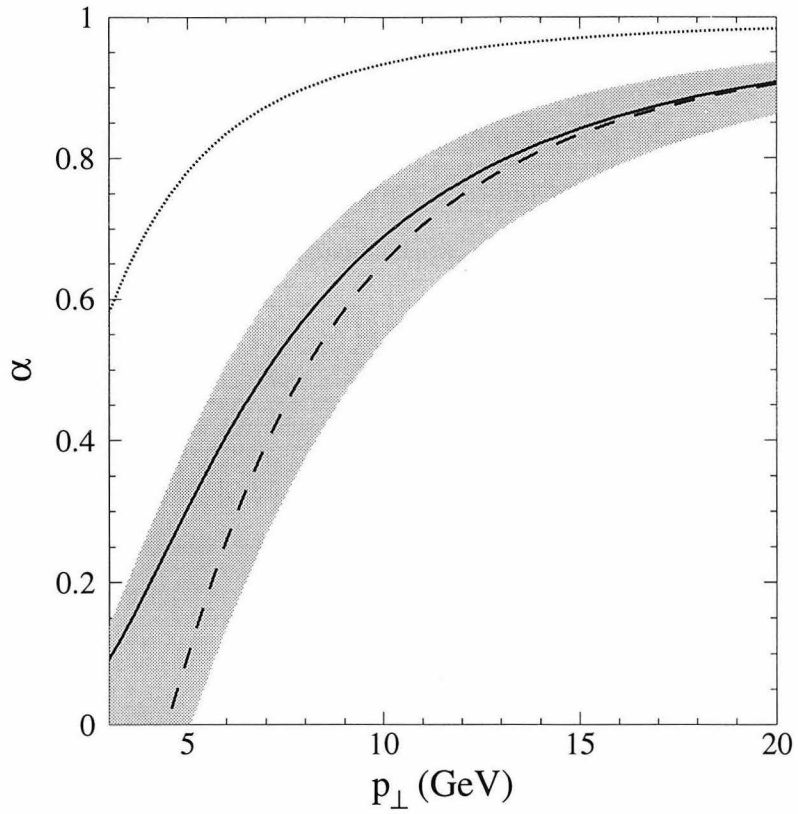

Figure 4.10: Coefficient α which governs the lepton angular distribution in $\psi' \to \ell^+\ell^-$ decay plotted as a function of $p_\perp$. The solid and dashed curves illustrate α for ψ' production at the Tevatron when $\langle 0|\mathcal{O}_8^{\psi'}(^3P_0)|0\rangle$ and $\langle 0|\mathcal{O}_8^{\psi'}(^1S_0)|0\rangle$ respectively vanish. The shaded region shows the effect of the uncertainty in the extraction of the matrix elements. The dotted line corresponds to the lowest order, color-singlet production.

The angular distribution approaches the transverse form $1 + \cos^2\theta$ at high $p_\perp$ as predicted by gluon fragmentation computations [62]. At low transverse momentum, the ψ' is essentially unpolarized due to $L = S = 0$ and $L = S = 1$ color-octet states. Since the two curves are similar in shape, the true value for the angular coefficient should be close to the curves shown. The effect of uncertainties in the matrix elements and higher order corrections can be qualitatively described by slight displacements of the curves in Fig. 4.10, without changing the asymptotic behaviors. Higher order α_s corrections, however, can change the asymptotic high $p_\perp$ behavior, but it should be a small effect [63].

Also plotted in Fig. 4.10 is the polarization due to the lowest order, color-singlet

production, $gg \rightarrow c\bar{c}[^3S_1^{(1)}]g$. As can be seen, the qualitative shape of the color-singlet curve is similar to the color-octet curves. While higher order color-singlet corrections will modify this shape, it is clear that by just observing the qualitative shape presented in Fig. 4.10 of the prompt ψ' polarization at the Tevatron will not be a clear signature for color-octet production.

Chapter 5 Conclusion

Nonrelativistic Quantum Chromodynamics has been proposed as the proper way of calculating quarkonia production and decay. We have reviewed the implications of this effective field theory in this thesis. NRQCD makes a variety of predictions which are relevant in many experimental situations. We have examined color-octet production of heavy quarkonia at hadron colliders. Color-octet diagrams arise at the same order in perturbative QCD as their color-singlet analogues and reduce to the dominant set of gluon fragmentation graphs in the high energy limit. They must therefore be included in bottomonia and charmonia production computations.

Even though the color-octet mechanism is very important at the Tevatron, it is not the whole picture. Color-singlet production is often the most important contribution to quarkonia production. In particular, for quarkonia production at an e^+e^- collider there is no kinematic reason for the color-singlet channel to be suppressed relative to the color-octet channel for most of phase space. As such, as an example we calculated the color-singlet production of prompt ψ's at CLEO in closed form.

As we have seen, color-octet contributions to Υ and ψ differential cross sections eliminate large disparities between earlier predictions and recent measurements. The long distance matrix element values needed to bring theory into line with experiment are consistent with NRQCD scaling rules. The ψ is predicted to be 100% polarized in the fragmentation limit. Inclusion of the full $\mathcal{O}(v^7)$ calculation reduces the predicted polarization in the low $p_\perp$ region. These measurements are currently being pursued, and it will be interesting to see whether they are consistent with the predictions of NRQCD.

Many of the results in this paper can be applied to a range of other interesting problems in quarkonium phenomenology. For example, the velocity scaling rules for NRQCD are not obvious in all calculations. Deriving them in a systematic, gauge-independent way would be very interesting. It may be possible to relate the

NRQCD matrix elements extracted from different experimental settings, with perhaps some model dependence. If so, it would be an interesting test of the formalism. At low transverse momentum, the quarkonia distributions should vanish rather than diverge. In order to compute the cross section turnover, it will be necessary to factorize collinear singularities in both the color-singlet and color-octet channels into incident parton distribution functions. This factorization also needs to be performed before differential quarkonia distributions can be integrated. The NRQCD matrix elements can also be applied to the study of quarkonia production at lepton colliders. Gluon fragmentation has been shown to represent the largest source of prompt ψ and Υ vector mesons at LEP [64, 53]. Its incorporation into $Z \to J/\psi$, $Z \to \psi'$ and $Z \to \Upsilon$ branching fractions reduces sizable differences between predictions based upon color-singlet heavy quark fragmentation and recent LEP measurements. The color-octet mechanism may eliminate disagreements between theory and experiment in fixed target settings. Finally, all the results in this thesis can be applied to the study of quarkonia production at the next generation of hadron colliders. We look forward to further surprises in quarkonium physics coming from machines like the LHC well into the next century.

Appendix A Squared amplitudes for unpolarized quarkonia production

We list below short distance squared amplitudes for $2 \to 1$ and $2 \to 2$ scattering processes which mediate color-octet quarkonia production. These expressions are averaged over initial and summed over final spins and colors of the appropriate particles. The total squared amplitudes for creating specific quarkonia states are obtained by multiplying these process-independent short distance expressions with appropriate long distance NRQCD matrix elements [28].

$q\bar{q} \to Q\bar{Q}[^{2S+1}L_J^{(8)}]$ channel:

$$\overline{\sum}|\mathcal{A}(q\bar{q} \to Q\bar{Q}[^3S_1^{(8)}])|^2 = \frac{(4\pi\alpha_s)^2}{27M} \tag{A.1}$$

$gg \to Q\bar{Q}[^{2S+1}L_J^{(8)}]$ channel:

$$\overline{\sum}|\mathcal{A}(gg \to Q\bar{Q}[^1S_0^{(8)}])|^2 = \frac{5(4\pi\alpha_s)^2}{192M} \tag{A.2a}$$

$$\overline{\sum}|\mathcal{A}(gg \to Q\bar{Q}[^3P_0^{(8)}])|^2 = \frac{5(4\pi\alpha_s)^2}{16M^3} \tag{A.2b}$$

$$\overline{\sum}|\mathcal{A}(gg \to Q\bar{Q}[^3P_1^{(8)}])|^2 = 0 \tag{A.2c}$$

$$\overline{\sum}|\mathcal{A}(gg \to Q\bar{Q}[^3P_2^{(8)}])|^2 = \frac{(4\pi\alpha_s)^2}{12M^3} \tag{A.2d}$$

$q\bar{q} \to Q\bar{Q}[^{2S+1}L_J^{(8)}]g$ channel:

$$\overline{\sum}|\mathcal{A}(q\bar{q} \to Q\bar{Q}[^1S_0^{(8)}]g)|^2 = \frac{5(4\pi\alpha_s)^3}{27M^3}\frac{\hat{t}^2+\hat{u}^2}{\hat{s}(\hat{s}-M^2)^2} \tag{A.3a}$$

$$\overline{\sum}|\mathcal{A}(q\bar{q} \to Q\bar{Q}[^3S_1^{(8)}]g)|^2 = \frac{2(4\pi\alpha_s)^3}{81M^3}\frac{\hat{t}^2+\hat{u}^2+2M^2\hat{s}}{\hat{t}\hat{u}(\hat{s}-M^2)^2}[4(\hat{t}^2+\hat{u}^2)-\hat{t}\hat{u}] \tag{A.3b}$$

$$\overline{\sum}|\mathcal{A}(q\bar{q} \to Q\bar{Q}[^3P_0^{(8)}]g)|^2 = \frac{20(4\pi\alpha_s)^3}{81M^3}\frac{(\hat{s}-3M^2)^2(\hat{t}^2+\hat{u}^2)}{\hat{s}(\hat{s}-M^2)^4} \tag{A.3c}$$

$$\overline{\sum}|\mathcal{A}(q\bar{q} \to Q\bar{Q}[^3P_1^{(8)}]g)|^2 = \frac{40(4\pi\alpha_s)^3}{81M^3}\frac{\hat{s}(\hat{t}^2+\hat{u}^2)+4M^2\hat{t}\hat{u}}{(\hat{s}-M^2)^4} \tag{A.3d}$$

$$\overline{\sum}|\mathcal{A}(q\bar{q} \to Q\bar{Q}[^3P_2^{(8)}]g)|^2 = \frac{8(4\pi\alpha_s)^3}{81M^3}\frac{(\hat{s}^2+6M^4)(\hat{t}^2+\hat{u}^2)+12M^2\hat{s}\hat{t}\hat{u}}{\hat{s}(\hat{s}-M^2)^4} \tag{A.3e}$$

$gq \to Q\bar{Q}[^{2S+1}L_J^{(8)}]q$ channel:

$$\overline{\sum}|\mathcal{A}(gq \to Q\bar{Q}[^1S_0^{(8)}]q)|^2 = -\frac{5(4\pi\alpha_s)^3}{72M}\frac{\hat{s}^2+\hat{u}^2}{\hat{t}(\hat{t}-M^2)^2} \tag{A.4a}$$

$$\overline{\sum}|\mathcal{A}(gq \to Q\bar{Q}[^3S_1^{(8)}]q)|^2 = -\frac{(4\pi\alpha_s)^3}{108M^3}\frac{\hat{s}^2+\hat{u}^2+2M^2\hat{t}}{\hat{s}\hat{u}(\hat{t}-M^2)^2}[4(\hat{s}^2+\hat{u}^2)-\hat{s}\hat{u}] \tag{A.4b}$$

$$\overline{\sum}|\mathcal{A}(gq \to Q\bar{Q}[^3P_0^{(8)}]q)|^2 = -\frac{5(4\pi\alpha_s)^3}{54M^3}\frac{(\hat{t}-3M^2)^2(\hat{s}^2+\hat{u}^2)}{\hat{t}(\hat{t}-M^2)^4} \tag{A.4c}$$

$$\overline{\sum}|\mathcal{A}(gq \to Q\bar{Q}[^3P_1^{(8)}]q)|^2 = -\frac{5(4\pi\alpha_s)^3}{27M^3}\frac{\hat{t}(\hat{s}^2+\hat{u}^2)+4M^2\hat{s}\hat{u}}{(\hat{t}-M^2)^4} \tag{A.4d}$$

$$\overline{\sum}|\mathcal{A}(gq \to Q\bar{Q}[^3P_2^{(8)}]q)|^2 = -\frac{(4\pi\alpha_s)^3}{27M^3}\frac{(\hat{t}^2+6M^4)(\hat{s}^2+\hat{u}^2)+12M^2\hat{s}\hat{t}\hat{u}}{\hat{t}(\hat{t}-M^2)^4} \tag{A.4e}$$

$gg \to Q\bar{Q}[^{2S+1}L_J^{(8)}]g$ channel:[1]

$$\overline{\sum}|\mathcal{A}(gg \to Q\bar{Q}[^1S_0^{(8)}]g)|^2 = \frac{5(4\pi\alpha_s)^3}{16M}[\hat{s}^2(\hat{s}-M^2)^2 + \hat{s}\hat{t}\hat{u}(M^2-2\hat{s}) + (\hat{t}\hat{u})^2]$$
$$\times \frac{[(\hat{s}^2 - M^2\hat{s} + M^4)^2 - \hat{t}\hat{u}(2\hat{t}^2 + 3\hat{t}\hat{u} + 2\hat{u}^2)]}{\hat{s}\hat{t}\hat{u}(\hat{s}-M^2)^2(\hat{t}-M^2)^2(\hat{u}-M^2)^2} \tag{A.5a}$$

$$\overline{\sum}|\mathcal{A}(gg \to Q\bar{Q}[^3S_1^{(8)}]g)|^2 = -\frac{(4\pi\alpha_s)^3}{72M^3}\frac{27(\hat{s}\hat{t}+\hat{t}\hat{u}+\hat{u}\hat{s}) - 19M^4}{[(\hat{s}-M^2)(\hat{t}-M^2)(\hat{u}-M^2)]^2}$$
$$\times[(\hat{t}^2+\hat{t}\hat{u}+\hat{u}^2)^2 - M^2(\hat{t}+\hat{u})(2\hat{t}^2+\hat{t}\hat{u}+2\hat{u}^2) + M^4(\hat{t}^2+\hat{t}\hat{u}+\hat{u}^2)] \tag{A.5b}$$

$$\overline{\sum}|\mathcal{A}(gg \to Q\bar{Q}[^3P_0^{(8)}]g)|^2 = \frac{(4\pi\alpha_s)^3}{12M^3}$$
$$\times\Big\{\hat{s}^2\hat{z}^4(\hat{s}^2-\hat{z}^2)^4 + M^2\hat{s}\hat{z}^2(\hat{s}^2-\hat{z}^2)^2(3\hat{s}^2-2\hat{z}^2)(2\hat{s}^4-6\hat{s}^2\hat{z}^2+3\hat{z}^4)$$
$$+M^4[9\hat{s}^{12} - 84\hat{s}^{10}\hat{z}^2 + 265\hat{s}^8\hat{z}^4 - 382\hat{s}^6\hat{z}^6 + 276\hat{s}^4\hat{z}^8 - 88\hat{s}^2\hat{z}^{10} + 9\hat{z}^{12}]$$
$$-M^6\hat{s}[54\hat{s}^{10} - 357\hat{s}^8\hat{z}^2 + 844\hat{s}^6\hat{z}^4 - 898\hat{s}^4\hat{z}^6 + 439\hat{s}^2\hat{z}^8 - 81\hat{z}^{10}]$$
$$+M^8[153\hat{s}^{10} - 798\hat{s}^8\hat{z}^2 + 1415\hat{s}^6\hat{z}^4 - 1041\hat{s}^4\hat{z}^6 + 301\hat{s}^2\hat{z}^8 - 18\hat{z}^{10}]$$
$$-M^{10}\hat{s}[270\hat{s}^8 - 1089\hat{s}^6\hat{z}^2 + 1365\hat{s}^4\hat{z}^4 - 616\hat{s}^2\hat{z}^6 + 87\hat{z}^8]$$
$$+M^{12}[324\hat{s}^8 - 951\hat{s}^6\hat{z}^2 + 769\hat{s}^4\hat{z}^4 - 189\hat{s}^2\hat{z}^6 + 9\hat{z}^8]$$
$$-9M^{14}\hat{s}(6\hat{s}^2-\hat{z}^2)(5\hat{s}^4 - 9\hat{s}^2\hat{z}^2 + 3\hat{z}^4)$$
$$+3M^{16}\hat{s}^2(51\hat{s}^4 - 59\hat{s}^2\hat{z}^2 + 12\hat{z}^4) - 27M^{18}\hat{s}^3(2\hat{s}^2-\hat{z}^2) + 9M^{20}\hat{s}^4\Big\}$$
$$/[\hat{s}\hat{z}^2(\hat{s}-M^2)^4(\hat{s}M^2+\hat{z}^2)^4] \tag{A.5c}$$

(A.5d)

[1] We have introduced the variable $\hat{z} = \sqrt{\hat{t}\hat{u}}$ to simplify some of the coefficients.

$$\overline{\sum}|\mathcal{A}(gg \to Q\bar{Q}[^3P_2^{(8)}]g)|^2 = \frac{(4\pi\alpha_s)^3}{6M^3}$$
$$\times\Big\{\hat{s}^2\hat{z}^4(\hat{s}^2-\hat{z}^2)^4 + M^2\hat{s}\hat{z}^2(\hat{s}^2-\hat{z}^2)^2(6\hat{s}^6-22\hat{s}^4\hat{z}^2-9\hat{s}^2\hat{z}^4-6\hat{z}^6)$$
$$+M^4[6\hat{s}^{12}-66\hat{s}^{10}\hat{z}^2+175\hat{s}^8\hat{z}^4-127\hat{s}^6\hat{z}^6+42\hat{s}^4\hat{z}^8-25\hat{s}^2\hat{z}^{10}+6\hat{z}^{12}]$$
$$-M^6\hat{s}[36\hat{s}^{10}-243\hat{s}^8\hat{z}^2+433\hat{s}^6\hat{z}^4-271\hat{s}^4\hat{z}^6+115\hat{s}^2\hat{z}^8-39\hat{z}^{10}]$$
$$+M^8[102\hat{s}^{10}-492\hat{s}^8\hat{z}^2+665\hat{s}^6\hat{z}^4-381\hat{s}^4\hat{z}^6+133\hat{s}^2\hat{z}^8-12\hat{z}^{10}]$$
$$-M^{10}\hat{s}[180\hat{s}^8-651\hat{s}^6\hat{z}^2+696\hat{s}^4\hat{z}^4-310\hat{s}^2\hat{z}^6+63\hat{z}^8]$$
$$+M^{12}[216\hat{s}^8-591\hat{s}^6\hat{z}^2+463\hat{s}^4\hat{z}^4-129\hat{s}^2\hat{z}^6+6\hat{z}^8]$$
$$-3M^{14}\hat{s}[60\hat{s}^6-118\hat{s}^4\hat{z}^2+55\hat{s}^2\hat{z}^4-6\hat{z}^6]$$
$$+3M^{16}\hat{s}^2(34\hat{s}^4-41\hat{s}^2\hat{z}^2+8\hat{z}^4)-18M^{18}\hat{s}^3(2\hat{s}^2-\hat{z}^2)+6M^{20}\hat{s}^4\Big\}$$
$$/[\hat{s}\hat{z}^2(\hat{s}-M^2)^4(\hat{s}M^2+\hat{z}^2)^4] \qquad \text{(A.5e)}$$

Appendix B Color-singlet functions in e^+e^- cross section

We list here the color-singlet functions S and α which enter into the differential cross section (3.7) at leading order in both the perturbative QCD and NRQCD velocity expansions [45]. Recall the definitions $\delta = 2M_Q/E$ and $z_i = E_i/E$.

$\underline{e^+e^- \to Q\bar{Q}[^3S_1^{(1)}] + g + g \text{ mode:}}$

$$
\begin{aligned}
S_{\text{gluon}} = {} & \frac{\pi}{216}\frac{(\alpha_s\,\alpha_{EM}\,\mathcal{Q}_Q)^2}{\delta\,E^5}\frac{\left\langle 0|\mathcal{O}_1^{\psi_Q}(\,^3S_1)|0\right\rangle}{(z_3-2)^2\,(2z_3-\delta^2)^3\,(z_3^2-\delta^2)} \\
& \times \Big\{ 4\Big[-\delta^2(4+\delta^2)(48+48\delta^2+13\delta^4) + 32\delta^2(4+\delta^2)(4+3\delta^2)z_3 \\
& \quad + 8(32-56\delta^2-24\delta^4+\delta^6)z_3^2 - 16(32+4\delta^2+3\delta^4)z_3^3 \\
& \quad + 112(4+\delta^2)z_3^4 - 128z_3^5\Big]\,(2z_3-\delta^2)\sqrt{z_3^2-\delta^2} \qquad \text{(B.1a)} \\
& + \Big[\delta^4(4-\delta^2)(48+96\delta^2+13\delta^4) - 32\delta^4(28-3\delta^2-3\delta^4)z_3 \\
& \quad + 8\delta^2(16-40\delta^2-27\delta^4+\delta^6)z_3^2 + 16\delta^2(56+14\delta^2-3\delta^4)z_3^3 \\
& \quad - 16(4-\delta^2)(4+5\delta^2)z_3^4\Big]\,(4z_3-4-\delta^2)\ln\frac{2z_3-\delta^2+2\sqrt{z_3^2-\delta^2}}{2z_3-\delta^2-2\sqrt{z_3^2-\delta^2}}\Big\}
\end{aligned}
$$

$$
\begin{aligned}
\alpha_{\text{gluon}}(z_3) = {} & \frac{\pi}{216}\frac{(\alpha_s\,\alpha_{EM}\,\mathcal{Q}_Q)^2}{\delta\,E^5}\frac{\left\langle 0|\mathcal{O}_1^{\psi_Q}(\,^3S_1)|0\right\rangle}{(z_3-2)^2\,(2z_3-\delta^2)^3\,(z_3^2-\delta^2)}\frac{1}{S_{\text{gluon}}(z_3)} \\
& \times \Big\{ 4\Big[\delta^2(64+80\delta^2+76\delta^4+7\delta^6) - 96\delta^4(4+\delta^2)z_3 \\
& \quad - 8(32-40\delta^2-44\delta^4-\delta^6)z_3^2 - 16\delta^2(28+3\delta^2)z_3^3 \\
& \quad + 16(20+7\delta^2)z_3^4 - 128z_3^5\Big]\,(2z_3-\delta^2)\sqrt{z_3^2-\delta^2} \qquad \text{(B.1b)} \\
& - \Big[\delta^4(4-\delta^2)(4+\delta^2)(4+7\delta^2) - 32\delta^4(1-\delta^2)(4+3\delta^2)z_3 \\
& \quad - 8\delta^2(16+40\delta^2+57\delta^4+\delta^6)z_3^2 + 16\delta^2(8+58\delta^2+3\delta^4)z_3^3 \\
& \quad + 16(16-32\delta^2-5\delta^4)z_3^4\Big]\,(4z_3-4-\delta^2)\ln\frac{2z_3-\delta^2+2\sqrt{z_3^2-\delta^2}}{2z_3-\delta^2-2\sqrt{z_3^2-\delta^2}}\Big\}
\end{aligned}
$$

$e^+e^- \to Q\bar{Q}[^3S_1^{(1)}] + Q + \bar{Q}$ mode:

$$
\begin{aligned}
S_{\rm quark}(z_3) = \frac{\pi}{3888}\frac{(\alpha_s\,\alpha_{EM}\,\mathcal{Q}_Q)^2}{\delta^3\,E^5}\frac{\left\langle 0|\mathcal{O}_1^{\psi_Q}(\,^3S_1)|0\right\rangle}{z_3^3\,(z_3-2)^6\,(z_3^2-\delta^2)} \\
\times\Bigg\{4z_3\sqrt{\frac{(1-z_3)(z_3^2-\delta^2)}{4+\delta^2-4z_3}}\Big[-32\delta^4(4+\delta^2)(48+22\delta^2+3\delta^4) \\
+32\delta^4(768+400\delta^2+66\delta^4+3\delta^6)z_3 \\
-16\delta^2(384+1920\delta^2+556\delta^4+29\delta^6-2\delta^8)z_3^2 \\
+8\delta^2(1792+128\delta^2-568\delta^4-80\delta^6-\delta^8)z_3^3 \\
+2(2048-11008\delta^2+10752\delta^4+3176\delta^6+98\delta^8+3\delta^{10})z_3^4 \\
-4(4096-7808\delta^2+3424\delta^4+600\delta^6+17\delta^8)z_3^5 \\
+(38912-20608\delta^2+4544\delta^4+508\delta^6-3\delta^8)z_3^6 \\
-4(13312-800\delta^2+120\delta^4-3\delta^6)z_3^7+8(4512-20\delta^2-15\delta^4)z_3^8 \\
-\;32(336-\delta^2)z_3^9+1280z_3^{10}\Big] \qquad \text{(B.2a)} \\
-\Big[8\delta^4(48+22\delta^2+3\delta^4)-32\delta^4(24+5\delta^2)z_3 \\
-2\delta^2(448+16\delta^2+8\delta^4-3\delta^6)z_3^2+16\delta^2(56-10\delta^2-5\delta^4)z_3^3 \\
+\delta^2(1152+272\delta^2-3\delta^4)z_3^4+8(32-92\delta^2+5\delta^4)z_3^5 \\
-56(16+\delta^2)z_3^6+512z_3^7\Big] \\
\times\delta^2(z_3^2-2)^4\ln\frac{z_3\sqrt{4+\delta^2-4z_3}+2\sqrt{(1-z_3)(z_3^2-\delta^2)}}{z_3\sqrt{4+\delta^2-4z_3}-2\sqrt{(1-z_3)(z_3^2-\delta^2)}}\Bigg\}
\end{aligned}
$$

$$\alpha_{\rm quark}(z_3) = \frac{\pi}{3888}\frac{(\alpha_s\,\alpha_{EM}\,\mathcal{Q}_Q)^2}{\delta^3\,E^5}\frac{\left\langle 0|\mathcal{O}_1^{\psi_Q}(\,^3S_1)|0\right\rangle}{z_3^3\,(z_3-2)^6\,(z_3^2-\delta^2)}\frac{1}{S_{\rm quark}(z_3)}$$

$$\times\Bigg\{4z_3\sqrt{\frac{(1-z_3)(z_3^2-\delta^2)}{4+\delta^2-4z_3}}\Big[32\delta^4(4+\delta^2)(16+2\delta^2+3\delta^4)$$

$$-32\delta^4(256+48\delta^2+22\delta^4+3\delta^6)z_3$$

$$+16\delta^2(1152+1024\delta^2-140\delta^4-53\delta^6-2\delta^8)z_3^2$$

$$-8\delta^2(5376+128\delta^2-1576\delta^4-240\delta^6-\delta^8)z_3^3$$

$$+2(2048-768\delta^2-19968\delta^4-6968\delta^6-350\delta^8-3\delta^{10})z_3^4$$

$$-4(4096-20096\delta^2-11168\delta^4-1208\delta^6-43\delta^8)z_3^5$$

$$+(38912-75392\delta^2-16960\delta^4-996\delta^6-3\delta^8)z_3^6$$

$$-4(13312-6304\delta^2-872\delta^4-3\delta^6)z_3^7+8(4512-500\delta^2-15\delta^4)z_3^8$$

$$-\;32(336-\delta^2)z_3^9+1280z_3^{10}\Big] \qquad \text{(B.2b)}$$

$$+\;\Big[8\delta^4(16+2\delta^2+3\delta^4)-32\delta^4(8-\delta^2)z_3$$

$$-2\delta^2(320-272\delta^2+64\delta^4-3\delta^6)z_3^2+16\delta^2(40-54\delta^2-5\delta^4)z_3^3$$

$$-(1024-720\delta^4-3\delta^6)z_3^4+8(96-36\delta^2-5\delta^4)z_3^5$$

$$+8(80+7\delta^2)z_3^6-512z_3^7\Big]$$

$$\times\delta^2(z_3^2-2)^4\ln\frac{z_3\sqrt{4+\delta^2-4z_3}+2\sqrt{(1-z_3)(z_3^2-\delta^2)}}{z_3\sqrt{4+\delta^2-4z_3}-2\sqrt{(1-z_3)(z_3^2-\delta^2)}}\Bigg\}$$

Appendix C Inclusive angular distributions in electron-positron collisions

It is useful to note some general features of inclusive, unpolarized ψ_Q production in e^+e^- annihilation [45]. Unitarity, parity and angular momentum considerations restrict the form of the differential cross section expression

$$\frac{d^2\sigma}{dE_3 d\cos\theta_3}\left(e^+(p_1)e^-(p_2) \to \gamma^* \to \psi_Q(p_3) + X\right) = S(E_3)\left[1 + \alpha(E_3)\cos^2\theta_3\right]. \quad \text{(C.1)}$$

In particular, the allowed range for the angular coefficient function is constrained to lie within the interval $-1 \leq \alpha(E_3) \leq 1$. We sketch a derivation of this result below.

It is instructive to consider the subprocess $\gamma^*(P) \to \psi_Q(p_3) + X(P - p_3)$ where the intermediate photon is either longitudinally or transversely aligned. The squared amplitude for this decay

$$|\mathcal{A}|^2 = \sum_\lambda \varepsilon_\mu(P;\lambda)\varepsilon_\nu(P;\lambda)^* F^{\mu\nu} \quad \text{(C.2)}$$

involves a form factor $F^{\mu\nu}$ which can be decomposed in terms of tensors that respect parity and gauge invariance:

$$F^{\mu\nu} = -F_1\left(g^{\mu\nu} - \frac{P^\mu P^\nu}{P^2}\right) + \frac{F_2}{P^2}\left(p_3^\mu - \frac{P\cdot p_3}{P^2}P^\mu\right)\left(p_3^\nu - \frac{P\cdot p_3}{P^2}P^\nu\right). \quad \text{(C.3)}$$

Working in the γ^* rest frame where the ψ_Q four-momentum looks like $p_3 = (E_3, \vec{p}_3) = (E_3, |\vec{p}_3|\sin\theta\cos\phi, |\vec{p}_3|\sin\theta\sin\phi, |\vec{p}_3|\cos\theta)$, we find that the squared decay amplitude for a longitudinally polarized virtual photon reduces to

$$|\mathcal{A}|_L^2 = F_1[1 + \alpha_L\cos^2\theta], \quad \text{(C.4)}$$

with

$$\alpha_L = \frac{|\vec{p}_3|^2}{P^2}\frac{F_2}{F_1}. \tag{C.5}$$

For a transverse γ^*, the squared amplitude takes the form

$$|\mathcal{A}|_T^2 = \left(2F_1 + \frac{|\vec{p}_3|^2}{P^2}F_2\right)[1 + \alpha_T \cos^2\theta], \tag{C.6}$$

where

$$\alpha_T = -\frac{|\vec{p}_3|^2 F_2}{2P^2F_1 + |\vec{p}_3|^2F_2} = -\frac{\alpha_L}{2+\alpha_L}. \tag{C.7}$$

Since both $|\mathcal{A}|_L^2$ and $|\mathcal{A}|_T^2$ are nonnegative, Eqs. (C.4) and (C.7) imply $\alpha_L \geq -1$ and $-1 \leq \alpha_T \leq 1$.

Helicity conservation requires the intermediate photon in $e^+e^- \to \gamma^* \to \psi_Q + X$ to be transversely aligned relative to the beam axis in the $m_e = 0$ limit. The ψ_Q meson's angular distribution is therefore significantly restricted by simple symmetry considerations. In fact, the inclusive angular distribution of *any* unpolarized particle which is produced in electron-positron colliders operating well below the Z-pole goes as $1 + \alpha_T \cos^2\theta$ with $-1 \leq \alpha_T \leq 1$. So while observation of a pure $\sin^2\theta$ distribution for a lepton or hadron at a collider like CLEO is possible, a pure $\cos^2\theta$ distribution is not.

Appendix D Functions entering polarized quarkonia production cross section

Functions entering into polarized cross sections [65]:

$qq \to \psi^{(\lambda)} g$:

$$
\begin{aligned}
A_{qq}[{}^1S_0^{(8)}] &= \frac{20\alpha_s^3\pi^2}{81M\hat{s}^2}\,\frac{\hat{t}^2+\hat{u}^2}{\hat{s}(\hat{s}-M^2)^2},\\
B_{qq}[{}^1S_0^{(8)}] &= C_{qq}[{}^1S_0^{(8)}] = D_{qq}[{}^1S_0^{(8)}] = 0,
\end{aligned}
\tag{D.1a}
$$

$$
\begin{aligned}
A_{qq}[{}^3S_1^{(8)}] &= \frac{4\alpha_s^3\pi^2}{81M^3\hat{s}^2}\,\frac{\left(4(\hat{t}^2+\hat{u}^2)-\hat{t}\hat{u}\right)(\hat{s}^2-2\hat{t}\hat{u}+M^4)}{\hat{t}\hat{u}(\hat{s}-M^2)^2},\\
B_{qq}[{}^3S_1^{(8)}] &= -\frac{16\alpha_s^3\pi^2}{81M\hat{s}^2}\,\frac{\left(4(\hat{t}^2+\hat{u}^2)-\hat{t}\hat{u}\right)}{\hat{t}\hat{u}(\hat{s}-M^2)^2},\\
C_{qq}[{}^3S_1^{(8)}] &= -\frac{16\alpha_s^3\pi^2}{81M\hat{s}^2}\,\frac{\left(4(\hat{t}^2+\hat{u}^2)-\hat{t}\hat{u}\right)}{\hat{t}\hat{u}(\hat{s}-M^2)^2},\\
D_{qq}[{}^3S_1^{(8)}] &= 0,
\end{aligned}
\tag{D.1b}
$$

$$
\begin{aligned}
A_{qq}[{}^3P_J^{(8)}] &= \frac{80\alpha_s^3\pi^2}{27M^3\hat{s}^2}\,\frac{\hat{s}^2-2\hat{t}\hat{u}+3M^4}{\hat{s}(\hat{s}-M^2)^2},\\
B_{qq}[{}^3P_J^{(8)}] &= -\frac{640\alpha_s^3\pi^2}{27M\hat{s}^2}\,\frac{\hat{t}\hat{u}+\hat{u}M^2-M^4}{\hat{s}^2(\hat{s}-M^2)^3},\\
C_{qq}[{}^3P_J^{(8)}] &= -\frac{640\alpha_s^3\pi^2}{27M\hat{s}^2}\,\frac{\hat{t}\hat{u}+\hat{t}M^2-M^4}{\hat{s}^2(\hat{s}-M^2)^3},\\
D_{qq}[{}^3P_J^{(8)}] &= \frac{640\alpha_s^3\pi^2}{27M\hat{s}^2}\,\frac{\hat{s}^2+\hat{s}M^2-2\hat{t}\hat{u}}{\hat{s}^2(\hat{s}-M^2)^3},
\end{aligned}
\tag{D.1c}
$$

$gq \to \psi^{(\lambda)} q$:

$$
A_{gq}[{}^1S_0^{(8)}] = -\frac{5\alpha_s^3\pi^2}{54M\hat{s}^2}\,\frac{\hat{s}^2+\hat{u}^2}{\hat{t}(\hat{t}-M^12)^2},
$$

$$B_{gq}[^1S_0^{(8)}] = C_{gq}[^1S_0^{(8)}] = D_{gq}[^1S_0^{(8)}] = 0, \tag{D.2a}$$

$$\begin{aligned}
A_{gq}[^3S_1^{(8)}] &= -\frac{\alpha_s^3\pi^2}{54M^3\hat{s}^2}\,\frac{(4(\hat{s}^2+\hat{u}^2)-\hat{s}\hat{u})\,(\hat{t}^2-2\hat{s}\hat{u}+M^4)}{\hat{s}\hat{u}(\hat{t}-M^2)^2}, \\
B_{gq}[^3S_1^{(8)}] &= \frac{2\alpha_s^3\pi^2}{27M\hat{s}^2}\,\frac{(4(\hat{s}^2+\hat{u}^2)-\hat{s}\hat{u})}{\hat{s}\hat{u}(\hat{t}-M^2)^2}, \\
C_{gq}[^3S_1^{(8)}] &= \frac{4\alpha_s^3\pi^2}{27M\hat{s}^2}\,\frac{(4(\hat{s}^2+\hat{u}^2)-\hat{s}\hat{u})}{\hat{s}\hat{u}(\hat{t}-M^2)^2}, \\
D_{gq}[^3S_1^{(8)}] &= \frac{4\alpha_s^3\pi^2}{27M\hat{s}^2}\,\frac{(4(\hat{s}^2+\hat{u}^2)-\hat{s}\hat{u})}{\hat{s}\hat{u}(\hat{t}-M^2)^2},
\end{aligned} \tag{D.2b}$$

$$\begin{aligned}
A_{gq}[^3P_J^{(8)}] &= -\frac{10\alpha_s^3\pi^2}{9M^3\hat{s}^2}\,\frac{\hat{t}^2-2\hat{s}\hat{u}+3M^4}{\hat{t}(\hat{t}-M^2)^2}, \\
B_{gq}[^3P_J^{(8)}] &= \frac{80\alpha_s^3\pi^2}{9M\hat{s}^2}\,\frac{\hat{s}\hat{u}+\hat{u}M^2-M^4}{\hat{t}^2(\hat{t}-M^2)^3}, \\
C_{gq}[^3P_J^{(8)}] &= \frac{80\alpha_s^3\pi^2}{9M\hat{s}^2}\,\frac{\hat{t}+M^2}{\hat{t}^2(\hat{t}-M^2)^2}, \\
D_{gq}[^3P_J^{(8)}] &= \frac{80\alpha_s^3\pi^2}{9M\hat{s}^2}\,\frac{\hat{t}^2-M^2(2\hat{s}+\hat{t})}{\hat{t}^2(\hat{t}-M^2)^3},
\end{aligned} \tag{D.2c}$$

$gg \to \psi^{(\lambda)}g$:[1]

$$\begin{aligned}
A_{gg}[^1S_0^{(1)}] &= \frac{5\alpha_s^3\pi^2}{12M\hat{s}^2}\,\left[\hat{s}^2(\hat{s}-M^2)^2+\hat{s}\hat{t}\hat{u}(M^2-2\hat{s})+(\hat{t}\hat{u})^2\right] \\
&\quad\times\frac{(\hat{s}^2-M^2\hat{s}+M^4)^2-\hat{t}\hat{u}(2\hat{t}^2+3\hat{t}\hat{u}+2\hat{u}^2)}{\hat{s}\hat{t}\hat{u}(\hat{s}-M^2)^2(\hat{t}-M^2)^2(\hat{u}-M^2)^2}, \\
B_{gg}[^1S_0^{(1)}] &= C_{gg}[^1S_0^{(1)}] = D_{gg}[^1S_0^{(1)}] = 0,
\end{aligned} \tag{D.3a}$$

$$\begin{aligned}
A_{gg}[^3S_1^{(1)}] &= \frac{10\alpha_s^3\pi^2M}{81\hat{s}^2}\,\frac{\hat{s}^2(\hat{s}-M^2)^2+\hat{t}\hat{u}\;(\hat{s}\hat{t}+\hat{t}\hat{u}+\hat{u}\hat{s}-\hat{s}^2)}{(\hat{s}-M^2)^2(\hat{t}-M^2)^2(\hat{u}-M^2)^2} \\
B_{gg}[^3S_1^{(1)}] &= -\frac{20\alpha_s^3\pi^2M^3}{81\hat{s}^2}\,\frac{(\hat{s}^2+\hat{t}^2)}{(\hat{s}-M^2)^2(\hat{t}-M^2)^2(\hat{u}-M^2)^2}, \\
C_{gg}[^3S_1^{(1)}] &= -\frac{20\alpha_s^3\pi^2M^3}{81\hat{s}^2}\,\frac{(\hat{s}^2+\hat{u}^2)}{(\hat{s}-M^2)^2(\hat{t}-M^2)^2(\hat{u}-M^2)^2}, \\
D_{gg}[^3S_1^{(1)}] &= -\frac{40\alpha_s^3\pi^2M^3}{81\hat{s}^2}\,\frac{\hat{s}^2}{(\hat{s}-M^2)^2(\hat{t}-M^2)^2(\hat{u}-M^2)^2},
\end{aligned} \tag{D.3b}$$

[1] We have introduced the variable $\hat{z} = \sqrt{\hat{t}\hat{u}}$ to simplify some of the coefficients.

$$
\begin{aligned}
A_{gg}[{}^3S_1^{(8)}] &= \frac{\alpha_s^3\pi^2}{36M^3\hat{s}^2}\,\frac{\left[27(\hat{s}^2-\hat{t}\hat{u}-M^2\hat{s})+19M^4\right]}{(\hat{s}-M^2)^2(\hat{t}-M^2)^2(\hat{u}-M^2)^2} \\
&\quad\times\left[\hat{s}^2(\hat{s}-M^2)^2+\hat{t}\hat{u}\;(\hat{s}\hat{t}+\hat{t}\hat{u}+\hat{u}\hat{s}-\hat{s}^2)\right], \\
B_{gg}[{}^3S_1^{(8)}] &= -\frac{\alpha_s^3\pi^2}{18M\hat{s}^2}\,\frac{\left[27(\hat{s}^2-\hat{t}\hat{u}-M^2\hat{s})+19M^4\right](\hat{s}^2+\hat{t}^2)}{(\hat{s}-M^2)^2(\hat{t}-M^2)^2(\hat{u}-M^2)^2}, \\
C_{gg}[{}^3S_1^{(8)}] &= -\frac{\alpha_s^3\pi^2}{18M\hat{s}^2}\,\frac{\left[27(\hat{s}^2-\hat{t}\hat{u}-M^2\hat{s})+19M^4\right](\hat{s}^2+\hat{u}^2)}{(\hat{s}-M^2)^2(\hat{t}-M^2)^2(\hat{u}-M^2)^2}, \\
D_{gg}[{}^3S_1^{(8)}] &= -\frac{\alpha_s^3\pi^2}{9M\hat{s}^2}\,\frac{\left[27(\hat{s}^2-\hat{t}\hat{u}-M^2\hat{s})+19M^4\right]\hat{s}^2}{(\hat{s}-M^2)^2(\hat{t}-M^2)^2(\hat{u}-M^2)^2},
\end{aligned}
\tag{D.3c}
$$

$$A_{gg}[^3P_J^{(8)}] = \frac{5\alpha_s^3\pi^2}{M^3\hat{s}^2}\Big\{ M^2\hat{s}^3(\hat{s}-M^2)^3(\hat{s}^4-2M^2\hat{s}^3+7M^4\hat{s}^2-6M^6\hat{s}+3M^8)$$
$$+\hat{s}^2\hat{z}^2(\hat{s}-M^2)(\hat{s}^6-8M^2\hat{s}^5+23M^4\hat{s}^4-50M^6\hat{s}^3+56M^8\hat{s}^2$$
$$-31M^{10}\hat{s}+6M^{12})$$
$$-\hat{s}\hat{z}^4(4\hat{s}^6-9M^2\hat{s}^5+31M^4\hat{s}^4-71M^6\hat{s}^3+77M^8\hat{s}^2-34M^{10}\hat{s}$$
$$+6M^{12})$$
$$+\hat{z}^6(6\hat{s}^5+4M^2\hat{s}^4+20M^4\hat{s}^3-33M^6\hat{s}^2+22M^8\hat{s}-3M^{10})$$
$$-2\hat{z}^8(2\hat{s}^3+2M^2\hat{s}^2+5M^4\hat{s}-3M^6)$$
$$+\hat{z}^{10}(\hat{s}-M^2)\Big\}\Big/\left(\hat{s}\hat{z}^2(\hat{s}-M^2)^3(M^2s+\hat{z}^2)^3\right),$$

$$B_{gg}[^3P_J^{(8)}] = -\frac{5\alpha_s^3\pi^2}{M\hat{s}^2}\Big\{4\hat{u}^5(M^2-\hat{u})^7$$
$$-\hat{t}\hat{u}^3(M^2-\hat{u})^4(M^8-7M^6\hat{u}+42M^4\hat{u}^2-52M^2\hat{u}^3+24\hat{u}^4)$$
$$+\hat{t}^2\hat{u}^2(M^2-\hat{u})^3(2M^{10}-M^8\hat{u}-39M^6\hat{u}^2+152M^4\hat{u}^3$$
$$-166M^2\hat{u}^4+68\hat{u}^5)$$
$$-\hat{t}^3\hat{u}(M^2-\hat{u})^2(M^{12}+9M^{10}\hat{u}+2M^8\hat{u}^2-134M^6\hat{u}^3+361M^4\hat{u}^4$$
$$-339M^2\hat{u}^5+116\hat{u}^6)$$
$$+\hat{t}^4\hat{u}(M^2-\hat{u})(11M^{12}+9M^{10}\hat{u}+16M^8\hat{u}^2-274M^6\hat{u}^3$$
$$+589M^4\hat{u}^4-471M^2\hat{u}^5+128\hat{u}^6)$$
$$+\hat{t}^5(M^2-\hat{u})(4M^{12}-51M^{10}\hat{u}+2M^8\hat{u}^2-36M^6\hat{u}^3+282M^4\hat{u}^4$$
$$-329M^2\hat{u}^5+80\hat{u}^6)$$
$$-\hat{t}^6(20M^{12}-129M^{10}\hat{u}+94M^8\hat{u}^2-12M^6\hat{u}^3+150M^4\hat{u}^4$$
$$-147M^2\hat{u}^5+8\hat{u}^6)$$
$$+8\hat{t}^7(5M^{10}-19M^8\hat{u}+6M^6\hat{u}^2+6M^4\hat{u}^3-3M^2\hat{u}^4+5\hat{u}^5)$$
$$-8\hat{t}^8(5M^8-11M^6\hat{u}-2M^4\hat{u}^2+7M^2\hat{u}^3-5\hat{u}^4)$$
$$+20\hat{t}^9(M^2-\hat{u})^2(M^2+\hat{u})$$
$$-4\hat{t}^{10}(M^4-\hat{u}^2)\Big\}\Big/\left(\hat{s}^2\hat{t}^2\hat{u}^2(\hat{s}-M^2)^3(\hat{t}-M^2)^3(\hat{u}-M^2)^3\right),$$

$$C_{gg}[^3P_J^{(8)}] = B_{gg}[^3P_J^{(8)}]|_{\hat{t}\leftrightarrow\hat{u}}, \tag{D.3d}$$

$$D_{gg}[{}^3P_J^{(8)}] = \frac{10\alpha_s^3\pi^2}{M\hat{s}^2}\Big\{4M^2\hat{s}^6(\hat{s}-M^2)^5$$
$$-M^2\hat{s}^4\hat{z}^2(\hat{s}-M^2)^2(22\hat{s}^3-38M^2\hat{s}^2+19M^4\hat{s}-4M^6)$$
$$-2\hat{s}^3\hat{z}^4(\hat{s}^5-22M^2\hat{s}^4+62M^4\hat{s}^3-62M^6\hat{s}^2+27M^8\hat{s}-4M^{10})$$
$$+\hat{s}^2\hat{z}^6(2\hat{s}^4-17M^2\hat{s}^3+66M^4\hat{s}^2-31M^6\hat{s}+8M^8)$$
$$+2\hat{s}\hat{z}^8(3\hat{s}^3-6M^2\hat{s}^2-3M^4\hat{s}+2M^6)$$
$$-2\hat{s}\hat{z}^{10}(5\hat{s}-3M^2)+4\hat{z}^{12}\Big\}\Big/\Big(\hat{s}^2\hat{z}^4(\hat{s}-M^2)^3(M^2\hat{s}+\hat{z}^2)^3\Big)\,.$$

Bibliography

[1] J. J. Aubert *et al.*, Phys. Rev. Lett. **33**, 1404 (1974).

[2] J. E. Augusitin *et al.*, Phys. Rev. Lett. **33**, 1406 (1974).

[3] S. W. Herb *et al.*, Phys. Rev. Lett. **39**, 252 (1977).

[4] G. T. Bodwin *et al.*, Phys. Rev. D **51**, 1125 (1995), Erratum-ibid. D **55**, 5853 (1997).

[5] N. Isgur and M. B. Wise, Phys. Lett. B **232**, 113 (1989).

[6] N. Isgur and M. B. Wise, Phys. Lett. B **237**, 527 (1990).

[7] M. Luke and A. V. Manohar, Phys. Rev. **D55**, 4129 (1997).

[8] W. Buchmüller, *Quarkonia* (North-Holland, Amsterdam, 1992).

[9] G. P. Lepage *et al.*, Phys. Rev. D **46**, 4052 (1992).

[10] T. Appelquist and H. D. Politzer, Phys. Rev. Lett. **34**, 43 (1975).

[11] T. Appelquist and H. D. Politzer, Phys. Rev. D **12**, 1404 (1975).

[12] C. Chang, Nucl. Phys. B **172**, 425 (1980).

[13] E. Berger and D. Jones, Phys. Rev. D **23**, 1521 (1981).

[14] J. H. Kühn *et al.*, Nucl. Phys. B **174**, 125 (1979).

[15] B. Guberina *et al.*, Nucl. Phys. B **174**, 317 (1980).

[16] R. Baier and R. Rückl, Z. Phys. C **19**, 251 (1983).

[17] E. Braaten and T. C. Yuan, Phys. Rev. D **50**, 3176 (1994).

[18] L. L. Foldy and S. A. Wouthuysen, Phys. Rev. **78**, 29 (1950).

[19] S. Tani, Prog. Theor. Phys. **6**, 267 (1951).

[20] W. E. Caswell and G. P. Lepage, Phys Lett B **167**, 437 (1986).

[21] G. P. Lepage *et al.*, Phys. Rev. D **46**, 4052 (1992).

[22] A. V. Manohar, Phys. Rev. **D56**, 230 (1997).

[23] B. Grinstein and I. Z. Rothstein, preprint hep/ph9703298 (unpublished).

[24] M. Luke and M. Savage, preprint hep-ph/9707313 (unpublished).

[25] J.-W. Qiu and G. Sterman, Nucl. Phys. B **353**, 137 (1991).

[26] J.-W. Qiu and G. Sterman, Nucl. Phys. B **353**, 105 (1991).

[27] R. Doria *et al.*, Nucl. Phys. B **168**, 93 (1980).

[28] P. Cho and A. Leibovich, Phys. Rev. D **53**, 6203 (1996).

[29] E. Braaten and Y.-Q. Chen, Phys. Rev. D **54**, 3216 (1996).

[30] S. Fleming and I. Maksymyk, Phys. Rev. D **54**, 3608 (1996).

[31] P. Cho and A. Leibovich, Phys. Rev. D **53**, 150 (1996).

[32] W.-K. Tang and M. Vänttinen, Phys. Rev. D **53**, 4851 (1996).

[33] M. Beneke and I. Z. Rothstein, Phys. Rev. D **54**, 2005 (1996), Erratum-ibid. D **54**, 7082 (1996).

[34] E. Braaten *et al.*, Phys. Rev. D **48**, 4230 (1993).

[35] E. Braaten and T. C. Yuan, Phys. Rev. Lett. **71**, 1673 (1993).

[36] G. Altarelli and G. Parisi, Nucl. Phys. B **126**, 298 (1977).

[37] The CDF collaboration, preprint Fermilab-Conf-94/136-E (unpublished).

[38] V. Papadimitriou, preprint Fermilab-conf-95/128-E (unpublished).

[39] F. Abe *et al.*, preprint Fermilab-Pub-95/271-E (unpublished).

[40] E. Braaten and Y.-Q. Chen, Phys. Rev. Lett. **76**, 730 (1996).

[41] J. Kühn and H. Schneider, Phys. Rev. D **24**, 2996 (1981).

[42] J. Kühn and H. Schneider, Z. Phys. C **11**, 253 (1981).

[43] V. Driesen *et al.*, Phys. Rev. D **49**, 3197 (1994).

[44] L. Clavelli, Phys. Rev. D **26**, 1610 (1982).

[45] P. Cho and A. Leibovich, Phys. Rev. D **54**, 6690 (1996).

[46] M. S. Alam *et al.*, Phys. Rev. D **50**, 43 (1994).

[47] R. Balest *et al.*, Phys. Rev. D **52**, 2661 (1995).

[48] R. Gastmans *et al.*, Phys. Lett. B **184**, 257 (1987).

[49] B. Humpert, Phys. Lett. B **184**, 105 (1987).

[50] G. A. Schuler, preprint hep-ph/9403387 (unpublished).

[51] R. Mertig *et al.*, Comp. Phys. Comm. **64**, 345 (1991).

[52] E. Braaten *et al.*, Phys. Lett. B **333**, 548 (1994).

[53] P. Cho, Phys. Lett. B **368**, 171 (1996).

[54] E. Braaten and S. Fleming, Phys. Rev. Lett. **74**, 3327 (1995).

[55] E. J. Eichten and C. Quigg, Phys. Rev. D **52**, 1726 (1995).

[56] D. P. Roy and K. Sridhar, Phys. Lett. B **339**, 141 (1994).

[57] M. Cacciari and M. Greco, Phys. Rev. Lett. **73**, 1586 (1994).

[58] M. Beneke and M. Krämer, Phys. Rev. D **55**, 5269 (1997).

[59] S. Fleming *et al.*, Phys. Rev. D **55**, 4098 (1997).

[60] J. Amundson *et al.*, preprint hep-ph/9601298 (unpublished).

[61] M. Beneke *et al.*, preprint hep-ph/9705286 (unpublished).

[62] P. Cho and M. Wise, Phys. Lett. B **346**, 129 (1995).

[63] M. Beneke and I. Z. Rothstein, Phys. Lett. B **372**, 157 (1996), Erratum-ibid. B **389**, 769 (1996).

[64] K. Cheung *et al.*, Phys. Rev. Lett. **76**, 877 (1996).

[65] A. K. Leibovich, preprint hep-ph/9610381 (unpublished).